ABSTRACT

FDTD-BASED FULL WAVE CO-SIMULATION MODEL FOR HYBRID ELECTROMAGNETIC SYSTEMS

by
Tong Li

In high-frequency ranges, the present electronic design automation software has limited capabilities to model electromagnetic (EM) systems where there are strong field effects influencing their characteristics. In this situation, a full-wave simulation tool is desired for the analysis and design of high-speed and non-linear EM systems. It is necessary to explore the interaction between the field and electronic components during a transient process when field effects are more significant. The finite-difference time-domain (FDTD) technique receives growing attention in the area of EM system analysis and simulation due to its simplicity, flexibility and robustness. It is a full-wave simulation method that solves the Maxwell's equations in time domain directly. Decades of research and development and rapid growth in computer capability have built up a firm foundation for FDTD techniques to be applied to many practical problems.

Based on FDTD, this dissertation develops a stable co-simulation method to perform a full-wave simulation of a hybrid EM system consisting of lumped elements and distributed structures. In this method, FDTD is used to solve the EM field problems associated with distributed structures, and a circuit simulator solves the response of lumped elements. A field-circuit model proposed in the dissertation serves as the interface between the two simulation tools. Compared with previous methods, the FDTD method based on this model is much more flexible and stable for linear and nonlinear lumped elements under both small and large signal conditions. Because of its flexibility

and robustness, this model is a promising approach to integrate a field solver and a circuit simulator in the simulations of practical EM systems.

In order to improve the simulation accuracy, some problems related to FDTD simulation are studied. Based on the numerical dispersion in homogeneous media and uniform grids, the FDTD numerical reflection and transmission on the boundary of two media, which are discritized by a non-uniform grid, are investigated. This investigation provides for the first time an estimation of FDTD numerical error in inhomogeneous media and non-uniform grids. Perfectly matched layer (PML) was previously utilized to the homogeneous media or uniform grids. This dissertation extends the PML boundary conditions to handle the inhomogeneous media and non-uniform grid. Techniques for extracting S parameters from FDTD simulation are also discussed.

Two and three-dimensional co-simulation software, written in C++, has been derived, developed and verified in this dissertation. The simulation results agree well with results from other simulation methods, like SPICE, for many test circuits. Taking data sampling and interpolation into account, simulation results generally fit well to the measurement and other simulation results for complicated three-dimensional structures.

With further improvements of the FDTD technique and circuit simulation, the field-circuit co-simulation model will widen its application to general EM systems.

FDTD-BASED FULL WAVE CO-SIMULATION MODEL FOR HYBRID ELECTROMAGNETIC SYSTEMS

by
Tong Li

A Dissertation
Submitted to the Faculty of
New Jersey Institute of Technology
In Partial Fulfillment of the Requirements for the Degree of
Doctor of Philosophy

Department of Electrical and Computer Engineering

May 1999

APPROVAL PAGE

FDTD-BASED FULL WAVE CO-SIMULATION MODEL FOR HYBRID ELECTROMAGNETIC SYSTEMS

Tong Li

Dr. MengChu Zhou, Dissertation Advisor — Date
Associate Professor of Electrical and Computer Engineering, NJIT
Newark, NJ.

Dr. Wenquan Sui, Dissertation Co-Advisor — Date
Senior Scientist, IBM
Hopewell, NY.

Dr. Edip Niver, Committee Member — Date
Associate Professor of Electrical and Computer Engineering, NJIT
Newark, NJ.

Dr. Edwin Hou, Committee Member — Date
Associate Professor of Electrical and Computer Engineering, NJIT
Newark, NJ.

Dr. Jonathan Luke, Committee Member — Date
Associate Professor of Mathematical Sciences, NJIT
Newark, NJ.

BIOGRAPHICAL SKETCH

Author: Tong Li

Degree: Doctor of Philosophy in Electrical Engineering

Date: May, 1999

Undergraduate and Graduate Education

- Doctor of Philosophy in Electrical Engineering,
  New Jersey Institute of Technology, NJ, 1999
- Master of Science in Electrical Engineering,
  Xi'an Jiaotong University, P. R. China, 1992
- Bachelor of Science in Electrical Engineering,
  Xi'an Jiaotong University, P. R. China, 1989

Major: Electrical Engineering

Publications:

Li, T., Sui, W. and Zhou, M.,
"Full wave analysis of a narrow pulse generator," accepted for *SPIE millimeter-wave materials, devices and components conference*, March, 1999.

Li, T., Sui, W. and Zhou, M.,
"Extension of PML boundary conditions in inhomogeneous media in a non-uniform FDTD grid," accepted by *IEEE Transaction on MTT.*

Li, T., Sui, W. and Zhou, M.,
"A Novel field-circuit model for hybrid system co-simulation," submitted to *IEEE Transaction on MTT.*

Li, T., Sui, W., Zhou, M., H. Tsai,
"S parameters extraction for a MMIC matching circuit using hybrid FDTD techniques," submitted to *European Wireless's 99 & ITG Mobile Communications,* March, 1999.

Dedicated to my wife Yinchun for all the challenges we overcame together
and
my parents who are always in my heart

ACKNOWLEDGMENT

At the end of the three-year study for my Ph.D. degree in Electrical and Computer Engineering Department at the New Jersey Institute of Technology, I would like to express my appreciation and thankfulness to my academic advisor, Dr. Mengchu Zhou, who has always encouraged me at each frustrated time and supported me at his best. I would to give my deep gratefulness to my academic co-advisor, Dr. Wenquan Sui, for all of his guidance and instruction to me and many profitable discussions in either phone or meeting. Without the support and guide from Dr. Mengchu Zhou and Dr. Wenquan Sui, this research work would never be finished. Also I would like to thank Dr. Edip Niver for his advisement and material about the practical EM systems. Special thanks are given to Dr. Jonathan Luke for his wonderful explanation to FDTD from a mathematician point of view.

I would like to thank Dr. Mengch Zhou, Dr. Wenquan Sui, Dr. Edip Niver, Dr. Jonathan Luke and Dr. Edwin Hou to serve as members of my doctoral committee.

Thanks Dr. Ali Arkansu for his support of computing resources.

Actually, I owe my success to all my friends and teachers who support me by all means or inspire me in every discussion. Thanks all of them heartfelt.

TABLE OF CONTENTS

Chapter	Page
1. INTRODUCTION	1
1.1. Motivation	1
1.2. Literature Review of FDTD Related Topics	3
1.2.1. FDTD and Its Application	3
1.2.2. Lumped Current Algorithm	6
1.2.3. Absorbing Boundary Conditions (ABCs)	8
1.2.4. Numerical Error And Dispersion	9
1.3. Objective of This Dissertation	10
1.3.1. Limitations of Previous Work	10
1.3.2. Field-Circuit Model For Hybrid System Co-Simulation	11
1.4. Conclusion	14
2. OVERVIEW OF FDTD AND RELATED TOPICS	15
2.1. Introduction	15
2.2. Fundamental FDTD Method	15
2.2.1. Yee Algorithm	15
2.2.2. Numerical Dispersion	19
2.2.3. Stability Criterion	20
2.3. Lumped Current Algorithm	21
2.4. Absorbing Boundary Conditions (ABCs)	27
2.4.1. Mur's ABCs	27
2.4.2. Perfectly Matched Layer (PML)	29

TABLE OF CONTENTS
(continued)

Chapter	Page
2.5. Conclusion	33
3. NUMERICAL ERROR OF FDTD METHOD	35
3.1. Introduction	35
3.2. Non-Uniform FDTD Grid	36
3.3. Plane Wave on the Boundary of Adjacent Medium	39
3.3.1. One Dimensional FDTD	39
3.3.2. Oblique Incidence with Parallel Polarization	43
3.3.3. Oblique Incidence with Perpendicular Polarization	46
3.4. Discussion	47
3.4.1. Normally Incident Wave	47
3.4.2. Obliquely Incident Wave	48
3.5. Conclusion	61
4. HYBRID SYSTEM CO-SIMULATION MODEL	65
4.1. Introduction	65
4.2. Hybrid System Model	65
4.3. Modified Lumped Current Algorithm	67
4.4. Hybrid System Co-Simulation Model	71
4.5. Numerical Validation	74
4.5.1. Resistive Voltage Source and Capacitance Load	76
4.5.2. Resistive Voltage Source and Diode Load	78

TABLE OF CONTENTS
(continued)

Chapter	Page
4.5.3. Bipolar Junction Transistor Load	80
4.5.4. Short Pulse Generator	83
4.5.5. Diode Mixer	86
4.6. Conclusion	98
5. EXTENSION OF PML ABSORBING BOUNDARY CONDITION	100
5.1. Introduction	100
5.2. Generation of PML Layers for Inhomogeneous Boundary	102
5.3. Derivation of PML Equations	110
5.4. Numerical Validation	115
5.5. Conclusion	118
6. THE HYBRID SIMULATION APPLICATIONS	123
6.1. Introduction	123
6.2. Power Divider	124
6.3. Microstrip-Fed Patch Antenna	132
6.4. Spiral Inductor	140
6.5. Band Gap Transmission Line Loaded with Plated Through Holes	155
6.6. Conclusion	164
7. CONCLUSION	168
7.1. Contributions of the Dissertation	168
7.2. Limitations and Future work	170

TABLE OF CONTENTS
(continued)

Chapter	Page
REFERENCES	174

LIST OF TABLES

Table **Page**

6.1. PEC Type of Yee Cells..... 158

LIST OF FIGURES

Figure		Page
2.1.	Yee cell in three dimensional space.....	17
2.2.	Illustration of Ampere's Law in which J may contain the lumped current.....	23
2.3.	Illustration of Ampere's Law in which J may contain the lumped current in a FDTD grid.....	25
3.1.	Non-uniform FDTD grid and illustration of an integral form for the FDTD equation of Ez.....	37
3.2.	Parallel-polarization wave in the interface of two different media.....	41
3.3.	One–dimensional FDTD reflection coefficient, f=1GHz, $d_1=\lambda_1/20$, $\varepsilon_1=1$. Starting from the lowest pair of lines, $\varepsilon_2=2, 4, 6, \ldots, 16$. In each pair of curves, the theoretical solution is the dashed line parallel to ρ axis and the FDTD solution is the solid line. $\rho=d_2/d_1$.....	49
3.4.	One–dimensional FDTD reflection coefficient, f=1GHz, $dx=\lambda_1/10$, $\varepsilon_1=1$. Starting from the lowest pair of lines, $\varepsilon_2=2, 4, 6, \ldots, 16$. In each pair of curves, the theoretical solution is the dashed line parallel to ρ axis and the FDTD solution is the solid line. $\rho=d_2/d_1$.....	50
3.5.	Two–dimensional FDTD numerical transmission angle, f=1GHz, $dx_1=\lambda_1/10$, $\varepsilon_1=\varepsilon_2=1$, $dy_1=dy_2=dx_1$. From top to bottom, $\rho=0.2, 0.4, \ldots, 2$. $\rho=dx_2/dx_1$.....	52
3.6.	Two–dimensional FDTD numerical transmission angle, f=1GHz, $dx_1=\lambda_1/10$, $\varepsilon_2/\varepsilon_1=4$, and $dy_1=dy_2=dx_1$. Dashed line is the theoretical solution. $\rho=dx_2/dx_1$	53
3.7.	Two–dimensional FDTD numerical transmission angle, f=1GHz, $dx_1=\lambda_1/10$, $\varepsilon_2/\varepsilon_1=10$, and $dy_1=dy_2=dx_1$. Dashed line is the theoretical solution. $\rho= dx_2/dx$.....	54
3.8.	Two–dimensional FDTD numerical transmission angle, f=1GHz, $dx_1=\lambda_1/10$, $\varepsilon_2/\varepsilon_1=4$, and $dy_1=dy_2=2dx_1$. Dashed line is the theoretical solution. $\rho=dx_2/dx_1$.....	55
3.9.	FDTD numerical reflection coefficients of an EM wave in parallel polarization, f=1GHz, $dx_1=\lambda_1/10$, $\varepsilon_2/\varepsilon_1=1$, and $dy_1=dy_2=dx_1$. $\rho=dx_2/dx_1$.....	57

LIST OF FIGURES
(continued)

Figure **Page**

3.10. FDTD numerical reflection coefficients of an EM wave in parallel polarization, f=1GHz, $dx_1=\lambda_1/10$, $\varepsilon_2/\varepsilon_1=4$, and $dy_1=dy_2=dx_1$. The dashed line is the theoretical solution, and the solid lines are the FDTD numerical solutions. $\rho=dx_2/dx_1$ 58

3.11. FDTD numerical reflection coefficients of an EM wave in parallel polarization, f=1GHz, $dx_1=\lambda_1/10$, $\varepsilon_2/\varepsilon_1=4$, and $dy_1=dy_2=3dx_1$. The dashed line is the theoretical solution and the solid lines are the FDTD numerical solutions. $\rho=dx_2/dx_1$ 59

3.12. FDTD numerical reflection coefficients of an EM wave in parallel polarization, f=1GHz, $dx_1=\lambda_1/10$, $\varepsilon_2/\varepsilon_1=10$, and $dy_1=dy_2=dx_1$. The dashed line is the theoretical solution and the solid lines are the FDTD numerical solutions. $\rho=dx_2/dx_1$ 60

3.13. FDTD numerical reflection coefficients of an EM wave in perpendicular polarization, f=1GHz, $dx_1=\lambda_1/10$, $\varepsilon_2/\varepsilon_1=1$, and $dy_1=dy_2=dx_1$ 62

3.14. FDTD numerical reflection coefficients of an EM in perpendicular polarization, f=1GHz, $dx_1=\lambda_1/10$, $\varepsilon_2/\varepsilon_1=4$, and $dy_1=dy_2=dx_1$. Dashed line is the theoretical solution, and the solid lines are FDTD solutions, from top to bottom, the ratios of dx_2/dx_1 are 1, 0.8, 0.6, 0.4, and 0.2, respectively..... 63

3.15. FDTD numerical reflection coefficients of an EM wave in perpendicular polarization, f=1GHz, $dx_1=\lambda_1/10$, $\varepsilon_2/\varepsilon_1=10$, and $dy_1=dy_2=dx_1$. Dashed line is the theoretical solution, and the solid lines are FDTD solutions, from top to bottom, the ratios of dx_2/dx_1 are 1, 0.8, 0.6, 0.4, and 0.2, respectively..... 64

4.1. Field-circuit model for hybrid system co-simulation..... 73

4.2. A hybrid system configuration..... 75

4.3. Test Case 1: agreement of the co-simulation method and SPICE. Source: $R_s=0.001Z0$, $V_0=90V$, f=5GHz; transmission line in Figure 4.2: BD=0.06m, AB=0.008m, Z0=3.01379Ω; Load: C=1μF..... 77

4.4. The charging current to a capacitor by an exponential-rise resistive Dc voltage source. Rs=2Ω, Voltage source: V=1-exp(-t/τ), τ=1ns, and C is made a pair of parallel metal plates, 80mm*80mm*8mm, filled with air. Dashed line is the theoretical solution and the solid line is the co-simulation solution..... 79

LIST OF FIGURES
(continued)

Figure **Page**

4.5. Test case 2: Voltage profile of the Schottky diode load shown in Figure 4.2. Dashed line: SPICE solution. Solid line: co-simulation solution..... 81

4.6. Bipolar juncture transistor load. (a) a hybrid system. (b) Ebers-Moll model of Bipolar jucture transistor and the co-simulation model..... 82

4.7. Test case 3: Voltage profile of BE junction of the transistor load shown in Figure 4.6..... 84

4.8. Circuit structure of a narrow pulse generator. $Vs=V_0\sin 2\pi ft$, $V_0=90V$, $f=200MHz$, $Rs=3\Omega$, $L=1\mu H$, $AB=8mm$, $BD=30mm$, $\varepsilon_1=2$, $\varepsilon_2=4$, $\varepsilon_3=20$. Schottky Diode parameters are $I_0=0.5mA$ and $T=298K$..... 85

4.9. Voltage profile of the inductor shown in Figure 4.8 by co-simulation method..... 87

4.10. Illustration of a one-port mixer structure. $AB=0.06m$, $BC=0.12m$, $CD=0.008m$, $DE=0.032m$ and $Rs=Z0$; LO signal parameters are $f=10GHz$, $V0=10V$; RF signal parameters are $f=2GHz$, $V0=10V$; Schottky diode parameters are $I0=5mA$, $T=298K$; Load $R=Z0\Omega$..... 89

4.11. Illustration of a bandpass filter used in co-simulation..... 90

4.12. Simulation results of the mixer shown in Figure 4.10. Comparison of simulation results: Diode voltages from FDTD field-circuit model (solid line) and SPICE (dashed line) are both plotted..... 92

4.13. Simulation results of the mixer shown in Figure 4.10. Spectrum of voltage of the diode (before filter) obtained from FDTD field-circuit co-simulation model..... 93

4.14. Simulation results of the mixer shown in Figure 4.10. Spectrum of voltage of the diode (after filter) obtained from FDTD field-circuit co-simulation model..... 94

4.15. Illustration of a two-port input mixer structure with multiple-dielectric layers. $AB=0.003m$, $BC=0.002m$, $CD=0.0008m$, $EF=0.002m$. $\varepsilon1=20$, $\varepsilon2=4$, $\varepsilon3=2$; LO signal parameters are $f=100GHz$, $V0=5V$, $Rs=300\Omega$; RF signal parameters are $f=20GHz$, $V0=5V$, $Rs=300\Omega$; $R=266\Omega$..... 95

LIST OF FIGURES
(continued)

Figure **Page**

4.16. FDTD simulation results for the mixer shown in Figure 4.15. Spectrum of the mixing diode voltage..... 96

4.17. FDTD simulation results for the mixer shown in Figure 4.15. Spectrum of the load resistor voltage (after bandpass filter)..... 97

5.1. The construction of the electric loss of the PML cells..... 104

5.2. PML grid for non-uniform FDTD grid..... 109

5.3. Discretization scheme of PML equations. (a) EM subcomponent locates inside its corresponding PML layers, (b) EM subcomponent does not locates inside its corresponding PML layers..... 112

5.4. The microstrip line structure, (a) longitudinal view, (b) transverse view. D=10 cells, t=2 cells, W=12 cells, ε_1=6, ε_2=9, metal conductivity is 10^7 (S/m). P1, P2 are two observation points..... 116

5.5. PML error spectrum distribution of point P1 in Figure 5.4..... 120

5.6. PML error spectrum distribution of point P2 in Figure 5.4..... 121

5.7. Global error (the sum of square of E_x, E_y and E_z over all the Yee cells) versus time steps..... 122

6.1. Configuration of the microstrip line power divider. In the figure (unit: mm), W=1, W1=10, W2=48, W3=12, L1=20, L2=28, L3=32, H1=1, H2=5. The substrate permittivity is 9.07 and metal conductivity is 10^7mho/m. R=50ohm, Resistive voltage source: sinual wave with 900MHz frequency, Rs=50ohm..... 125

6.2. The waveform of the diode currents obtained from co-simulation and Ansoft Serenade package when the power divider is in balanced condition..... 126

6.3. The diagram of Ez distribution of the power divider shown in Figure 6.1 under a balanced condition..... 127

6.4. The contour of Ez distribution shown in Figure 6.3..... 128

6.5. The waveforms of the diode currents obtained from co-simulation when the power divider is in an unbalanced condition..... 129

LIST OF FIGURES
(continued)

Figure **Page**

6.6. The waveform of the diode currents obtained from co-simulation when the power divider is under an unbalanced condition and R is 10Ω..... 130

6.7. The contour of Ez distribution shown in Figure 6.3 when the two branches are not balanced..... 131

6.8. A microstrip-fed rectangular patched antenna (unit is mm)..... 133

6.9. FDTD mesh of the microstrip-fed rectangular patched antenna shown in Figure 6.8, (a) Source alignment (side view), (b) mesh configuration (top view)..... 135

6.10. S parameter extraction scheme from FDTD..... 139

6.11. S11 of the microstrip patch antenna shown in Figure 6.8. Solid line: measurement result, dashed line: result from [Sheen et al 1990], dotted: result of this dissertation..... 141

6.12. An impedance matching circuit with a spiral inductor and a lumped capacitor..... 143

6.13. FDTD numerical transmitting angle in a non-uniform grid, f=20GHz, dx1=265μm. Dashed line: theoretical solution, solid line: FDTD numerical solutions, from bottom to top, dx2=320, 160, 80, 40, 20, 10μm, ε=13..... 145

6.14. FDTD numerical reflection coefficient in a non-uniform grid, dx1=265μm. dx2=10μm, f=20GHz ε=13..... 146

6.15. Voltage of input signal vs time of the impedance matching circuit shown in Figure 6.12..... 148

6.16. Voltage of total signal vs time of the impedance matching circuit shown in Figure 6.12..... 149

6.17. S11 diagram obtained directly from simulation to the impedance matching circuit shown in Figure 6.12 150

6.18. S21 diagram obtained directly from the co-simulation to the impedance matching circuit shown in Figure 6.12..... 151

LIST OF FIGURES
(continued)

Figure **Page**

6.19. S11 diagrams of measurement and simulation results of the impedance matching circuit shown in Figure 6.12, and the latter is obtained after a phase compensation, (a) Magnitude of S11, (b) Real and imaginary parts of S11..... 152

6.20. S21 diagrams of measurement and simulation results of the impedance matching circuit shown in Figure 6.12, and the latter is obtained after a phase compensation, (a) Magnitude of S21, (b) Real and imaginary parts of S21..... 153

6.21. S11 of the impedance matching circuit shown in Figure 6.12 with a doubled lumped capacitor (C=2.7pF)..... 156

6.22. Micristrip band-pass filter with cylindrical holes through the substrate..... 157

6.23. Varactor model in co-simulation. (a) simple varactor model with bias circuit. (b) field-circuit model in small AC signals. the circuit in the dashed box is the varactor and bias circuit..... 160

6.24. Comparison of the FDTD and IE3D simulation to Micristrip band-pass filter with 3 cylindrical holes through the substrate. 'o' and '+' points are the results from IE3D..... 162

6.25. Te FDTD simulation results of microstrip band-pass filter with three cylindrical holes through the substrate. It shows that the different dielectric media in the cylinder has the tuning function..... 163

6.26. The co-simulation results of microstrip band-pass filter with three cylindrical holes through the substrate. It shows that the varactors in the filter has the tuning function..... 165

6.27. The FDTD simulation results of microstrip band-pass filter with three (a) and seven (b) cylindrical holes through the substrate..... 166

LIST OF ABBREVIATIONS

ABCs	Absorbing Boundary Conditions
ADE	Auxiliary Deferential Equation
AR	Auto-Regressive
BJT	Bipolar Juncture Transistor
CAD	Computer Aided Design
CFL	Courant-Friedrichs-Lewy
DFT	Digital Fourier Transform
EDA	Electronic Design Automation
EE	Electrical Engineering
EM	Electromagnetic
FDTD	Finite-difference Time-Domain
FFT	Fast Fourier Transform
IF	Intermediate Frequency
LO	Local Oscillation
MIC	Microwave Integrated Circuit
MMIC	Monolithic Microwave Integrated Circuit
MoM	Method of Moment
NN	Neural Network
PCS	Personal Communication Service
PEC	Perfect Electrical Conductor
PML	Perfectly Matched Layer
RC	Recursive Convolution

LIST OF ABBREVIATIONS
(continued)

RF	Radio Frequency
SIBCs	Surface Impedance Boundary Conditions

LIST OF SYMBOLS

E	electrical intensity vector
H	magnetic intensity vector
E_x, E_y, E_z	electrical intensity components
H_x, H_y, H_z	magnetic intensity components
x, y. z	Three axis of Cartesian coordinates
i, j, k	spatial index of FDTD grid
n	temporal index of FDTD iteration
dx, dy, dz	space step of FDTD grid
dt	temporal increment of FDTD iteration
ε_0 , ε	permittivity of free space and a medium
μ_0 , μ	permeability of free space and a medium
σ	conductivity of a medium
σ_x, σ_y, σ_z	PML electric loss
σ^*_x, σ^*_y, σ^*_z	PML magnetic loss
λ	Wavelength
f	frequency
ω	angular frequency
c_0 c	electromagnetic wave phase speed in free space and in a medium
k	electromagnetic wave number in a medium
I	current
V	Voltage

LIST OF SYMBOLS
(continued)

R	resistor or the reflecting coefficient
C	capacitor
L	inductor
t_w	Gaussian pulse width
t_d	Gausian pulse delay
N	Number of PML layers
g	factor of geometric PML loss profile
θ_I, θ_t, θ_r	incident angle, transmitting angle and reflecting angle
ξ	characteristic impedance of a medium
ϕ, ψ	intermediate variables explained with the equations.

CHAPTER 1

INTRODUCTION

1.1 Motivation

In the design of high-frequency electronic systems such as radio frequency (RF), microwave and optical wave devices, computer aided design (CAD) plays an important role in improving their performance and reducing their development cost. Much electrical design automation (EDA) software is essential in the design and analysis analog and digital systems. Simulation is an essential step in the analysis and design procedure. A good simulation will expose and fix most problems during the development stage of a prototype system.

However, as the frequencies of signals rise higher and higher, system designers find the simulation of the system gets more difficult than ever. Traditionally, the simulation of a electrical is done by circuit methods, in which all components in the system are simplified by lumped element. Under this simplification, the system is called a lumped circuit. Lumped circuit, described by circuit theory, is a low-frequency approximation of a practical electromagnetic (EM) system. In circuit simulation the connections between components are either ignored or represented by an empirical model, like a transmission line or an LCR network. At present, widely used EDA software in industrials, such as SPICE®, Serenade®, Libra®, Celerity®, etc, are essentially applications of circuit simulation models. Although in those packages, there are some distributed components, such as microstrip line, T-shape connector, spiral inductor, and strip line corner, the

fundamental simulation concept is still built on the circuit model, i. e. the components are separated and general field effects are not completely included.

Today's EM systems have increasingly complicated structures, in which the field effects show additionally important influences on system characteristics and performance. However, the circuit method has inherent difficulties in demonstrating field effects. It is well known that, in the high-frequency range, many properties of a system are influenced by its distributed parameters, such as the physical dimensions, the media used and the positions of components. All those factors are very difficult if not possible to be handled in the traditional circuit-based simulation methods. Furthermore, the characteristics of a lumped component depend upon the interaction between the lumped component and the EM field around it. This dependence is significant for the time-domain behavior of a system. The phenomena caused by field effects have become the dominant concerns in RFIC and MMIC designs.

Thus, an appropriate simulation model for handling field effects is essential to the circuit designers, because the presently used circuit simulators can no longer satisfactorily fulfill the requirements of the analysis and design of high-frequency EM systems. Due to lack of the appropriate simulation tools, present practice is based on trial and error methods. Much of the design cost can be alleviated with the help of a full-wave solution based simulation, which can describe the field effects and the interaction between the lumped components and their surrounding EM field.

Finite-difference time-domain (FDTD) is a widely used numerical simulation method used in the design and analysis EM systems, such as antennas, wave propagating, biomedical applications, and microwave circuits. It provides a full-wave solution to an

EM structure. Generally speaking, FDTD is shown to be a versatile and powerful tool and has gained a positive reputation in the study of EM wave propagation based on the following several essential attributes. First, the Maxwell's equations are discretized in a straightforward manner to provide a precise description of the EM system. Second, FDTD provides a visualized time-domain solution to the EM process and also gives a transient response of the system. Third, this method is very flexible and can be applied to some complicated structures with many medium types and geometric shapes.

Because of these outstanding properties, FDTD is a good candidate to be used in a high-frequency system simulation model to handle the field effects in the system. Because practical EM systems have lumped components and distributed structures, this model has to simulate lumped components and the EM field at the same time. Thus it is a hybrid simulation model that includes a FDTD simulation as well as a circuit simulation.

This dissertation builds an appropriate hybrid model for the RF or microwave system analysis. Some modifications of previous work about FDTD methodologies and implementation schemes are accomplished to improve the simulation performance.

1.2 Literature Review of FDTD Related Topic

1.2.1 FDTD method and Applications

In 1966, Yee proposed a numerical algorithm for the time-domain solution of Maxwell's equations [Yee 1966]. This method is currently known as the Finite-Difference Time-Domain (FDTD). This method discretizes the Maxwell's equations by a grid, which is made of Yee cells. Although FDTD was mathematically simple and can be easily

implemented, it did not gain much attention immediately after its initial publication because of its high computational cost and some inherent limitations at that time.

With the drastic increasing of the computing capability, people began to realize that FDTD had some obvious advantages over other numerical methods within the computable capability. In 1975, FDTD was initially used to solve the EM scattering problem by Taflove [Taflove 1975], which is the first break-through in the FDTD developing history. In that paper, some critical problems were solved or improved. The correct derivation of the stability criterion was demonstrated; the lattice truncation conditions were proposed to handle the unbounded boundary. This could be treated as the prototype of Absorbing Boundary conditions (ABCs); and the soft excitation was proposed to simulate an EM source transparent to EM waves.

Since then, researchers have been interested in FDTD and it has been enhanced in many aspects. Generally, the development of FDTD falls into three categories: fundamental issues, extension, and practical applications.

The fundamental issues are addressed to overcome some inherent disadvantages of the prototyped FDTD proposed by Yee.

The open space problems need a boundary condition to define the computational domain within a finite range. Absorbing boundary conditions (ABCs) [Engquist and Majda 1977, Lindman 1975, Bayliss 1980 1981, Mur 1981, Berenger 1994] were proposed to describe an EM wave propagating out of the computational domain without reflection. Especially Mur's ABCs [Mur 1981] and Berenger's perfectly matched layer (PML) [Berenger 1994] essentially solved the problems of boundary conditions in FDTD.

Because of the introduction of the FDTD grid, the dispersion relation in the FDTD solution is different from the analytic one. Taflove (1988), Choi (1989), Kim and Hoefer (1990) analyzed the numerical errors in the FDTD solution and showed the relation of the numerical error and such FDTD parameters as cell size and temporal increment. In order to reduce the dispersion error, high order FDTD techniques [Fang 1989, Deveze et al 1992] were proposed for high accuracy applications.

Most FDTD developments fall into the second category, the extension of FDTD in its practical implementation.

The non-uniform orthogonal FDTD grid was introduced by Sheen [1991]. Monk and Suli [1994] proved that although in an arbitrary non-uniform orthogonal grid FDTD can only provide a numerical solution in first order accuracy locally, it results in second order accuracy globally. Holland [1983] proposed an FDTD algorithm in generalized non-orthogonal coordinates. The conformal techniques are also developed to model the curved surface in Cartesian coordinates [Mei et al 1984, Yee et al 1992, Jurgens and Taflove 1993, Gedney et al 1996].

Lumped elements were modeled into the FDTD formulation by adding an additional current term, named lumped current, in the Ampere's Law [Sui et al 1992, Picket-May et al 1993]. Then a lumped-voltage approach based on the variation of Faraday's Law was proposed to model lumped elements [Kuo et al 1996]. The lumped-element modeling has gained many attentions in terms of numerical performance and applications [Thomas et al 1994, Zhao 1997, Durney et al 1994, Gedney et al 1996, Kuo et al 1995, 1996, and 1997].

Frequency-dispersive material is also modeled in the FDTD formulation by a recurvise convolution (RC) method [Luebber et al 1990 1991] and an auxiliary

differential equation (ADE) method [Kashiwa et al 1990]. The surface impedance boundary conditions (SIBCs) were modeled into FDTD thus reduce its computational burden when modeling the skin effect inside lossy media [Maloney and Smith 1992, Beggs et al 1992, Lee et al 1992]. Near to far field transformations were added into the FDTD simulation to efficiently yield the far field pattern [Yee et al 1991, Luebbers et al 1991].

With these methodological improvements and extensions, FDTD has been applied to increasingly large areas, such as scattering problems, antenna analysis, microwave structure analysis, electronic packaging, photonics, biomedical, and acoustics.

Up to the present, there is a large literature related to FDTD. Shlager and Schneider [1995] maintain an on-line database contains bibliographic information about most FDTD publications. Its web site is http://www.eecs.wsu.edu/~schneid/fdtd-bib.html.

The three basic research issues discussed in this dissertation are the lumped element modeling, ABCs, and the numerical dispersion of FDTD. Existing research progress is reviewed briefly in the following sections.

1.2.2 Lumped Current Algorithm

Because of the existence of lumped components in an EM system, the passive and active lumped elements have to be modeled in the FDTD formulation. In the distributed system simulation level, the interaction between lumped elements and their surrounding EM field has be to modeled, nevertheless the EM field inside the lumped elements does not to be simulated. The FDTD simulation was first extended to include the lumped elements in two-dimensional domains [Sui et al 1992], in which the lumped element is replaced by an

additional lumped current term in Ampere's Law. By this method, the effect of linear and nonlinear lumped components can be simulated by the FDTD. Many researchers used the lumped current algorithm in their applications. Later, a dual method, which was called lumped voltage algorithm, was proposed to handle the lumped element [Kuo et al 1996]. Conceptually, these two methods are the same.

Since then, lumped current algorithm has been further extended to three-dimensional FDTD simulation [Piket-May 1993] and multiple-cell formulation [Durney et al 1996]. It was improved in stability for nonlinear systems [Toland et al 1994, Kuo et al 1995 Ciampolini et al 1996, Xu et al 1997]. The applications of the lumped current algorithm in many systems were published [Thomas and Lin et al 1994, Kuo et al 1995, Gedney et al 1996, Chen et al 1997 1998, Rosilli et al 1998].

Multiple-cell FDTD formulation for lumped current algorithm is very important for structures with stacked dielectric and metal layers where electrical field distribution is not uniform. A simple example would be, in a suspended microstrip line system, to model a lumped element across the stripline and its ground plane. When a lumped element is across non-uniform or uniform media, the spatial field distribution is not uniform in most cases. Durney et al (1994) proposed an explicit FDTD formulation for a lumped element crossing multiple cells, however it has stability problems in certain situations. Piket-May et al (1996) and Xu et al (1997) suggested using a semi-implicit descritization method to improve the stability, but it would compromise the computational efficiency. Ciampolini et al (1996) proposed an adaptive time step approach to improve the efficiency.

Because of the additional lumped current term, the FDTD stability is changed even when the lumped element is just a linear resistor. Stability is thus a essential problem for

the implementation of lumped current algorithm. Sometimes numerical efficiency has to be compromised in exchange for stable solutions [Ciamponili et al 1996]. In order to overcome the non-stability of the lumped current algorithm, many methods were proposed. Toland et al (1994) used the Tayor's series to extend the nonlinear VI relation of the lumped components. Campolini et al (1996) used the adaptive temporal increment, Piket-May et al (1996) used the average of the electrical field to represent the lumped voltage.

In an attempt to take advantage of the existing SPICE and SPICE-like analog circuit simulators, especially their rich model resources, lumped circuits were modeled as an FDTD sub-grid in SPICE analysis [Thomas et al 1994], but it remains as a single-cell formulation by assuming uniform field distribution.

1.2.3 Absorbing Boundary Conditions (ABCs)

The open space boundary conditions, which is also called absorbing boundary conditions (ABCs), used to be an obstacle in keeping FDTD from many applications. Many techniques were proposed to solve this problem. One of the important early techniques using ABCs is radiation conditions [Bayliss et al 1980]. Because it is not easy to be used in Cartesian coordinates, it was left unused. The first breakthrough of ABCs was the one-way approximation of the wave equation which was initially proposed in [Engquist and Majda 1977] for acoustic wave equations. Mur first applied this solution in FDTD [Mur 1981]. After Mur's publication, much work was expended to improve its performance [Halpern and Trefethen 1986, Higdon 1987, Liao et al 1984, Mei and Fang 1992]. All of

these the approaches based on the one-way wave approximation were called differential equation based ABCs, which is still very much in use today.

A new more accurate ABCs technique was proposed several years ago. In 1994, Berenger proposed his perfectly matched layer (PML) absorbing conditions in free space [Berenger 1994]. PML belongs to the material based ABCs. Compared with other ABCs, PML provides a much higher absorption to EM waves propagating obliquely towards the boundary. PML make it possible to accurately analyze an EM structure involving complicated wave propagation in three-dimensional domain. Immediately after its publication, PML gained a wide attention from the FDTD community. Various formulations of PML were proposed to improve its performance [Berenger 1996, Veihl and Mittra 1996, Fang et al 1996, Sullivan 1996, Zhao et al 1996]. It was implemented to truncate the guided-wave structures [Reuter et al 1994 1995] and multi-layered structures [Bahr et al 1995, Spillard et al 1995, Oguz et al 1997]. Additional research has applied PML to evanescent waves [Moerloose 1995, Chew and Jin 1996, Berenger 1997] and lossey media [Lau et al, 1996]. The internal physical meaning of PML was also discussed in order to further development of this material into other uses other than boundary conditions [Mittra and Pekel 1995].

1.2.4 Numerical Error and Dispersion

The original FDTD method is second-order accurate in both space and time. Like all the numerical methods, the accuracy of FDTD depends on its discretization scheme and grid distribution.

The numerical error and dispersion relation of the standard FDTD method was analyzed in [Taflove 1988, Choi 1989, Kim and Hoefer 1990]. The global second-order convergence of non-uniformed FDTD grid was verified [Monk 1994]. Because of the complexity of a practical EM system with inhomogeneous media, general evaluation of FDTD numerical errors is very difficult. Presently, in terms of numerical errors, researchers generally implement FDTD empirically into the inhomogeneous media.

The comparison of some higher order FDTD methods to second-order FDTD was presented [Shlager et al 1993].

1.3 Objective of This Dissertation

1.3.1 Limitations of Previous Work

As mentioned above, much work has been performed utilizing FDTD in EM system analysis. However, FDTD is not mature enough to be implemented and utilized in many realistic problems. In order to implement FDTD more accurately and efficiently for the analysis of a hybrid system, additional improvements have to be made.

First the lumped current algorithm has to be improved to be more robust and flexible. It is hoped that the extra lumped current term in Maxwell's equation would not compromise the computational cost, which is already high. The lumped current algorithm should handle the lumped element across multiple cells in which different media may fill. The non-uniformed FDTD grid should also be included into the lumped current formulation.

One important thing about the formulation of lumped elements is that the cooperation between the circuit simulation and field simulation has to be arranged in a general

scheme. In this formulation of lumped elements, no matter what kind of a hybrid system, the simulation will be processed uniformly. Because FDTD is a computationally intensive method, in order to take the advantage of parallel computing, this formulation should provide a convenient way to allow parallel computing.

Because an EM structure is normally filled with inhomogeneous media, the numerical EM wave behavior in the media has to be investigated in order to decide the FDTD grid and temporal parameters properly. This point is especially important to an FDTD simulation in a non-uniform grid.

The boundary conditions have to be modified to fit a complicated EM structure. In the two-dimensional FDTD simulation, second-order Mur ABCs are good for most cases and first-order Mur ABCs still can provide a satisfactory result in many cases. But for the three-dimensional FDTD simulation, in the case of a multi-layered structure and other complicated structures, PML boundary has to be utilized into FDTD. Because of the complexity of practical EM structures, non-uniformed FDTD grid is normally necessary. Thus, for an inhomogeneous boundary and a non-uniform FDTD grid, the previous PML has to be modified to handle the more complicated boundary situation to achieve the comparable performance with that in homogeneous boundary and uniform grid.

1.3.2 Field-Circuit Model for Hybrid System Co-Simulation

A hybrid system is defined as a system consisting of distributed components, such as microstrip line, multi-layered board or waveguide, and lumped components, such as resistors, capacitors, diodes, transistors, etc. The field effects can play a very important role in such a hybrid system.

This dissertation is dedicated to an FDTD simulation methodology of a hybrid system. Both circuit simulation and FDTD are utilized to handle the lumped elements and EM field in the system, respectively. The following topics are discussed in this dissertation.

First, a field-circuit co-simulation model is proposed based on a modified lumped current algorithm. The modified lumped current algorithm is robust and flexible. It can be used in a general non-uniformed FDTD grid with inhomogeneous media filled in. Based on this, the field-circuit co-simulation model combines the circuit simulation and FDTD simulation in a flexible manner so that these two simulations can cooperate with each other to solve hybrid system problems seamlessly. The derivation, discussion and verification of this model are in Chapter 4.

Second, the FDTD numerical dispersion error on the interface of two different media is investigated. Based on the derived FDTD numerical reflection coefficient formulation, suggestions are proposed to decide cell sizes of a non-uniform FDTD grid. Although results are obtained for relatively simple situations, they provide important information to improve the accuracy of the FDTD simulation of some complicated structures. The detailed derivation and discussion in one-dimensional and two-dimensional FDTD grids are presented in Chapter 3.

Third, the PML boundary conditions are modified to truncate the EM system in some places in order to have a reasonable computational cost. The boundary is inhomogeneous, which consists of metals, dielectric media with different permittivity or permeability. The boundary cells are non-uniformed. Chapter 5 is devoted to describe a extension of PML

boundary conditions to inhomogeneous media in a three-dimensional non-uniform FDTD grid.

Fourth, the lumped characteristics of an EM system, such as scattering (S) parameters, impedance, spectrum response, can be extracted from the FDTD simulation. In order to get those parameters, some supplementary issues, such as excitation types, probing positions, and DFT methods, have to be considered carefully. These considerations not only help us obtain the valuable information from the FDTD simulation, but also gain new insight into numerical FDTD methods and EM wave behaviors. In Chapter 6, several three-dimensional simulation examples are given to demonstrate the implementation of the FDTD based co-simulation model and also the extraction of S parameters from the FDTD simulation are discussed.

Many important topics for future studies can be included in the proposed co-simulation model, such as non-orthogonal griding, anisotropic media modeling and nonlinear media modeling. The purpose of this dissertation is to address some essential solutions to the hybrid-system simulation, in which lumped elements modeling, circuit and FDTD simulation cooperation, FDTD numerical error, PML boundary conditions, and some FDTD numerical experiment settings are studies. With a great potential for future expansion, it aims to provide a basic co-simulation model for hybrid systems. It has many applications in practical analysis and design, such as filter design, packaging design, antenna design, microstrip line modeling, mixer, amplifier, pulse generator, and power divider sutdies. The outcome of this work will be beneficial to the researchers and engineers in the area of analysis and design of high-frequency systems.

1.4 Conclusion

High-frequency EM system design and analysis need to take the field effects into consideration during simulation. To date, there is no commercial simulation software to completely include the field effects. As an excellent full-wave simulation method, with decades of development, FDTD has many good properties to be utilized in the high-frequency circuit simulation. Although there are already some progress in this aspect, a number of limitations have to be overcome to reach such goals to put it into commercial usage.

This dissertation aims to provide several important improvements in this direction. Most important one is the field-circuit model for hybrid co-simulation model, with which the FDTD simulation and circuit simulation cooperate seamlessly.

Chapter 2 gives a brief overview of the fundamentals in the FDTD theory and some related topics. Chapter 3-6 demonstrate the field-circuit co-simulation model other related topics. Chapter 7 presents the contributions and limitations of our work and future researching topics about the hybrid system analysis.

CHAPTER 2

OVERVIEW OF FDTD AND RELATED TOPICS

2.1. Introduction

In order to introduce a complete concept of FDTD and some topics related to the hybrid system analysis, this chapter is devoted to provide fundamental theories of FDTD methods and issues related to the work of this dissertation. Details about FDTD can be found in [Taflove et al 1995], which provides the formulation and discussions of important aspects of FDTD.

2.2. Fundamental FDTD Method

2.2.1. Yee Algorithm

It is well known that the Maxwell's equations are sufficient mathematical description of all electromagnetic phenomena from the point of view of the classical electromagnetic theory. Let's start from the Maxwell's curl equations.

$$\frac{\partial \boldsymbol{D}}{\partial t} = \nabla \times \boldsymbol{H} - \boldsymbol{J} \tag{2.1}$$

$$\frac{\partial \boldsymbol{B}}{\partial t} = -\nabla \times \boldsymbol{E} \tag{2.2}$$

In linear, isotropic, time-invariant, non-dispersive media, the Maxwell's curl equations can be written as

$$\varepsilon \frac{\partial \boldsymbol{E}}{\partial t} = \nabla \times \boldsymbol{H} - \boldsymbol{J} \tag{2.3}$$

$$\mu \frac{\partial \boldsymbol{H}}{\partial t} = -\nabla \times \boldsymbol{E} \tag{2.4}$$

In Cartesian coordinates, (2.3) and (2.4) can be rewritten as an equation system for all the electromagnetic field components

$$\varepsilon \frac{\partial E_x}{\partial t} = \frac{\partial H_z}{\partial y} - \frac{\partial H_y}{\partial z} - J_x \tag{2.5}$$

$$\varepsilon \frac{\partial E_y}{\partial t} = \frac{\partial H_x}{\partial z} - \frac{\partial H_z}{\partial x} - J_y \tag{2.6}$$

$$\varepsilon \frac{\partial E_z}{\partial t} = \frac{\partial H_y}{\partial x} - \frac{\partial H_x}{\partial y} - J_z \tag{2.7}$$

$$-\mu \frac{\partial H_x}{\partial t} = \frac{\partial E_z}{\partial y} - \frac{\partial E_y}{\partial z} \tag{2.8}$$

$$-\mu \frac{\partial H_y}{\partial t} = \frac{\partial E_x}{\partial z} - \frac{\partial E_z}{\partial x} \tag{2.9}$$

$$-\mu \frac{\partial H_z}{\partial t} = \frac{\partial E_y}{\partial x} - \frac{\partial E_x}{\partial y} \tag{2.10}$$

The FDTD method is a finite difference method starting from Maxwell's equations directly. A centered difference scheme is utilized to approximate the derivations in time and space. This method has second-order accuracy in both time and space.

In order to apply the second-order centered difference scheme, a special spatial discretization scheme named Yee cell, shown in Figure 2.1, is used in FDTD method to discretize the equations (2.5-10). In FDTD, the placements of the electromagnetic field components are off the grid nodes of one half-cell size. In Figure 2.1, the arrangement of the positions of E and H components is for the purpose to locate the electrical media more conveniently. In order to locate the magnetic media conveniently, the positions of E and H components can be exchanged. This does not change the FDTD equations at all. In time domain, the E and H components are also defined at different time instants.

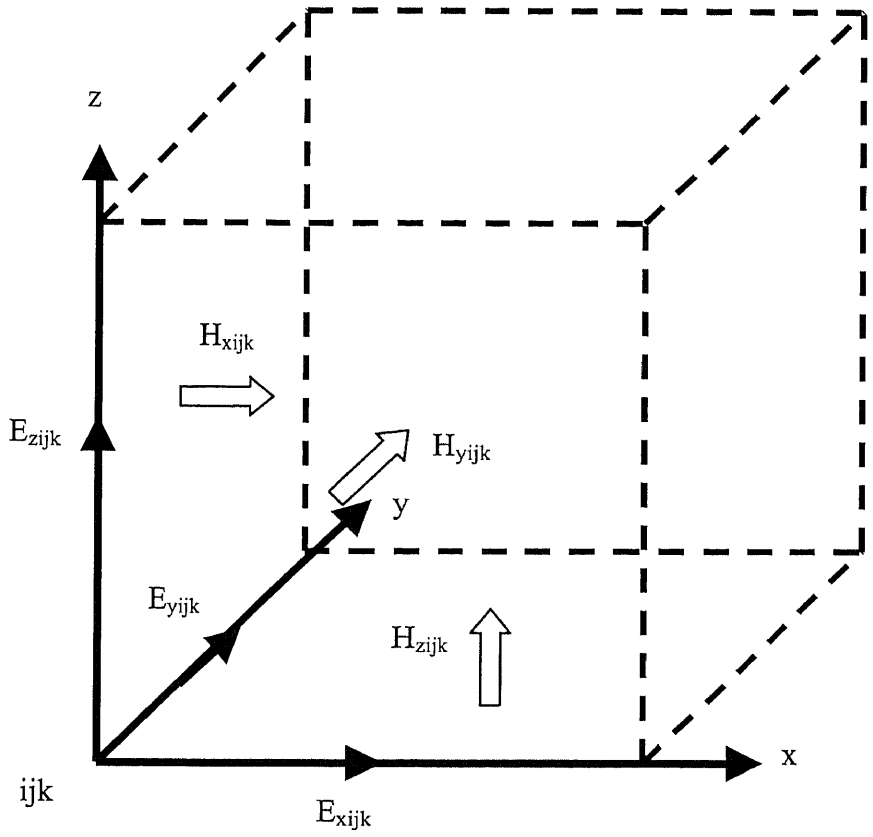

Figure 2.1 Yee cell in three-dimensional space.

Specifically, the E field is defined at the ndt and the H field is defined at (n+1/2)dt, n is a non-negative integer and dt is the temporal increment.

In case of a homogeneous medium with uniform cell size and only conduction current included, the discrete forms of equations (2.5-10) are

$$E_{xijk}^{n+1} = \frac{\frac{dt}{\varepsilon} - \frac{\sigma}{2}}{\frac{dt}{\varepsilon} + \frac{\sigma}{2}} E_{xijk}^{n} + \frac{1}{\frac{dt}{\varepsilon} + \frac{\sigma}{2}} \left(\frac{H_{zijk}^{n+1/2} - H_{zij-1k}^{n+1/2}}{dy} - \frac{H_{yijk}^{n+1/2} - H_{yijk-1}^{n+1/2}}{dz} \right) \tag{2.11}$$

$$E_{yijk}^{n+1} = \frac{\frac{dt}{\varepsilon} - \frac{\sigma}{2}}{\frac{dt}{\varepsilon} + \frac{\sigma}{2}} E_{yijk}^{n} + \frac{1}{\frac{dt}{\varepsilon} + \frac{\sigma}{2}} \left(\frac{H_{xijk}^{n+1/2} - H_{xijk-1}^{n+1/2}}{dz} - \frac{H_{zijk}^{n+1/2} - H_{zi-1jk}^{n+1/2}}{dx} \right) \tag{2.12}$$

$$E_{zijk}^{n+1} = \frac{\frac{dt}{\varepsilon} - \frac{\sigma}{2}}{\frac{dt}{\varepsilon} + \frac{\sigma}{2}} E_{zijk}^{n} + \frac{1}{\frac{dt}{\varepsilon} + \frac{\sigma}{2}} \left(\frac{H_{yijk}^{n+1/2} - H_{yi-1jk}^{n+1/2}}{dx} - \frac{H_{xijk}^{n+1/2} - H_{xij-1k}^{n+1/2}}{dy} \right) \tag{2.13}$$

$$H_{xijk}^{n+1/2} = H_{xijk}^{n-1/2} - \frac{dt}{\mu} \left(\frac{E_{zij+1k}^{n} - E_{zijk}^{n}}{dy} - \frac{E_{yijk+1}^{n} - E_{yijk}^{n}}{dz} \right) \tag{2.14}$$

$$H_{yijk}^{n+1/2} = H_{yijk}^{n-1/2} - \frac{dt}{\mu} \left(\frac{E_{xijk+1}^{n} - E_{xijk}^{n}}{dz} - \frac{E_{zi+1jk}^{n} - E_{zijk}^{n}}{dx} \right) \tag{2.15}$$

$$H_{zijk}^{n+1/2} = H_{zijk}^{n-1/2} - \frac{dt}{\mu} \left(\frac{E_{yi+1jk}^{n} - E_{yijk}^{n}}{dx} - \frac{E_{xij+1k}^{n} - E_{xijk}^{n}}{dy} \right) \tag{2.16}$$

in which the conduction current is evaluated as $J=\sigma(E^n+E^{n+1})/2$.

From (2.11) to (2.16), once the initial condition is given, every E component can be calculated based on its value in previous time step and H field values around it in half time step before. Every H field component can also be computed according to its value in previous time step and the E field values around it in half time step before. Thus, this scheme is also called leapfrog scheme.

Up to now, we have only consider the Maxwell's curl equations while ignoring the divergence equations. According to the electromagnetic theory, the Maxwell's divergence equations can automatically be satisfied under a continuous analytical case. This point remains true under an FDTD discretization scheme.

2.2.2. Numerical Dispersion

As a numerical method, FDTD describes the electromagnetic wave propagation by discrete forms instead of continuous differential equations, i.e. Maxwell's equations. Hence the numerical error, consists of cumulated error and discretization error, has to be considered. Because of the double precision variables used, the cumulated error is normally ignored. Here, the discretization error is considered as the whole numerical error. This error is expressed as the FDTD numerical dispersion relation, which will be explained in detail in Chapter 3.

A plane electromagnetic wave travels through an area filled by FDTD cells. Its angular frequency is ω and wave number k. The analytical relation between ω and k is

$$(\frac{\omega}{c})^2 = k^2 \tag{2.17}$$

in which c is the wave speed in this medium.

The dispersion relation yielded by an FDTD method is:

$$\frac{1}{(cdt)^2}\sin^2(\frac{\omega dt}{2}) = \frac{1}{dx^2}\sin^2(\frac{kdx}{2}) \tag{2.18}$$

$$\frac{1}{(cdt)^2}\sin^2(\frac{\omega dt}{2}) = \frac{1}{dx^2}\sin^2(\frac{k_x dx}{2}) + \frac{1}{dy^2}\sin^2(\frac{k_y dy}{2}) \tag{2.19}$$

$$\frac{1}{(cdt)^2}\sin^2(\frac{\omega dt}{2}) = \frac{1}{dx^2}\sin^2(\frac{k_x dx}{2}) + \frac{1}{dy^2}\sin^2(\frac{k_y dy}{2}) + \frac{1}{dz^2}\sin^2(\frac{k_z dy}{2}) \tag{2.20}$$

(2.18) (2.19) and (2.20) are the dispersion relation of FDTD method in 1D, 2D, and 3D cases, respectively.

If the time step dt is chosen to be dx/c, (2.18) is identical to (2.17). This means under a specific time step, in inhomogeneous media and uniform 1D FDTD grid, the FDTD numerical solution is the same as the analytical one. So dt=dx/c is also called magic time step.

However, 2D or 3D FDTD simulations, which have more practical applications, can not produce the exact solution no matter how the cell size is chosen. The FDTD numerical error is related to the FDTD cell sizes and time step. As shown in (2.18) and (2.19), the relation between the error and FDTD cell size is not linear. The reduction of cell size from coarse mesh to fine mesh can reduce the FDTD error significantly, but further reduction of the cell size will not give a worthy error reduction with respect to the increasing computational cost. Generally, the selection of the FDTD cell size depends on the wavelength in the media. Empirically, A FDTD grid with the cell size of l/20 wavelength is called a fine mesh, one with the cell size of 1/5 wavelength is called a coarse mesh, and one with the cell size of 1/10 wavelength is an intermediate mesh. The above suggestion is just for the general case. In case of complicated structures, such as taper or corner geometry, where will generate complicated high order mode patterns in a near field, the cell size has to be finer than l/20.

2.2.3. Stability Criterion

One of the advantages of the FDTD method obtained from Yee cells is that it can get an explicit second-order accuracy discrete scheme to the wave propagation solution without

any assumption. The explicit scheme needs much smaller memory compared to that of an implicit scheme, which is difficult to manipulate a huge matrix in 3D problems. However, like all the explicit solution, FDTD is stable under certain conditions.

The stability criteria of FDTD methods are [Taflove, 1995]

$$cdt \leq dx \tag{2.21}$$

$$cdt \leq \frac{1}{(\frac{1}{dx^2}+\frac{1}{dy^2})^{1/2}} \tag{2.22}$$

$$cdt \leq \frac{1}{(\frac{1}{dx^2}+\frac{1}{dy^2}+\frac{1}{dz^2})^{1/2}} \tag{2.21}$$

For 1D, 2D and 3D FDTD methods respectively. They are also known as Courant-Friedrichs-Lewy (CFL) stability criterion.

The CFL stability criterion gives the limitation of time step in FDTD simulation. The time step has to be smaller than the time duration in which the wave propagates across a grid length. To an EM process with a relative long period, the FDTD iteration number could become extremely large. This requirement, in turn, demands huge computational effort. This limitation might be the biggest disadvantage of the FDTD method.

2.3. Lumped Current Algorithm

Originally, FDTD was developed to be an approach to solve the electromagnetic wave propagation problems. Nevertheless in many practical distributed systems, there are some lumped devices embedded in them. The modeling of the interaction between the lumped element and the electromagnetic field was a problem limiting the applications of FDTD

to such hybrid systems. The lumped current algorithm was proposed to resolve this problem [Sui et al 1992].

Rewrite the Maxwell's curl equations in an integral form, which is equivalent to the differential form.

$$\oint_C \boldsymbol{E} \bullet d\boldsymbol{l} = -\iint_S \mu \frac{\partial \boldsymbol{H}}{\partial t} \bullet d\boldsymbol{S} \tag{2.22}$$

$$\oint_C \boldsymbol{H} \bullet d\boldsymbol{l} = \iint_S \boldsymbol{J} \bullet d\boldsymbol{S} + \iint_S \varepsilon \frac{\partial \boldsymbol{E}}{\partial t} \bullet d\boldsymbol{S} \tag{2.23}$$

The first term in the right-hand side of (2.23) represents the total current flowing through the surface S, as shown in Figure 2.2. The current would consist of conduction current, convection current and so-called lumped current. The lumped current is the current caused by the lumped element embedded in an electromagnetic system. The fundamental idea of the lumped current algorithm is to use the lumped current as the representative of a lumped element in Maxwell's equations. All the effects of a lumped element will be represented by the behavior of the lumped current.

Consider a homogeneous medium and uniform FDTD grid in which only conduction current and lumped current exist, the FDTD equations (2.11) to (2.13) can be rewritten as

$$E_{xijk}^{n+1} = \frac{\frac{dt}{\varepsilon} - \frac{\sigma}{2}}{\frac{dt}{\varepsilon} + \frac{\sigma}{2}} E_{xijk}^{n} + \frac{1}{\frac{dt}{\varepsilon} + \frac{\sigma}{2}} \left(\frac{H_{zijk}^{n+1/2} - H_{zij-1k}^{n+1/2}}{dy} - \frac{H_{yijk}^{n+1/2} - H_{yijk-1}^{n+1/2}}{dz} - J_{xijk}^{n+1/2} \right) \tag{2.24}$$

$$E_{yijk}^{n+1} = \frac{\frac{dt}{\varepsilon} - \frac{\sigma}{2}}{\frac{dt}{\varepsilon} + \frac{\sigma}{2}} E_{yijk}^{n} + \frac{1}{\frac{dt}{\varepsilon} + \frac{\sigma}{2}} \left(\frac{H_{xijk}^{n+1/2} - H_{xijk-1}^{n+1/2}}{dz} - \frac{H_{zijk}^{n+1/2} - H_{zi-1jk}^{n+1/2}}{dx} - J_{yijk}^{n+1/2} \right) \tag{2.25}$$

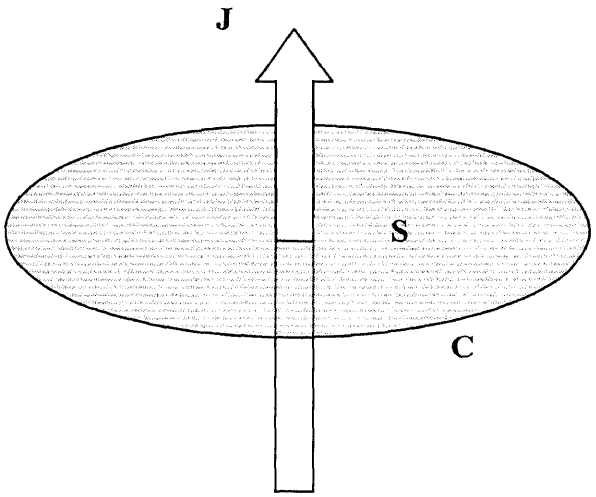

Figure 2.2 Illustration of Ampere's Law in which J may contain the lumped current

$$E_{zijk}^{n+1} = \frac{\frac{dt}{\varepsilon} - \frac{\sigma}{2}}{\frac{dt}{\varepsilon} + \frac{\sigma}{2}} E_{zijk}^{n} + \frac{1}{\frac{dt}{\varepsilon} + \frac{\sigma}{2}} \left(\frac{H_{yijk}^{n+1/2} - H_{yi-1jk}^{n+1/2}}{dx} - \frac{H_{xijk}^{n+1/2} - H_{xij-1k}^{n+1/2}}{dy} - J_{zijk}^{n+1/2} \right) \quad (2.26)$$

In which J is the lumped current term.

In the circuit theory, the current flowing through a component is a function of the voltage exerted on this component. Thus, the lumped current is the function of the voltage between the two points at which the lumped element is connected to an electromagnetic distributed system.

$$I_{lumped} = f(V_{lumped}) \quad (2.27)$$

Figure 2.3 shows a lumped element connected to an electromagnetic system between nodes A and B. Based on the definition of a lumped element, the physical dimension is much smaller than the wavelength. Hence, generally, we can put the lumped element along one FDTD grid edge, as shown in Figure 2.3.

The voltage is the integration of E field from A to B,

$$V_{lumped} = V_{AB} = \sum_{i=A}^{B} E_{xijk} dx \quad (2.28)$$

Once the E field is known between A and B points, the lumped voltage can be obtained. Then the lumped current value can be calculated based on the IV characteristic of the lumped element. Thus, the E field between nodes A and B in next time step is solved by the extended FDTD equations (2.24-26).

Notice that the lumped current term in (2.24-26) is defined at time n+1/2. In the procedure described above, the current value obtained is at time n. With the previous lumped current value substituted into the FDTD equations, the FDTD stability is

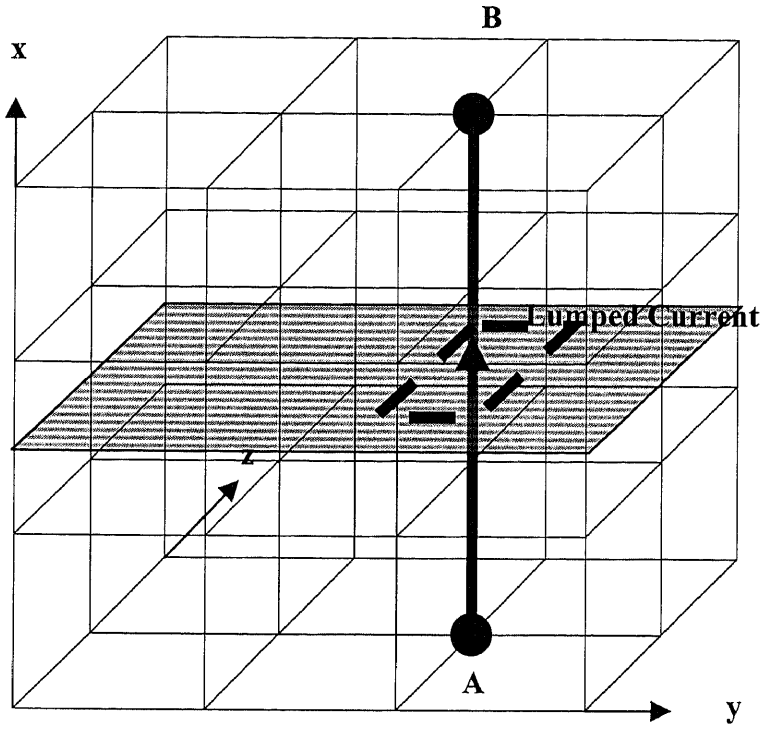

Figure 2.3 Illustration of Ampere's Law in which J may contain the lumped current in a FDTD grid

influenced negatively, and in case of a non-linear lumped element, the stability is even worse. Some approaches have been used to improve the stability.

One straightforward approach is to reduce the time increment. However, this approach does not work in case of an extreme non-linear lumped element involved. It increases the computational cost that is already a critical problem in FDTD. Some researchers modified it to be an adaptive time step approach. If the electromagnetic field changes very quickly, smaller time steps are used. Otherwise, the normal time step is used [Ciampolini 1996]. Because of the relative high computational cost, the adaptive time step approach is not widely used.

Another approach is to bring the current value at time n+1/2 directly into FDTD equations. (2.27) is written as following

$$I_{lumped} = f(V_{lumped}^{n+1} + V_{lumped}^{n}) \tag{2.29}$$

With this lumped current value substituted into FDTD equations, the unknowns, which are the E field values at time n+1, appear at both side of the equation. The FDTD equations between nodes A and B become an equation system. Generally, this equation system can be solved by such method as Newton-Raphson method. This would be very time consuming if (2.29) is a nonlinear equation. In order to avoid solving the equation system, which might be nonlinear, some researchers use a set of linear sections to replace the curve of (2.29). Hence in each section, only a linear equation system needs to be solved.

2.4. Absorbing Boundary Conditions (ABCs)

Lacking of a proper boundary condition used to be a main obstacle to spread FDTD to many applications during its early time. Presently, ABCs are used to truncate the FDTD computational domain, which might extend to infinity, to a limited range. On the boundary, the wave propagates only in outward direction. The ABCs absorb all the outgoing electromagnetic waves. The performance of ABCs is generally satisfactory. This section introduces the most two popular ABCs, i. e. Mur's ABCs and Berenger's PML.

2.4.1. Mur's ABCs

A second-order scalar wave equation for every EM field component can be deduced from Maxwell's equations. This wave equation describes the electromagnetic wave in all directions. Mur's ABCs are based on the defactoring the second-order wave equations into two first-order wave equations, and each of them represents the wave in opposite directions.

If E is one electromagnetic field component in an inhomogeneous and lossless media, it satisfies the wave equation

$$\frac{\partial^2 E}{\partial x^2}+\frac{\partial^2 E}{\partial y^2}+\frac{\partial^2 E}{\partial z^2}-\frac{\partial^2 E}{c^2\partial t^2}=0 \tag{2.30}$$

Define two pseudo operators Sy and Sz

$$Sy=\frac{\frac{\partial}{\partial y}}{\frac{\partial}{c\partial t}} \tag{2.31}$$

$$Sz = \frac{\frac{\partial}{\partial z}}{\frac{\partial}{c\partial t}} \tag{2.32}$$

(2.30) can be rewritten as

$$\frac{\partial^2 E}{\partial x^2} = (1 - Sy^2 - Sz^2)\frac{\partial^2 E}{c^2 \partial t^2} \tag{2.33}$$

(2.33) can be defactored as two equations which describe the wave propagates along +x and -x directions respectively. Suppose that we have a boundary at +x direction, the differential equation describing the outgoing wave is

$$\frac{\partial E}{\partial x} = (1 - Sy^2 - Sz^2)^{1/2}\frac{\partial E}{c\partial t} \tag{2.34}$$

(2.34) has a square root function of two pseudo operators that can be approximated by its Taylor's series. The different orders of the Taylor's series produce different order difference equations from (2.34).

First-order Taylor's series:

$$(1 - Sy^2 - Sz^2)^{1/2} = 1 \tag{2.35}$$

First-order Mur ABCs:

$$\frac{\partial E}{\partial x} = \frac{\partial E}{c\partial t} \tag{2.36}$$

Second-order Taylor's series:

$$(1 - Sy^2 - Sz^2)^{1/2} = 1 - \frac{1}{2}(Sy^2 + Sz^2) \tag{2.37}$$

Second-order Mur ABCs:

$$\frac{\partial^2 E}{c\partial x\partial t} + \frac{\partial^2 E}{2\partial y^2} + \frac{\partial^2 E}{2\partial z^2} - \frac{\partial^2 E}{c^2 \partial t^2} = 0 \tag{2.38}$$

The FDTD discretization forms of (2.36) and (2.38) can be found in [Mur 1988].

Equation (2.36) can only describe the wave that propagates perpendicularly to the x+ boundary. A certain amount of reflection will be caused to an obliquely outgoing wave. The reflection of an obliquely outgoing wave is significantly reduced by (2.37). The reflection of this boundary condition depends on the angle with which the electromagnetic wave propagates to the boundary. If the angle is too small, a strong reflection is generated by the boundary.

Although the Mur's boundary condition can be extended to higher order if higher Taylor's series is used, it does not help much on the reflection. On the other hand, it causes a stability problem. Normally, second-order Mur's ABCs are satisfactory in terms of both accuracy and stability.

Notice that the second-order Mur's ABCs cannot be used everywhere in a FDTD computational domain. In the corner, the only choice is the first-order boundary condition.

In order to obtain a better performance from Mur's ABCs, the boundary has to be kept a certain distance from the interested area in order to reduce the influence of the unexpected numerical reflection. Generally, Mur's ABCs can reach the reflection coefficient as low as - 20-30 dB.

2.4.2. Perfectly Matched Layer (PML)

The absorbing boundary can also be built up by wrapping the FDTD computational domain with a lossey medium. Berenger's PML is the most elegant absorbing medium used in the FDTD boundaries.

PML is developed by recognizing that a plane wave is perfectly matched when it is normally incident on a half space which has the following characteristic

$$\frac{\sigma}{\varepsilon}=\frac{\sigma^*}{\mu} \tag{2.39}$$

in which σ^* is the magnetic conductivity.

However, this medium fails to absorb the waves that are incident on it obliquely.

Berenger overcame this failure by artificially splitting each electromagnetic field component into two sub-components. He also defined the corresponding independent magnetic or electric conductivity to each sub-component.

Take the two-dimensional TE mode as an example, the modified Maxwell's equations for PML is

$$\varepsilon\frac{\partial E_x}{\partial t}+\sigma_y E_x=\frac{\partial H_z}{\partial y} \tag{2.40}$$

$$\varepsilon\frac{\partial E_y}{\partial t}+\sigma_x E_y=-\frac{\partial H_z}{\partial x} \tag{2.41}$$

$$\mu\frac{\partial H_{zx}}{\partial t}+\sigma_x^* H_{zx}=-\frac{\partial E_y}{\partial x} \tag{2.42}$$

$$\mu\frac{\partial H_{zy}}{\partial t}+\sigma_y^* H_{zy}=\frac{\partial E_x}{\partial y} \tag{2.43}$$

in which $H_z=H_{zx}+H_{zy}$ and σ^*_x and σ^*_y are the magnetic conductivity for Hzx and Hzy respectively.

This scheme lets the electromagnetic wave, normally or obliquely, propagates through the interface of free space and the PML medium without any reflection under proper-designed parameters. For example, the reflection coefficient is zero in the boundary of +x if the parameters of the PML medium holds the following relations

$$\sigma_y=\sigma^*_y=0 \text{ and } \frac{\sigma_x}{\varepsilon}=\frac{\sigma_x^*}{\mu} \tag{2.44}$$

In addition, in this case the time-harmonic solution in the PML region is

$$Hz = H_0 e^{j\omega t} e^{-j\frac{\omega}{c}(x\cos\phi+y\sin\phi)} e^{-x\frac{\sigma_x\cos\phi}{\varepsilon c}} \tag{2.45}$$

(2.44) shows an exponentially decreased electromagnetic wave propagating inside the PML media. Suppose that at the most outside, there is a perfect electric conductor (PEC) wall wrapping the PML medium. The electromagnetic wave then propagates through the PML medium, then reaches the PEC wall, and finally is bounced back to the FDTD computational region. After the wave propagates back and forth in the PML medium, its amplitude is dramatically reduced to a very small value which can reach the accuracy requirement.

Berenger first derived the PML in two dimensions [Berenger 1994] and this method was extended to three-dimensional FDTD method soon after that [Katz et al 1994]. The three dimensional PML equations are

$$\varepsilon\frac{\partial E_{xy}}{\partial t}+\sigma_y E_{xy}=\frac{\partial H_z}{\partial y} \tag{2.46}$$

$$\varepsilon\frac{\partial E_{xz}}{\partial t}+\sigma_z E_{xz}=-\frac{\partial H_y}{\partial z} \tag{2.46}$$

$$\mu\frac{\partial H_{xy}}{\partial t}+\sigma_y^* H_{xy}=-\frac{\partial E_z}{\partial y} \tag{2.47}$$

$$\mu\frac{\partial H_{xz}}{\partial t}+\sigma_z^* H_{xz}=\frac{\partial E_y}{\partial z} \tag{2.48}$$

$$\varepsilon\frac{\partial E_{yx}}{\partial t}+\sigma_x E_{yx}=-\frac{\partial H_z}{\partial x} \tag{2.49}$$

$$\varepsilon \frac{\partial E_{yz}}{\partial t} + \sigma_z E_{yz} = \frac{\partial H_x}{\partial z} \tag{2.50}$$

$$\mu \frac{\partial H_{yx}}{\partial t} + \sigma_x^* H_{yx} = \frac{\partial E_z}{\partial x} \tag{2.51}$$

$$\mu \frac{\partial H_{yz}}{\partial t} + \sigma_z^* H_{yz} = -\frac{\partial E_x}{\partial z} \tag{2.52}$$

$$\mu \frac{\partial E_{zx}}{\partial t} + \sigma_x E_{zx} = \frac{\partial H_y}{\partial x} \tag{2.53}$$

$$\mu \frac{\partial E_{zy}}{\partial t} + \sigma_y E_{zy} = -\frac{\partial H_x}{\partial y} \tag{2.54}$$

$$\mu \frac{\partial H_{zx}}{\partial t} + \sigma_x^* H_{zx} = -\frac{\partial E_y}{\partial x} \tag{2.55}$$

$$\mu \frac{\partial H_{zy}}{\partial t} + \sigma_y^* H_{zy} = \frac{\partial E_x}{\partial y} \tag{2.56}$$

in which every electromagnetic field component is split into two sub-components and their corresponding electric and magnetic conductivity is defined.

Because the electromagnetic field changes rapidly in a PML medium, some researchers suggested using the exponential discretization scheme to discretize the time derivative [Berenger 1994] in order to improve the stability of the PML equations. Others people think that such scheme will not help too much to the stability [Veihl and Mittra 1996]. The reason is that the electromagnetic field changes rapidly in space but not in time. Therefore, the exponential scheme in time does not improve the stability. Thus, the central discretization scheme to discretize the time derivative is also be used. The discretization of PML equations is straightforward under this scheme, just like the normal FDTD leapfrog scheme.

The electric and magnetic conductivity profile in a PML layer is another important factor to influence the performance of the PML. Constant, linear, parabolic, and geometric profiles are all used to define the conductivity profile from the interface between PML and Yee cell to the outer boundary, normally PEC wall. The parabolic profile is much better than the linear and constant profile, but for the simulation with a large number of iterations, the parabolic profile causes a significant error. The geometric profile can avoid this problem, but a more careful design has to be made to the PML boundary layers [Berenger 1996].

Generally, the performance of the PML is much better than Mur's ABCs. According to [Berenger 1994], the reflection coefficient of PML is 20 dB less than that of Mur's ABCs. The payoff of this excellent performance is its higher computational cost because of the splitting of the electromagnetic field components and additional layers in the FDTD grid.

In the microwave and high frequency circuit analysis, involving complicated electromagnetic phenomena, such as near field phenomena and high order modes, PML is generally accepted as the main approach to handle boundary conditions in FDTD simulation.

2.5. Conclusion

In this chapter, some fundamental FDTD issues are briefly reviewed. All the discussed topics are essentially related to the purpose of this dissertation, modeling and analysis of hybrid systems. In addition, in each topic, the present research progresses are demonstrated. With these progresses, FDTD methods obtained many applications in the area of wave propagation, microwave devices analysis, optical, et al (see the FDTD data

base mentioned in Chapter 1 for your interested topic). Based on the existing achievements, the FDTD method demonstrates its potential to become a powerful analysis tools for the practical hybrid system analysis.

CHAPTER 3

NUMERICAL ERROR OF FDTD METHODS

3.1. Introduction

In a homogeneous medium discretized by a uniform FDTD grid, there exist numerical errors depending on the relation between the cell size and the wavelength of the electromagnetic wave. The relation is known as the FDTD numerical dispersion relation. In a practical system, inhomogeneous media are usually used and numerical errors in these media must be considered. Specifically, the FDTD numerical wave behaviors in the interface of two media are interesting and worthy of explores. The investigation of this problem will help us improve the FDTD simulation accuracy.

In order to describe accurately the complicated geometry shape of an electromagnetic system, the non-uniform grid has to be introduced into the FDTD analysis. The non-uniform FDTD grid provides us flexibility to improve the accuracy. Knowledge about the numerical errors in an inhomogeneous medium discretized by non-uniform FDTD grids will give us a significant help to construct the simulation model intelligently.

This chapter analyzes the characteristics of a plane wave on the boundary of two adjacent media discretized by non-uniform FDTD rectangular grids. The reflection and refraction characteristics of the wave propagation at the boundary of two adjacent media due to the numerical dispersion of FDTD method are demonstrated. In the FDTD simulation, these characteristics are different from the theoretical solution and cause numerical error. The magnitude of numerical errors depends on the FDTD discretization

parameters. Knowing these characteristics would help us manipulate the FDTD cell size distribution in order to achieve the desired simulation accuracy within the requirement.

3.2. Non-Uniform FDTD Grid

In Chapter 2, the FDTD equations are derived from the differential Maxwell's equations in a homogeneous medium filled by uniform FDTD grids. In an inhomogeneous medium discretized by non-uniform FDTD grids, the integral forms of Maxwell's equations are more convenient to derive the FDTD equations. In this and the following chapters, we will see that the integral form has clearer physical meaning than the differential form and it can handle the boundary condition between two adjacent media automatically.

Let's take Ez as an example to derive the FDTD equation in an inhomogeneous medium discretized by non-uniform grids. Figure 1 shows the FDTD grid around node (ijk). Ampere's Law for Ez holds

$$\iint_S (\varepsilon \frac{\partial E_z}{\partial t} + \sigma E_z) ds = \oint_C \boldsymbol{H} \bullet \cdot \boldsymbol{dl} \tag{3.1}$$

Assume that E_z is uniform in area S and H is uniform along one edge of the contour C. The discretization form of (3.1) can be derived as

$$E_{zijk}^{n+1} = \frac{E_{zijk}^{n+1} \sum_{p=i-1}^{i} \sum_{q=j-1}^{j} [(\frac{\varepsilon_{pqk}}{dt} - \frac{\sigma_{pq}}{2}) \frac{dx_p dy_q}{4}] + \left(H_{yijk}^{n+\frac{1}{2}} - H_{yi-1jk}^{n+\frac{1}{2}} \right) \frac{dy_j + dy_{j-1}}{2} - \left(H_{xijk}^{n+\frac{1}{2}} - H_{xij-1k}^{n+\frac{1}{2}} \right) \frac{dx_i + dx_{i-1}}{2}}{\sum_{p=i-1}^{i} \sum_{q=j-1}^{j} \left[\left(\frac{\varepsilon_{pqk}}{dt} + \frac{\sigma_{pq}}{2} \right) \frac{dx_p dy_q}{4} \right]} \tag{3.2}$$

Instead of taking special consideration to the boundary condition on the interface of different media, (3.2) handles the boundary with the same form as that in a homogeneous media. This simplifies the implementation of an FDTD method. Also, the non-uniform

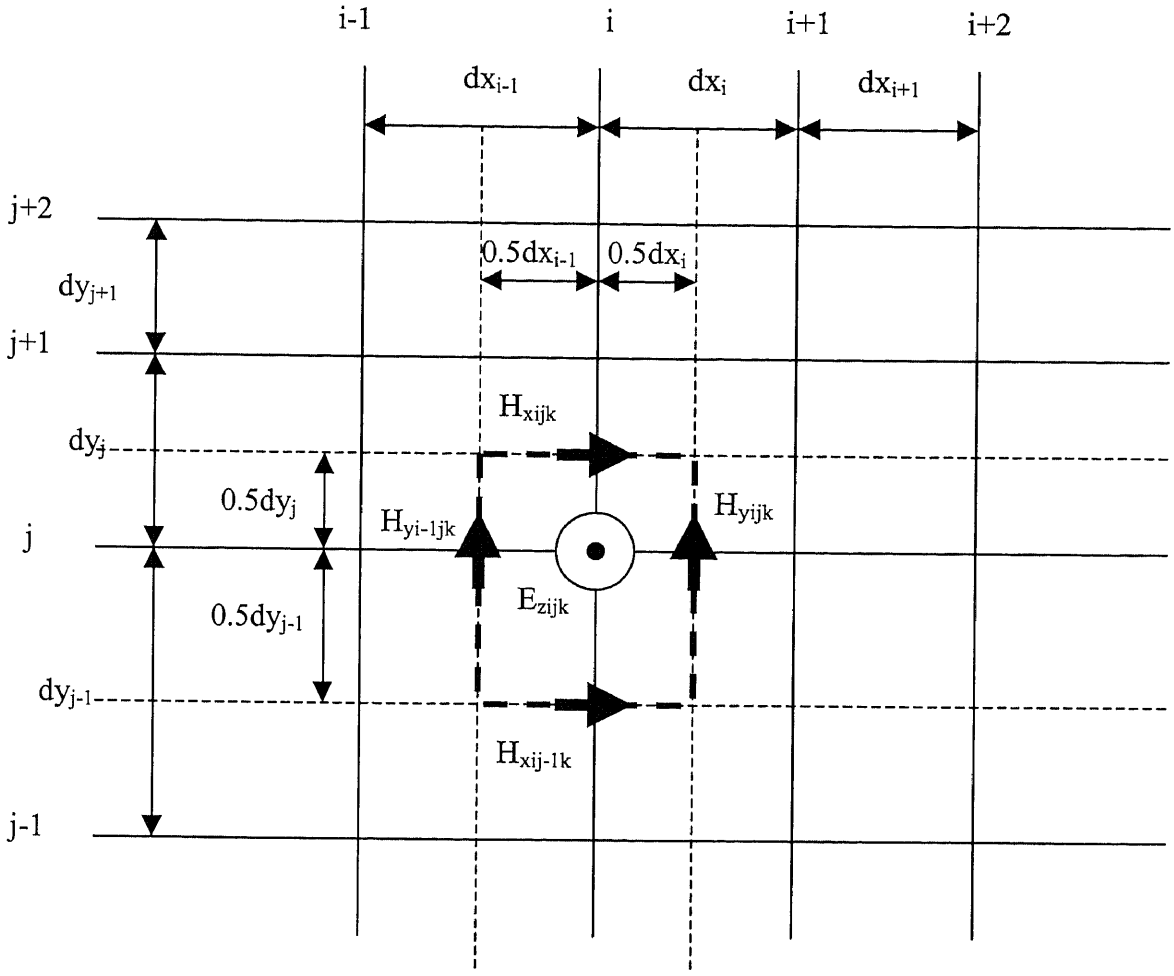

Figure 3.1 Non-uniform FDTD grid and illustration of an integral form for the FDTD equation of Ez.

grid configuration can also be included directly into (3.2). In the rest of the dissertation, the integral Maxwell's equations are generally utilized to derive the FDTD equation for different purposes.

Similar to the derivation of an FDTD equation for Ez component, the other FDTD equations for the non-uniform grid can be derived and listed bellow as a reference.

$$E_{xijk}^{n+1} = \frac{E_{xijk}^{n+1} \sum_{p=j-1}^{j} \sum_{q=k-1}^{k} [(\frac{\varepsilon_{ipq}}{dt} - \frac{\sigma_{pq}}{2}) \frac{dy_p dz_q}{4}] + \left(H_{zijk}^{n+\frac{1}{2}} - H_{zij-1k}^{n+\frac{1}{2}} \right) \frac{dz_k + dz_{k-1}}{2} - \left(H_{yijk}^{n+\frac{1}{2}} - H_{yijk-1}^{n+\frac{1}{2}} \right) \frac{dy_j + dy_{j-1}}{2}}{\sum_{p=j-1}^{j} \sum_{q=k-1}^{k} \left[\left(\frac{\varepsilon_{ipq}}{dt} + \frac{\sigma_{pq}}{2} \right) \frac{dy_p dz_q}{4} \right]} \tag{3.3}$$

$$E_{yijk}^{n+1} = \frac{E_{yijk}^{n+1} \sum_{p=i-1}^{i} \sum_{q=k-1}^{k} [(\frac{\varepsilon_{pjq}}{dt} - \frac{\sigma_{pq}}{2}) \frac{dx_p dz_q}{4}] + \left(H_{xijk}^{n+\frac{1}{2}} - H_{yijk-1}^{n+\frac{1}{2}} \right) \frac{dx_i + dx_{i-1}}{2} - \left(H_{zijk}^{n+\frac{1}{2}} - H_{zi-1jk}^{n+\frac{1}{2}} \right) \frac{dz_k + dz_{k-1}}{2}}{\sum_{p=i-1}^{i} \sum_{q=k-1}^{k} \left[\left(\frac{\varepsilon_{pjq}}{dt} + \frac{\sigma_{pq}}{2} \right) \frac{dx_p dz_q}{4} \right]} \tag{3.4}$$

$$H_{xijk}^{n+1/2} = H_{xijk}^{n-1/2} + \frac{\left(E_{yijk+1}^{n} - E_{yijk}^{n} \right) \frac{dy_j + dy_{j+1}}{2} - \left(E_{zij+1k}^{n} - E_{zijk}^{n} \right) \frac{dz_k + dz_{k+1}}{2}}{\sum_{p=j-1}^{j} \sum_{q=k-1}^{k} [\frac{\mu_{ipq}}{dt} \frac{dy_p dz_q}{4}]} \tag{3.5}$$

$$H_{yijk}^{n+1/2} = H_{yijk}^{n+1/2} + \frac{\left(E_{zi+1jk}^{n} - E_{zijk}^{n} \right) \frac{dz_k + dz_{k+1}}{2} - \left(E_{xijk+1}^{n} - E_{xijk}^{n} \right) \frac{dx_i + dx_{i+1}}{2}}{\sum_{p=i-1}^{i} \sum_{q=k-1}^{k} [\frac{\mu_{pq}}{dt} \frac{dx_p dz_q}{4}]} \tag{3.6}$$

$$H_{zijk}^{n+1/2} = H_{zijk}^{n+1/2} + \frac{\left(E_{xij+1k}^{n} - E_{xijk}^{n} \right) \frac{dx_i + dx_{i+1}}{2} - \left(E_{yi+1jk}^{n} - E_{yijk}^{n} \right) \frac{dy_j + dy_{j+1}}{2}}{\sum_{p=i-1}^{i} \sum_{q=j-1}^{j} [\frac{\mu_{pq}}{dt} \frac{dx_p dy_q}{4}]} \tag{3.7}$$

3.3. Plane Wave on the Boundary of Two Adjacent Media

A wave propagating in an inhomogeneous medium generates very complicated patterns and is always an interesting problem in the electromagnetic area. In order to simplify this problem, the inhomogeneous media in our discussion consist of two dielectric media and each of them occupies a half space of the computational domain.

In classical electromagnetic theory, the reflection on the interface of two media is well known. In an FDTD method, because the numerical dispersion relation is different from the theoretical solution, the reflecting and transmitting behaviors are quite different. For this simplified structure, one and two-dimensional analyses will cover all the wave behaviors on the boundary.

3.3.1. One Dimensional FDTD

Assume that an electromagnetic field modeled by a 1D FDTD modeling space has E_x and H_z components. The FDTD modeling space is filled with a homogeneous material of ε and μ. The FDTD cell size is d. Hence, a plane monochromatic traveling wave trivial solution is

$$E_x = E_{x0} e^{j(\omega n dt - kjd)} \tag{3.8}$$

$$H_z = H_{z0} e^{j(\omega n dt - kjd)} \tag{3.9}$$

where k is the numerical wave number. Substituting (3.8) and (3.9) into the FDTD finite difference equation, one has the relation of the amplitude of E and H

$$E_{x0} \frac{\varepsilon}{dt} \sin(\frac{\omega dt}{2}) = H_{z0} \frac{1}{d} \sin(\frac{kd}{2}) \tag{3.10}$$

$$H_{z0} \frac{\mu}{dt} \sin(\frac{\omega dt}{2}) = E_{x0} \frac{1}{d} \sin(\frac{kd}{2}) \tag{3.11}$$

The dispersion relation of one dimension FDTD wave can be obtained from (3.10) and (3.11)

$$\frac{\sqrt{\mu\varepsilon}}{dt}\sin(\frac{\omega dt}{2}) = \frac{1}{d}\sin(\frac{kd}{2}) \tag{3.12}$$

One can also obtain the numerical characteristic impedance

$$\xi = \frac{E_{x0}}{H_{z0}} = \sqrt{\frac{\mu}{\varepsilon}} \tag{3.13}$$

(3.13) shows that the FDTD numerical characteristic impedance is equal to the theoretical one.

Based on the above relations, we can derive the FDTD numerical reflection coefficient on the boundary between two linear media. Without losing generality, assume that a plane wave propagates normally from Region 1 to Region 2 in y direction, as shown in Figure 3.2(a). On the boundary between these two regions, due to the discontinuity of the media, an incident wave generates a reflecting wave and a transmitting wave. The electromagnetic waves in the two regions can be represented by

Region 1: the incident wave and reflecting wave

$$E_{x1} = A(e^{j(\omega ndt - k_1 jd_1)} + R \cdot e^{j(\omega ndt + k_1 jd_1)}) \tag{3.14}$$

$$H_{z1} = \xi_1^{-1} A(e^{j(\omega ndt - k_1 jd_1)} - R \cdot e^{j(\omega ndt + k_1 jd_1)}) \tag{3.15}$$

Region 2: the transmitting wave

$$E_{x2} = Be^{j(\omega ndt - k_2 jd_2)} \tag{3.16}$$

$$H_{z2} = \xi_2^{-1} Be^{j(\omega ndt - k_2 jd_2)} \tag{3.17}$$

in which R is the numerical reflection coefficient, ξ_1 and ξ_2 are the characteristic impedance in Region 1 and Region 2, respectively.

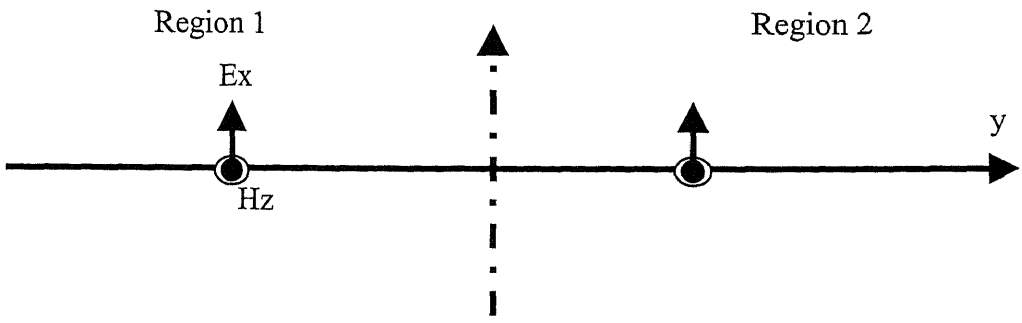

(a) one-dimensional case

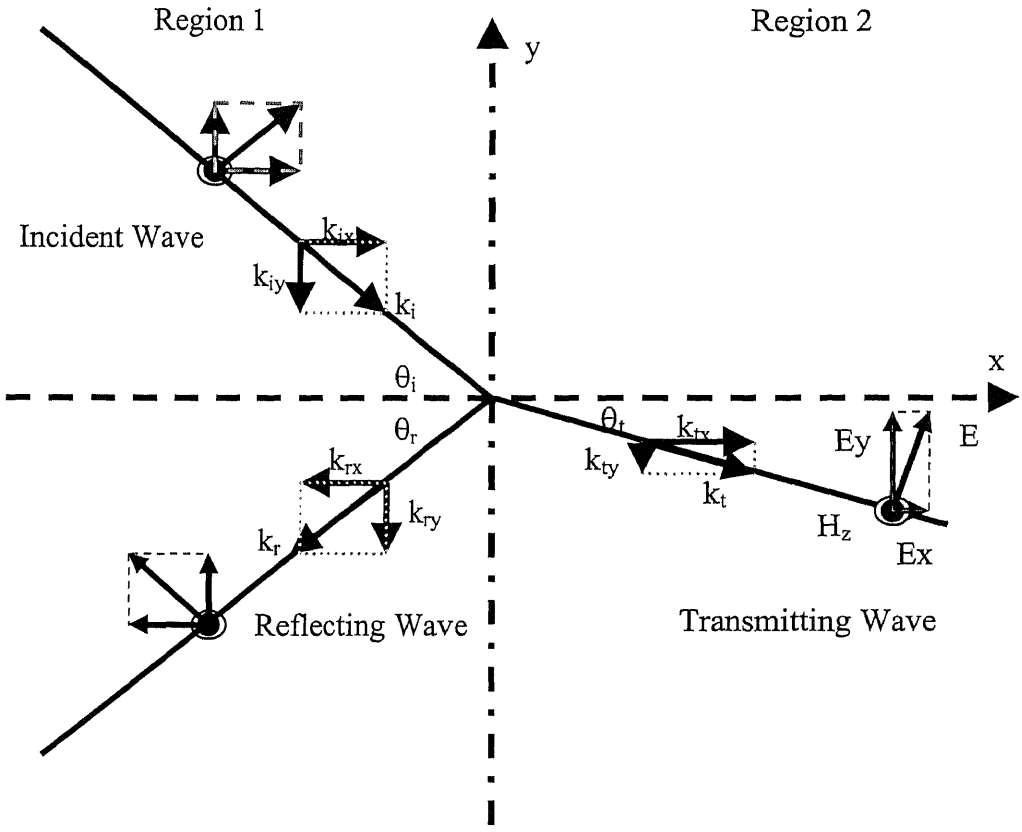

(b) two-dimensional case

Figure 3.2 Parallel-polarization wave in the interface of two different media

Without losing generality, assume that j=0 on the boundary. Because the tangential component of the electrical field on the boundary is continuous, by (3.14) and (3.16), we can obtain

$$A(1+R)=B \tag{3.18}$$

With the reference of (3.3), which is a 3D FDTD equation, the one-dimensional FDTD equation of Ex on the boundary is

$$\frac{(E_{xj}^{n+1}-E_{xj}^{n})}{dt}\cdot\frac{\varepsilon_1 d_1+\varepsilon_2 d_2}{2}=H_{zj-1/2}^{n+1/2}-H_{zj+1/2}^{n+1/2} \tag{3.19}$$

Substituting (3.14) ~ (3.17) into (3.19), with the help of relation (3.18), after several steps of algebra, one can obtain the numerical reflection coefficient R

$$R=\frac{j\dfrac{(\varepsilon_1 d_1+\varepsilon_2 d_2)\sin(\dfrac{\omega dt}{2})}{\delta t}+\xi_2^{-1}e^{-j\phi_2}-\xi_1^{-1}e^{j\phi_1}}{j\dfrac{(\varepsilon_1 d_1+\varepsilon_2 d_2)\sin(\dfrac{\omega dt}{2})}{dt}+\xi_2^{-1}e^{-j\phi_2}+\xi_1^{-1}e^{j\phi_1}} \tag{3.20}$$

where $\phi_t=\frac{\omega dt}{2}$, $\phi_1=\frac{k_1 d_1}{2}$, and $\phi_2=\frac{k_2 d_2}{2}$

A trivial test can be easily performed to the expression (3.20). Suppose that the media and FDTD grids are identical at two sides of the interface, in other words, there is no interface. Intuitively, R should be 0. With the help of the dispersion relation (3.12), the reflection coefficient R obtained from (3.20) is actually 0.

In case of the same media, but with the different FDTD cell sizes, there is a reflection caused only by the FDTD simulation, although theoretically it is impossible to have a reflection in a homogeneous medium. From this point, we can realize that the FDTD grid parameters may have important influence on the numerical wave behavior.

3.3.2. Oblique Incidence with Parallel Polarization

Instead of propagating along the grid in one-dimensional FDTD method, the electromagnetic wave propagates obliquely in the two-dimensional FDTD computational domain. Similar to the above derivation, first, we have to introduce the numerical dispersion relation of a plane wave in an FDTD modeling space with homogeneous media and uniform FDTD cell sizes.

A TE mode electromagnetic wave with components of Ex, Ey and Hz propagates in the x-y plane. $\widetilde{k}_x$ and $\widetilde{k}_y$ are its wave numbers in x and y direction, respectively. FDTD cell size is dx by dy and temporal increment is dt. Hence, a plane monochromatic traveling-wave solution is

$$E_x = E_{x0} e^{j(\omega ndt - (k_x id_x + k_y jd_y))} \tag{3.21}$$

$$E_y = E_{y0} e^{j(\omega ndt - (k_x id_x + k_y jd_y))} \tag{3.22}$$

$$H_z = H_{z0} e^{j(\omega ndt - (k_x i\delta_x + k_y jd_y))} \tag{3.23}$$

Substituting (3.21), (3.22) and (3.23) into 2D FDTD finite difference equations which can be obtained from (3.2) ~(3.7), one can obtain the following relations

$$\frac{-\mu}{dt}\sin(\frac{\omega dt}{2})H_{z0} = \frac{1}{d_y}\sin(\frac{k_y d_y}{2})E_{x0} - \frac{1}{d_x}\sin(\frac{k_x d_x}{2})E_{y0} \tag{3.24}$$

$$\frac{\varepsilon}{dt}\sin(\frac{\omega dt}{2})E_{y0} = \frac{1}{d_x}\sin(\frac{k_x d_x}{2})H_{z0} \tag{3.25}$$

$$\frac{\varepsilon}{dt}\sin(\frac{\omega dt}{2})E_{x0} = \frac{1}{d_y}\sin(\frac{k_y d_y}{2})H_{z0} \tag{3.26}$$

From (3.24), (3.25) and (3.26), the dispersion relation can be obtained as follows

$$\frac{\mu\varepsilon}{dt^2}\sin^2(\frac{\omega\delta t}{2}) = \frac{1}{d_y^{\ 2}}\sin^2(\frac{k_y d_y}{2}) + \frac{1}{d_x^{\ 2}}\sin^2(\frac{k_x d_x}{2}) \tag{3.27}$$

Also, the numerical characteristic impedance is

$$\xi = \frac{\sqrt{E_{x0}^2 + E_{y0}^2}}{H_{z0}} = \sqrt{\frac{\mu}{\varepsilon}} \tag{3.28}$$

Thus in two-dimensional FDTD method, the numerical characteristic is still equal to the theoretical one.

Now, we derive the reflection coefficient on the boundary of two adjacent media. Shown in Figure 3.2(b), a plane wave in parallel polarization propagates from Region 1 to Region 2. These two regions are filled with different media and have different FDTD discretization parameters. The trivial solutions of electromagnetic wave in Region 1 and 2 are:

Region 1: incident wave and reflecting wave.

$$H_{z1} = A(e^{j(\omega ndt-(k_{xi}id_{x1}+k_{yi}jd_{y1})} + R\cdot e^{j(\omega ndt-(k_{xr}id_{x1}+k_{yr}jd_{y1}))}) \tag{3.29}$$

$$E_{x1} = \xi_1 A(\sin\theta_i e^{j(\omega ndt-(k_{xi}id_{x1}+k_{yi}jd_{y1}))} + R\cdot\sin\theta_r e^{j(\omega ndt-(k_{xr}id_{x1}+k_{yr}jd_{y1}))}) \tag{3.30}$$

$$E_{y1} = \xi_1 A(\cos\theta_i e^{j(\omega ndt-(k_{xi}id_{x1}+k_{yi}jd_{y1}))} - R\cdot\cos\theta_r e^{j(\omega ndt-(k_{xr}id_{x1}+k_{yr}jd_{y1}))}) \tag{3.31}$$

Region 2: transmitting wave.

$$H_{z2} = Be^{j(\omega ndt-(k_{xt}id_{x2}+k_{yt}jd_{y2})} \tag{3.32}$$

$$E_{x1} = \xi_2 B\sin\theta_t e^{j(\omega ndt-(k_{xt}id_{x2}+k_{yt}jd_{y2}))} \tag{3.33}$$

$$E_{y1} = \xi_2 B\cos\theta_t e^{j(\omega ndt-(k_{xt}id_{x2}+k_{yt}jd_{y2}))} \tag{3.34}$$

in which θi, θt, and θr are the incident angle, transmitting angle, and the reflecting angle, respectively.

Without losing generality, assume that i=0 on the boundary and dy1=dy2. On the boundary, the tangential component, which is Ey in this case, is continuous. Hence, from (3.31) and (3.34), we can obtain

$$k_{yi} = k_{yr} = k_{yt} \tag{3.35}$$

$$\xi_1 \cos\theta_i (1-R)A = \xi_2 \cos\theta_t B \tag{3.36}$$

From (3.35) and the dispersion relation in Medium 1, we can derive that the reflecting angle is equal to the incident angle,

$$\theta_r = \theta_i . \tag{3.37}$$

This relation is the same as the theoretical results. This means that the FDTD method does not influence the relation of reflection angle and incident angle. This result is intuitive because that the reflecting wave and incident wave are in the same media.

The relation of transmission angle and incident angle can be obtained from (3.35) and the dispersion relations in the two media. It does not have an explicit form but we can solve it numerically. The transmission angle is different from what obtained theoretically, i.e. by Snell's Law. The difference between the theoretical and FDTD transmission angles depends on the FDTD cell size and incident angle. It will be shown in the next section how the FDTD method influences the wave property via its grid parameters.

Next let us derive the reflection coefficient R.

The two-dimensional FDTD equation of Ey can be obtained from (3.4) by considering only the Ex, Ey and Hz components

$$\frac{(E^{n+1}_{yij+1/2} - E^{n}_{yij+1/2})}{dt} \bullet \frac{\varepsilon d_{x1} + \varepsilon d_{x2}}{2} = H^{n+1/2}_{zi-1/2\,j+1/2} - H^{n+1/2}_{zi+1/2\,j+1/2} \tag{3.38}$$

Substituting (3.29)~(3.34) into (3.38), with the help of (3.35) ~(3.37), we can obtain the numerical reflection coefficient R as follows

$$R = \frac{j\frac{(\varepsilon_1 d_{x1} + \varepsilon_2 d_{x2})\sin(\frac{\omega dt}{2})}{dt} + \frac{e^{-j\phi_2}}{\xi_2 \cos\theta_t} - \frac{e^{j\phi_1}}{\xi_1 \cos\theta_i}}{j\frac{(\varepsilon_1 d_{x1} + \varepsilon_2 d_{x2})\sin(\frac{\omega dt}{2})}{dt} + \frac{e^{-j\phi_2}}{\xi_2 \cos\theta_t} + \frac{e^{j\phi_1}}{\xi_1 \cos\theta_i}} \tag{3.39}$$

where $\phi_t = \frac{\omega dt}{2}$, $\phi_1 = \frac{k_{xi} d_{x11}}{2}$, and $\phi_2 = \frac{k_{xi} d_{x2}}{2}$

In case of a normal incident wave, it is easy to show that incident and transmitting angles are zero, and (3.39) has exactly the same expression as (3.20). This has to be satisfied if we obtain a correct expression of R.

3.3.3. Oblique Incidence with Perpendicular Polarization

Theoretically, Snell's Law is correct for EM waves in both parallel and perpendicular polarizations. In FDTD, this relation between transmitting angle and incident angle is also the identical in these two cases.

By the similar derivation, the FDTD reflection coefficient of an EM wave in perpendicular polarization can be obtained as follows

$$R = \frac{j\frac{(\varepsilon_1 d_{x1} + \varepsilon_2 d_{x2})\sin(\frac{\omega dt}{2})}{dt} + \frac{\xi_2 e^{-j\phi_2}}{\cos\theta_t} - \frac{\xi_1 e^{j\phi_1}}{\cos\theta_i}}{j\frac{(\varepsilon_1 d_{x1} + \varepsilon_2 d_{x2})\sin(\frac{\omega dt}{2})}{dt} + \frac{\xi_2 e^{-j\phi_2}}{\cos\theta_t} + \frac{\xi_1 e^{j\phi_1}}{\cos\theta_i}} \tag{3.40}$$

where $\phi_t = \frac{\omega dt}{2}$, $\phi_1 = \frac{k_{xi} d_{x1}}{2}$, and $\phi_2 = \frac{k_{xi} d_{x2}}{2}$

3.4. Discussion

3.4.1. Normally Incident Wave

The basic operating mode of many transmission lines is the TEM mode. If the TEM mode is dominant in a system, the normally incident wave is potentially the main source of the numerical error. The one dimensional FDTD reflection coefficient can be used to show the numerical error corresponding to the FDTD cell size and media parameters in case of normally incident wave.

In Chapter II, we know that in order to reduce the FDTD dispersion error, the cell size has to be chosen according to the wavelength in the medium. The wavelength is related to the wave speed that is a characteristic parameter of this medium. This motivates a consideration that the cell sizes have to be related to the wave speeds in the two media to improve the FDTD performance. Intuitively, we consider a special situation

$$\frac{d_1}{c_1} = \frac{d_2}{c_2} \tag{3.41}$$

Substituting (3.41) into (3.20), with the help of (3.12) and (3.13), simplifies (3.20)

$$R = \frac{\xi_1 - \xi_2}{\xi_1 + \xi_2} \tag{3.42}$$

(3.42) is the same as the theoretical reflection coefficient of a wave normally incident on an interface between two media. This means, under condition (3.41), an FDTD method will not generate any numerical reflection. This can be also called magic cell size for the numerical reflection, just like the magic time step for the numerical dispersion mentioned in Chapter 2.

In many cases, because of some other consideration, such as the computational cost, we want to choose the cell size different from the magic cell size. (3.41) can help us to

estimate the numerical error cause by the FDTD method. Figure 3.3 and Figure 3.4 show the numerical reflections in some situations.

In Figure 3.3, the grid is fine in Region 1, $\lambda_1=20dx_1$. Given different media in Region 2, the numerical reflection is very close to the theoretical one when the two media's permittivities are close. The numerical reflection increases when $\varepsilon_2/\varepsilon_1$ increases. Also, we notice that the numerical error increases much faster in the big dx_2 region than that in the small dx_2 region. This means if dx_2 is beyond a limitation, the FDTD solution diverges immediately from the theoretical solution.

Figure 3.4 shows a similar behavior in a relatively coarse FDTD mesh. The numerical errors become larger. From Figure 3.4, we can see, if we have enough computational resource, we can use a smaller cell size. However, we can try to optimize our FDTD grid to choose the cell size near the cross of the theoretical solution and the FDTD solution.

3.4.2. Obliquely Incident Wave

The general case is an electromagnetic wave incidents the interface with an angle. We consider this situation in 2D FDTD method. As mentioned before, in an FDTD method, the reflecting angle is equal to the incident angle but the relation of the transmitting angle and incident angle does not obey the Snell's Law.

Suppose that the incident angle is θ_i, and wave number is k. In Region 1, shown in Figure 3.2, we have

$$k_{ix} = k_i \cos(\theta_i),\ k_{iy} = k_i \sin(\theta_i) \tag{3.43}$$

Substitute (3.43) into the dispersion relation in (3.28) in Region 1, we have

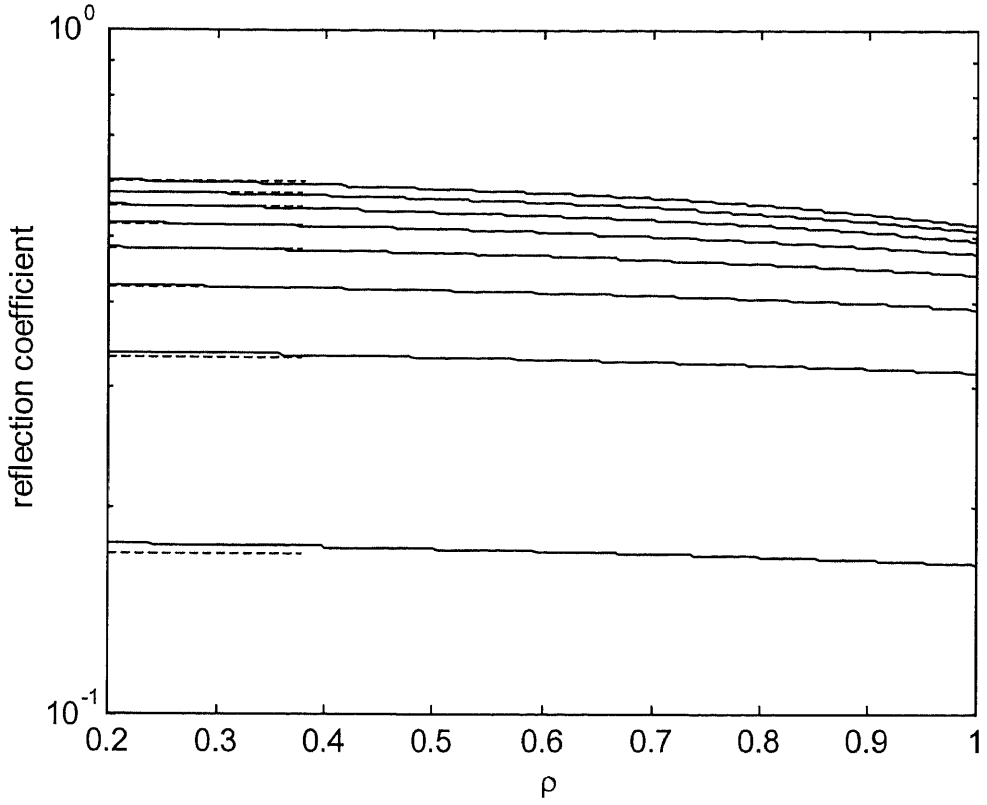

Figure 3.3 One–dimensional FDTD reflection coefficient, f=1GHz, $d_1=\lambda_1/20$, $\varepsilon_1=1$. Starting from the lowest pair of lines, $\varepsilon_2=2, 4, 6, \ldots, 16$. In each pair of curves, the theoretical solution is the dashed line parallel to ρ axis and the FDTD solution is the solid line. $\rho=d_2/d_1$

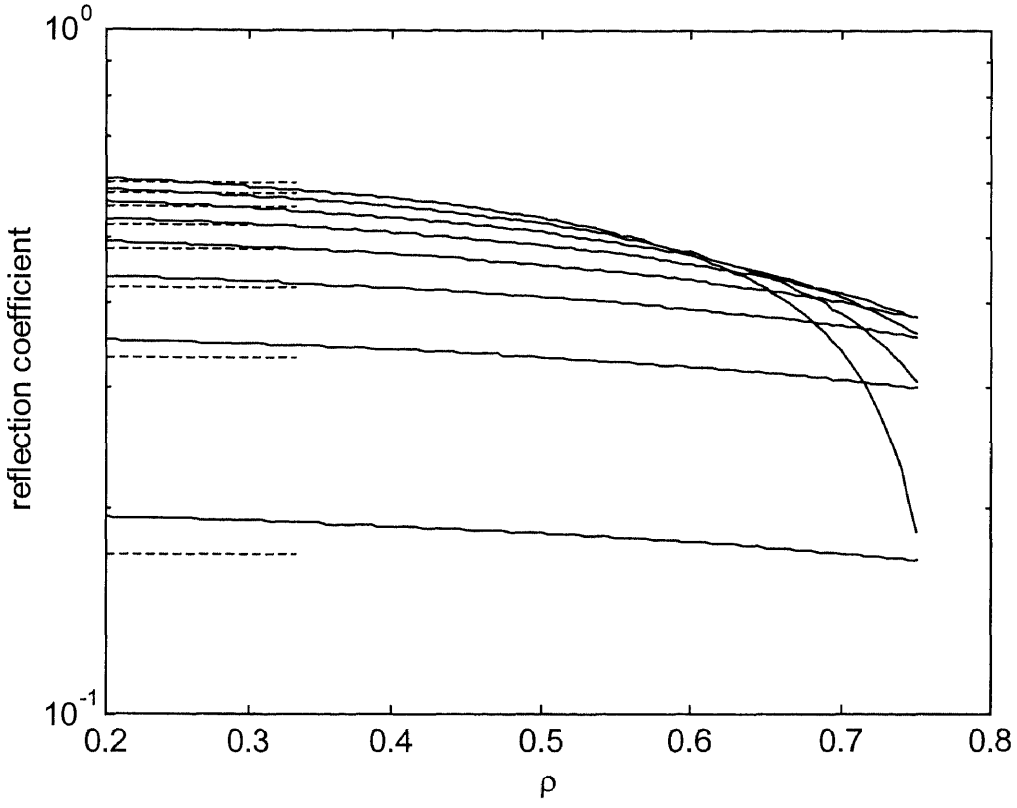

Figure 3.4 One–dimensional FDTD reflection coefficient, f=1GHz, $dx=\lambda_1/10$, $\varepsilon_1=1$. Starting from the lowest pair of lines, $\varepsilon_2=2, 4, 6, \ldots, 16$. In each pair of curves, the theoretical solution is the dashed line parallel to ρ axis and the FDTD solution is the solid line. $\rho=d_2/d_1$

$$\frac{\mu\varepsilon}{dt^2}\sin^2(\frac{\omega dt}{2}) = \frac{1}{d_y^{\ 2}}\sin^2(\frac{k_1\sin(\theta_i)d_y}{2}) + \frac{1}{d_{x1}^{\ 2}}\sin^2(\frac{k_1\cos(\theta_i)d_{x1}}{2}) \quad (3.44)$$

The wave number in Region 1 can be obtained from (3.44). Because of the relation

$$k_{yi} = k_{yr} = k_{yt} = k_i\sin(\theta_i) \quad (3.45)$$

Once k_{yt} is obtained, by the dispersion relation (3.44) in Region 2, k_t can be calculated. Thus, the transmission angle is

$$\theta_t = \arcsin(\frac{k_{yt}}{k_t}) \quad (3.46)$$

The relation between incident angle and transmission angle is more complicated than that represented by the Snell's Law. It depends on the shape of the Yee cells and the refraction indices of the two regions.

In the following discussions, suppose that we have a plane wave of 1GHz frequency propagates in a 2D FDTD grid. Figures 3.5 - 3.8 show the transmission angle in different situations.

In Figure 3.5, the media in both sides are the same. Theoretically, the transmission angle is equal to the incident angle. However, as shown in Figure 3.5, the transmission angle is different from the incident the angle and difference is related to the cell size and incident angle. When dx_1=dx_2, the FDTD solution is exactly the same as the theoretical one. This solution is trivial because there is only one FDTD grid and homogeneous medium. If dx_2 is smaller than dx_1, the difference is not big. However if dx_2 is bigger than dx_1, the difference increases very quickly as the dx_2 increases. We can get the same conclusion intuitively. If dx_2 is bigger than dx_1, the numerical dispersion in Region 2 is bigger than that in Region 1 and this will influence the wave on the boundary significantly besides the numerical error caused by the different grid. This influence

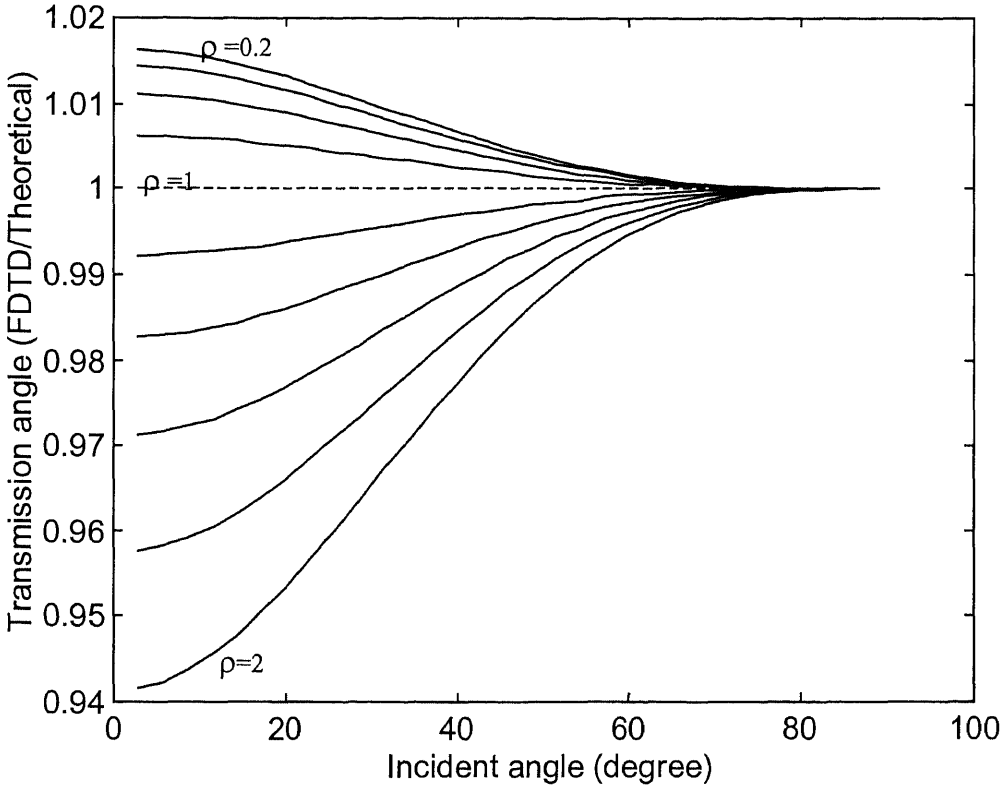

Figure 3.5 Two–dimensional FDTD numerical transmission angle, f=1GHz, $dx_1=\lambda_1/10$, $\varepsilon_1=\varepsilon_2=1$, $dy_1=dy_2=dx_1$. From top to bottom, $\rho=0.2$, 0.4, …., 2, $\rho=dx_2/dx_1$.

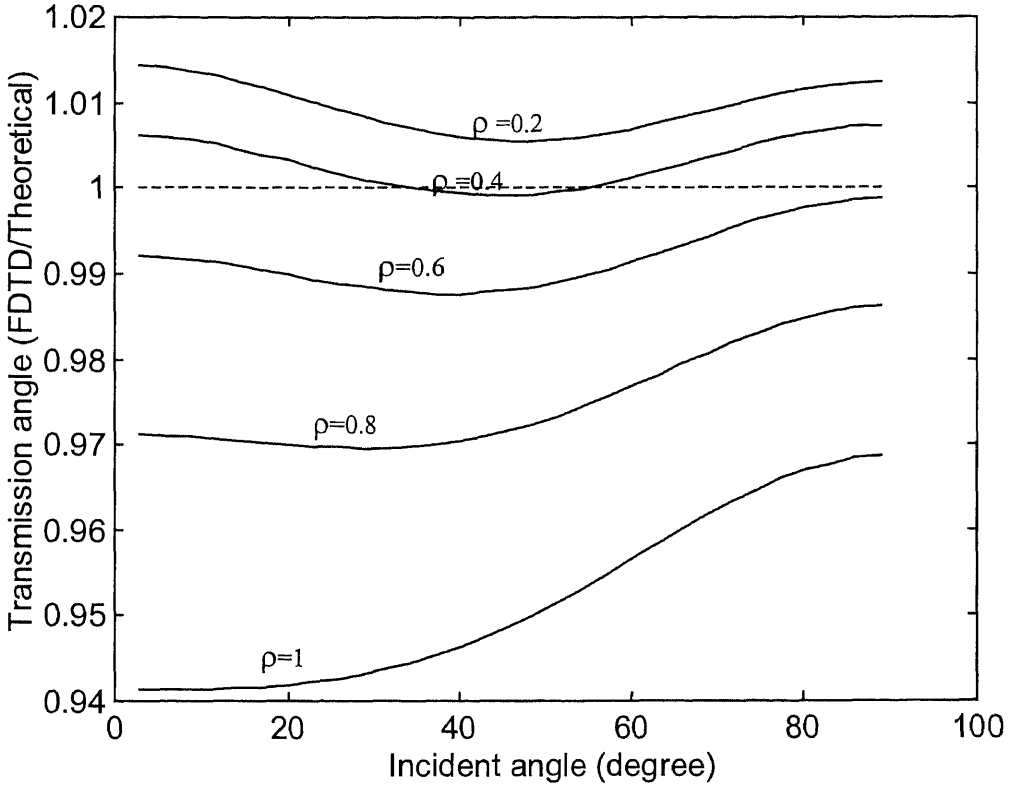

Figure 3.6 Two–dimensional FDTD numerical transmission angle, f=1GHz, $dx_1=\lambda_1/10$, $\varepsilon_2/\varepsilon_1=4$, and $dy_1=dy_2=dx_1$. Dashed line is the theoretical solution. $\rho=dx_2/dx_1$.

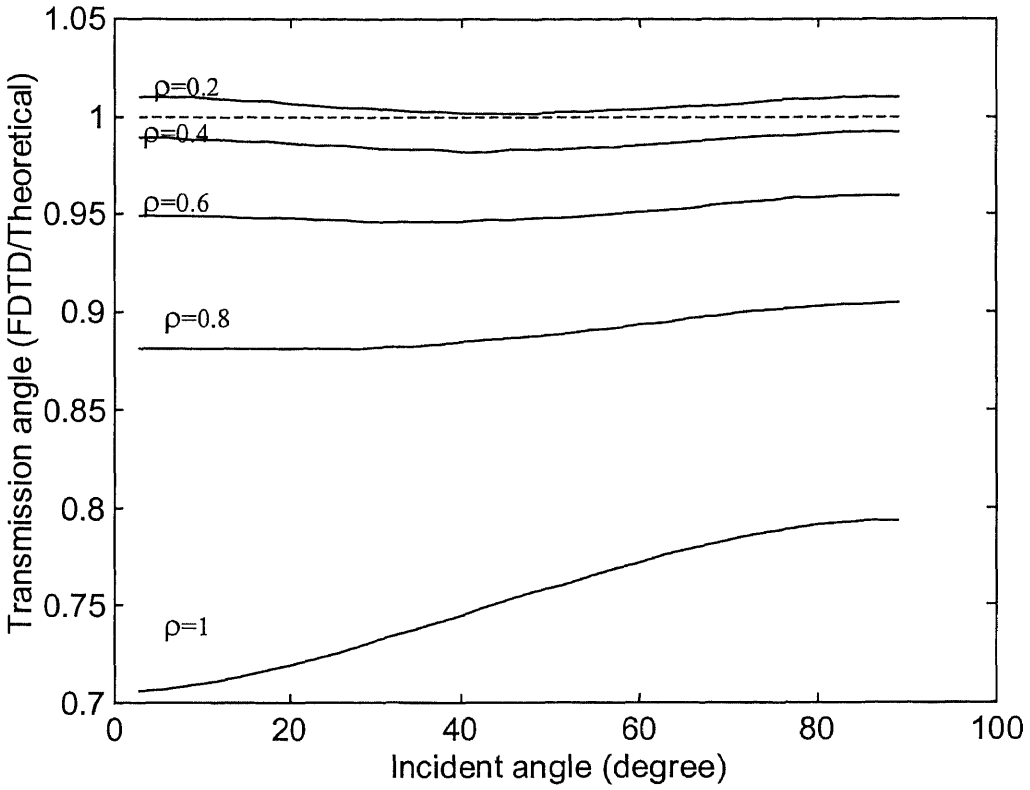

Figure 3.7 Two–dimensional FDTD numerical transmission angle, f=1GHz, $dx_1=\lambda_1/10$, $\varepsilon_2/\varepsilon_1=10$, and $dy_1=dy_2=dx_1$. Dashed line is the theoretical solution. $\rho= dx_2/ dx_1$.

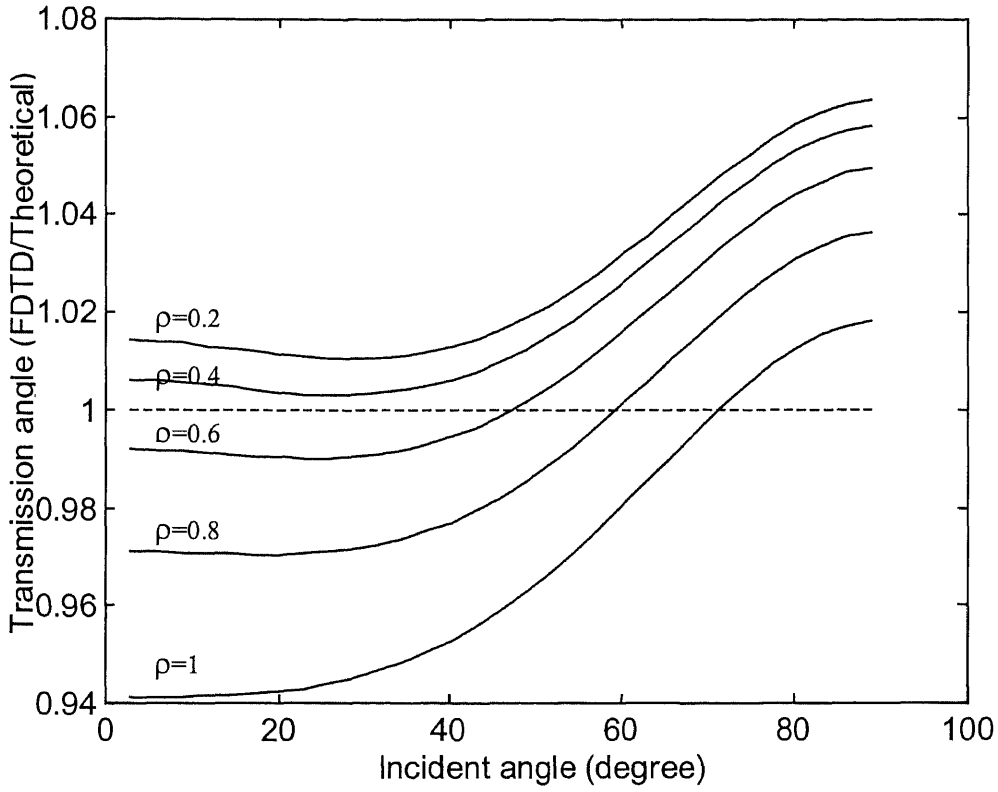

Figure 3.8 Two-dimensional FDTD numerical transmission angle, f=1GHz, $dx_1=\lambda_1/10$, $\varepsilon_2/\varepsilon_1=4$, and $dy_1=dy_2=2dx_1$. Dashed line is the theoretical solution. $\rho=dx_2/dx_1$.

increases rapidly when the cell size increases, and it is much smaller if we have a finer FDTD grid in Region 2.

In Figures 3.6 and 3.7, the media permittivities are different in both sides. In these cases, no matter what cell size is chosen, the FDTD transmission angle can no longer be equal to the theoretical solution. Also, with the theoretical reflection increasing, the error of the transmission angle increases. In Figure 3.6, $\varepsilon_2/\varepsilon_1=4$, which is not large. The transmission angle is close to the theoretical one. In Figure 3.7, $\varepsilon_2/\varepsilon_1=10$, which is much larger than that in Figure 3.6. The transmission angle is quite different from the theoretical one when the same cell size is used.

One interesting point is that the Yee cell shape also influences the transmission angle. In Figure 3.7, $dy=dx_1$ and in Figure 3.8, $dy=2dx_1$. The diagrams in these two cases are slightly different. These show that the FDTD grid is a kind of anisoptic medium and the direction of the medium can be changed by the cell shape. Although the diagram is not shown here, we can imagine that if dy is much bigger than dx_1, the FDTD transmission angle deviates far from the Snell's Law.

With the numerical transmission angle obtained, the numerical reflection coefficient can be calculated from (3.39) and (3.40). Figures 3.9 - 3.15 show the numerical reflection coefficients in different situations.

Figures 3.9 - 3.12 show the reflection coefficient of EM wave in parallel polarization.

In Figure 3.9, the media are the same. When dx1=dx2, R is equal to zero. When dx_2 is different from dx_1, R is not equal to zero but it is small if dx_2 is not too big compared with dx_1. In Figure 3.10, $\varepsilon_2/\varepsilon_1=4$, which is not very big. R is very close to the theoretical solution. In Figure 12, $\varepsilon_2/\varepsilon_1=10$, which is much bigger than that in Figure 3.10. R is quite

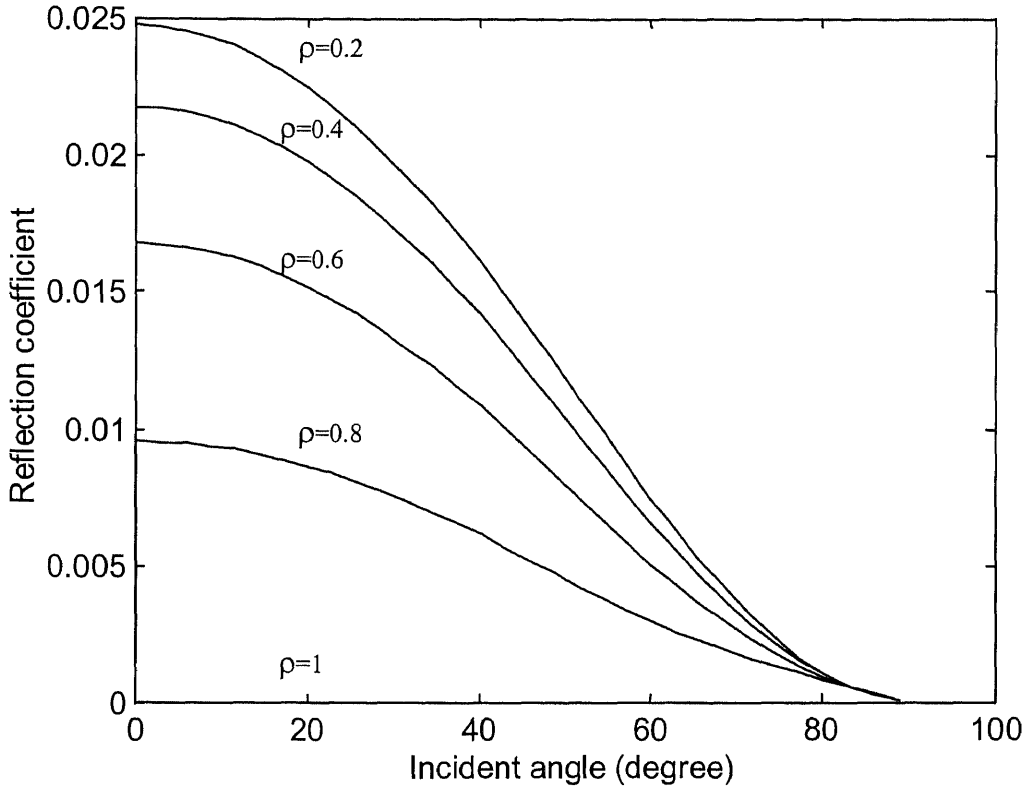

Figure 3.9 FDTD numerical reflection coefficients of an EM wave in parallel polarization, f=1GHz, $dx_1=\lambda_1/10$, $\varepsilon_2/\varepsilon_1=1$, and $dy_1=dy_2=dx_1$. $\rho=dx_2/dx_1$.

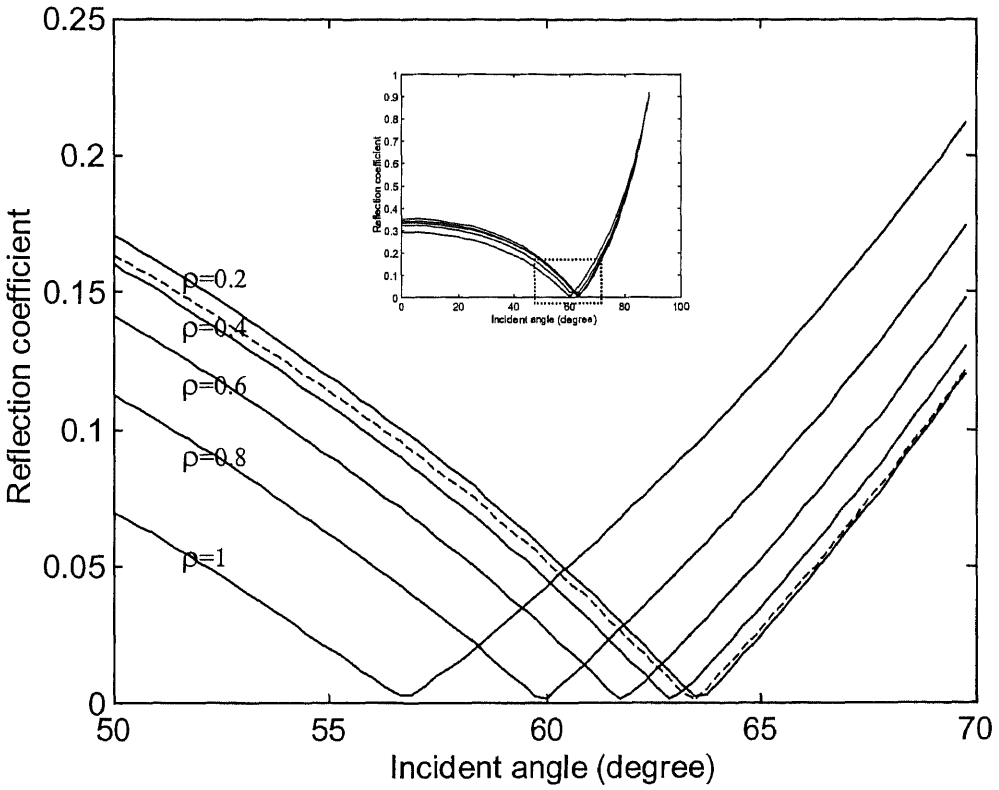

Figure 3.10 FDTD numerical reflection coefficients of an EM wave in parallel polarization, f=1GHz, $dx_1=\lambda_1/10$, $\varepsilon_2/\varepsilon_1=4$, and $dy_1=dy_2=dx_1$. The dashed line is the theoretical solution, and the solid lines are the FDTD numerical solutions. $\rho=dx_2/dx_1$.

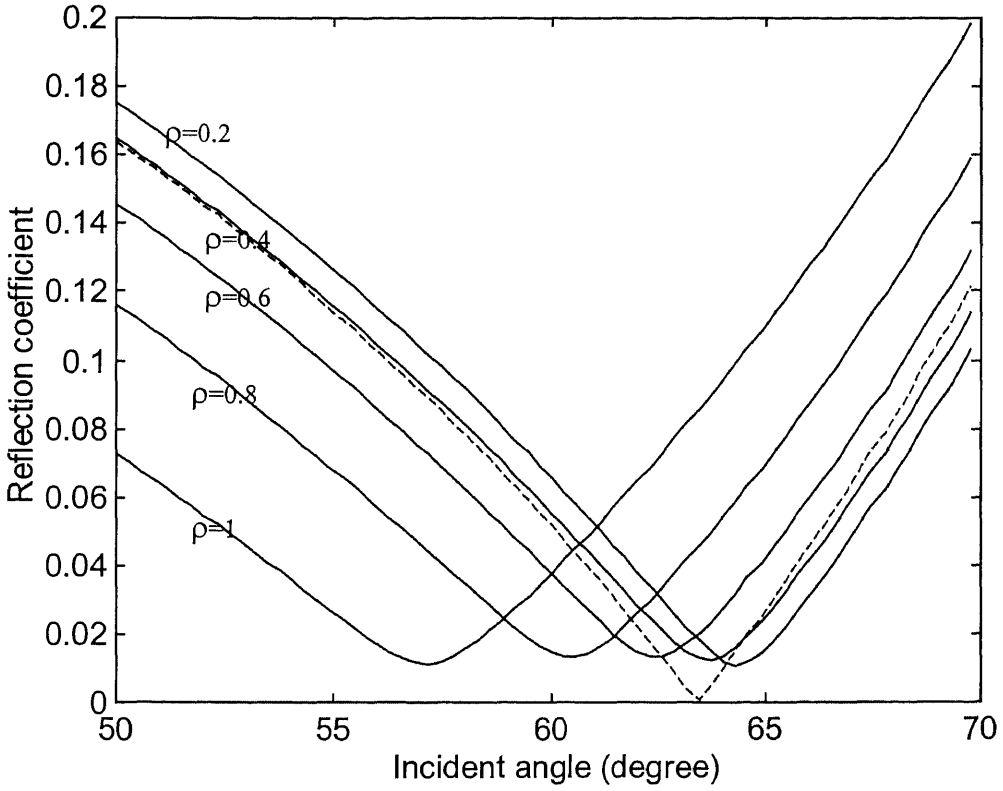

Figure 3.11 FDTD numerical reflection coefficients of an EM wave in parallel polarization, f=1GHz, $dx_1=\lambda_1/10$, $\varepsilon_2/\varepsilon_1=4$, and $dy_1=dy_2=3dx_1$. The dashed line is the theoretical solution and the solid lines are the FDTD numerical solutions. $\rho=dx_2/dx_1$.

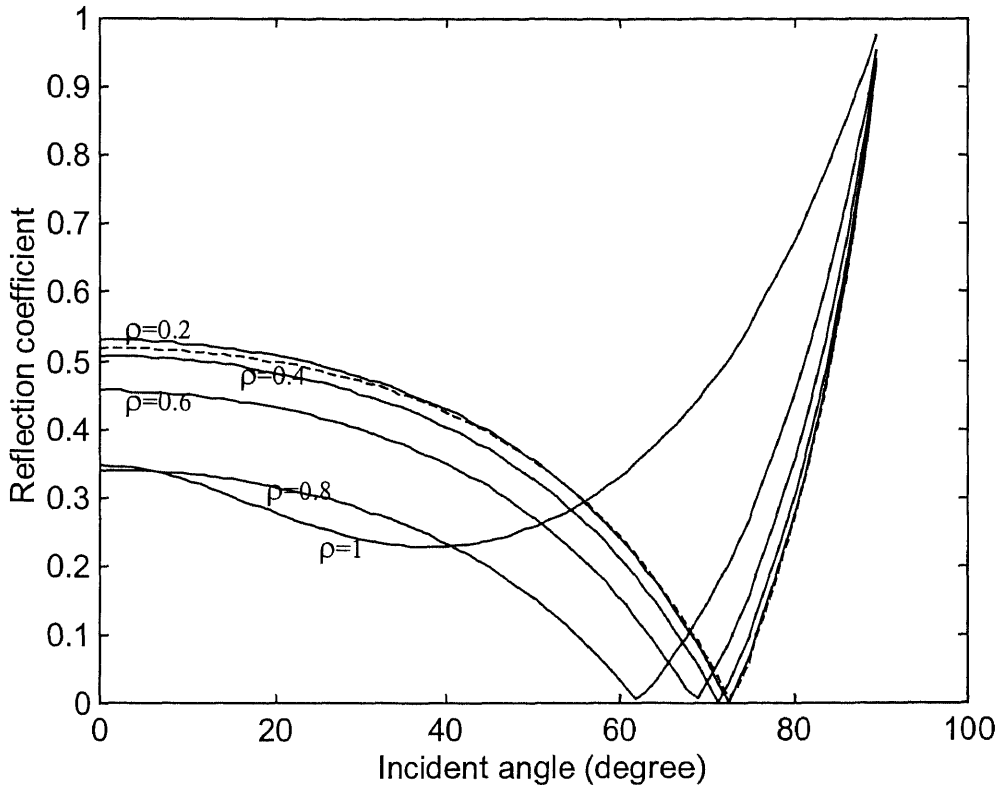

Figure 3.12 FDTD numerical reflection coefficients of an EM wave in parallel polarization, f=1GHz, $dx_1=\lambda_1/10$, $\varepsilon_2/\varepsilon_1=10$, and $dy_1=dy_2=dx_1$. The dashed line is the theoretical solution and the solid lines are the FDTD numerical solutions. $\rho=dx_2/dx_1$.

different from the theoretical solution. In order to improve the accuracy, dx_2 has to be smaller. The numerical and theoretical Brewster angles are also shown in Figures 3.10 and 3.12.

The grid shape also has influence on the numerical reflection. The situation described in Figure 3.11 is the same as that in Figure 3.10 except dy. It is observed that increasing dy even makes the Brewster angle disappear.

From Figures 3.9 - 3.12, we can conclude that in a dense medium the cell size has to be small and the upper bound of the cell size depends on the medium permittivity and required accuracy. Thus, before the simulation, the numerical reflection coefficient R has to be predicted based on (3.39) and (3.40) so that the simulation could run more smoothly.

Similar discussions can apply to the EM wave in perpendicular polarization, which has quite different bahavior from that of parallel polarization. The diagrams of numerical reflection coefficients are shown in Figures 3.13 - 3.15 to demonstrate behaviors in various situations.

3.5. Conclusion

In this chapter, the FDTD numerical error in an inhomogeneous medium is derived and discussed. This work provides the numerical electromagnetic wave behavior in the interface of two adjacent media discretized by a non-uniform grid. The results in this chapter are of essence to an FDTD grid construction and will be further implemented into FDTD simulation to achieve the desired simulation accuracy and reduce computational cost.

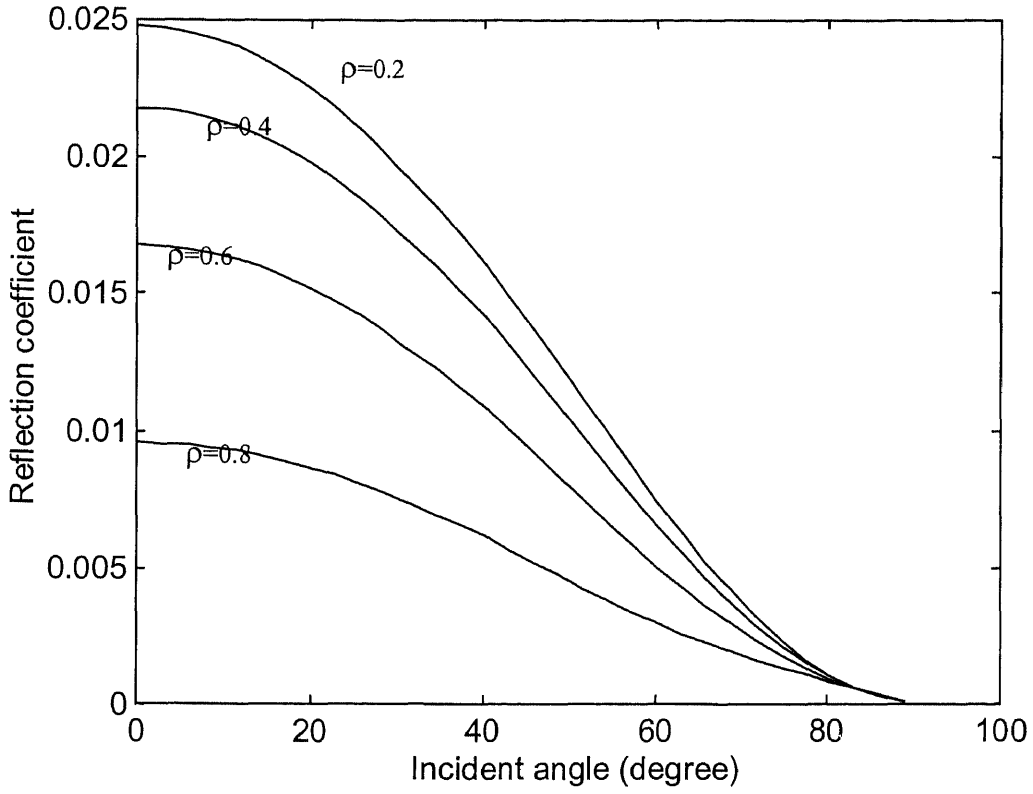

Figure 3.13 FDTD numerical reflection coefficients of an EM wave in perpendicular polarization, f=1GHz, $dx_1=\lambda_1/10$, $\varepsilon_2/\varepsilon_1=1$, and $dy_1=dy_2=dx_1$.

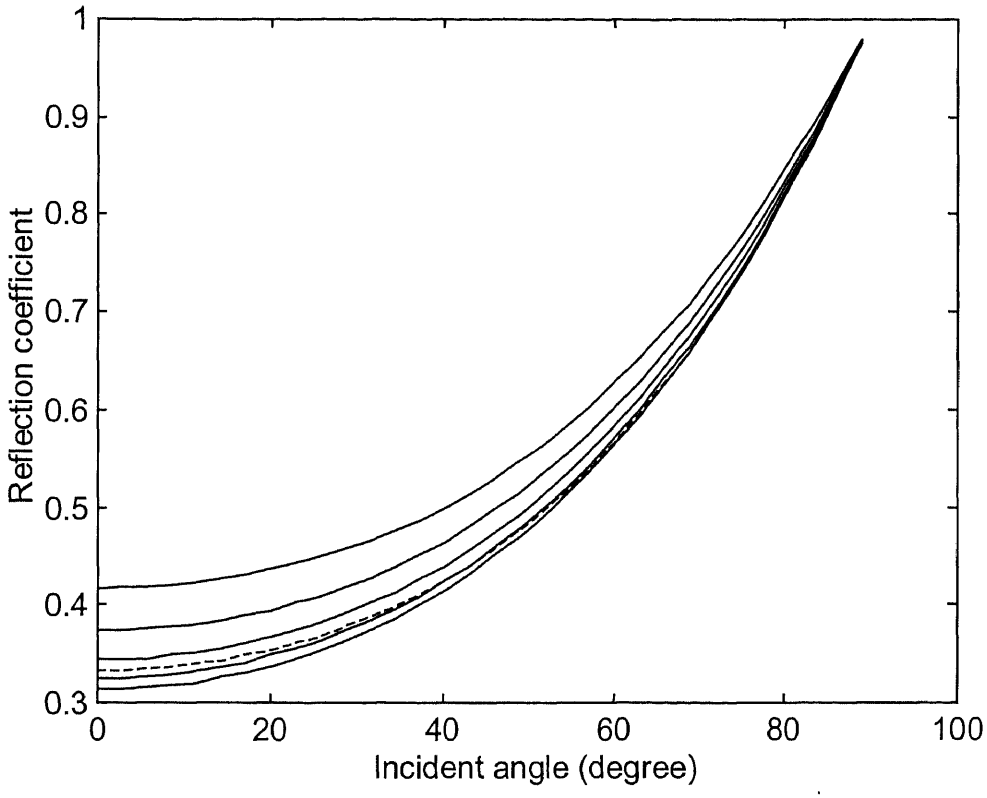

Figure 3.14 FDTD numerical reflection coefficients of an EM wave in perpendicular polarization, f=1GHz, $dx_1=\lambda_1/10$, $\varepsilon_2/\varepsilon_1=4$, and $dy_1=dy_2=dx_1$. Dashed line is the theoretical solution, and the solid lines are FDTD solutions, from top to bottom, the ratios of dx_2/dx_1 are 1, 0.8, 0.6, 0.4, and 0.2, respectively.

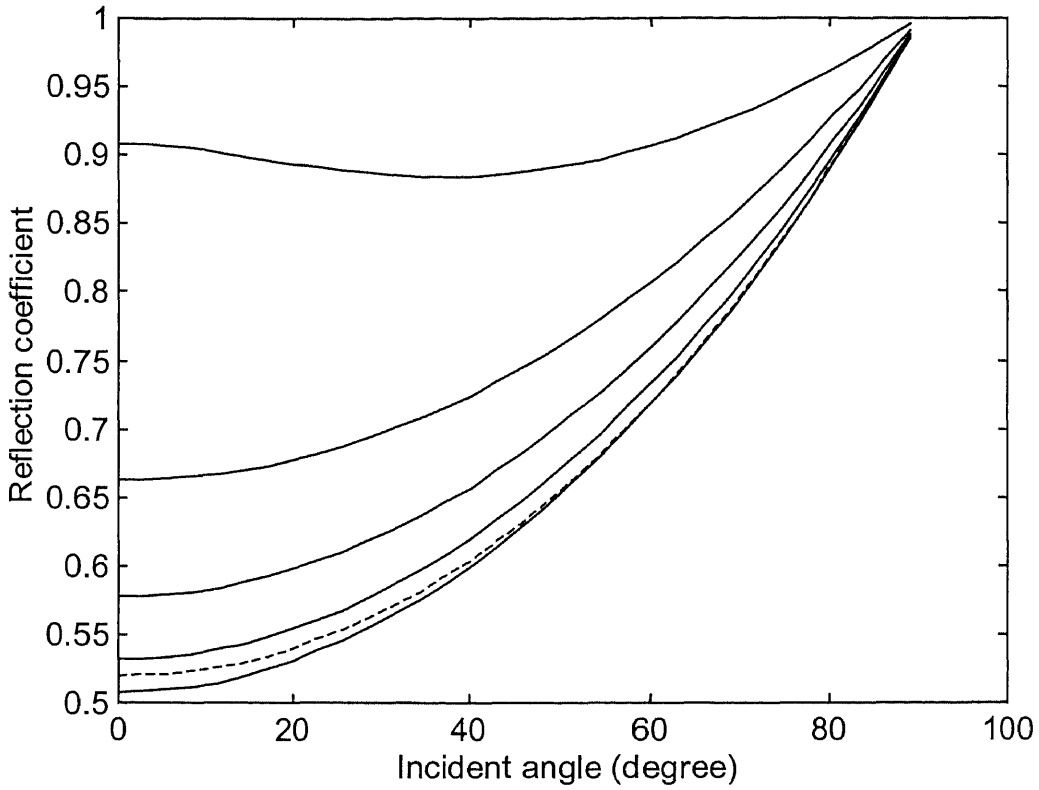

Figure 3.15 FDTD numerical reflection coefficients of an EM wave in perpendicular polarization, f=1GHz, $dx_1=\lambda_1/10$, $\varepsilon_2/\varepsilon_1=10$, and $dy_1=dy_2=dx_1$. Dashed line is the theoretical solution, and the solid lines are FDTD solutions, from top to bottom, the ratios of dx_2/dx_1 are 1, 0.8, 0.6, 0.4, and 0.2, respectively.

CHAPTER 4

HYBRID SYSTEM CO-SIMULATION MODEL

4.1. Introduction

A hybrid EM system is defined as a system consisting of two parts, the distributed one in which field effects have to be considered, and the electrically small lumped one where only voltage and current relations of those lumped elements are considered. The fundamental simulation model for a hybrid system is to include lumped elements into the FDTD method, or on the other hands, treats the FDTD simulation as a module in a circuit simulation package to solve the field effect problems in a circuit simulation. The work is a combination of two tasks, the field analysis and the circuit simulation. According to the focus of a practical problem, the simulation can be treated as a circuit simulation with field effects solved by FDTD, or an FDTD simulation with lumped elements handled by a circuit solver. Because the circuit and field analyses are both involved in one simulation procedure, it is called co-simulation procedure.

4.2. Hybrid System Model

In traditional EM simulations, an EM system is either treated as a distributed system or a circuit. Both of them already have mature simulation approaches. The circuit method either ignores the wave propagation in the system or uses lumped elements, such as transmission line, to approximate the distributed structures in the system. Let alone there are many structures that are hard to find an appropriate model, the characteristics of some simple EM structures, such as microstrip line, change in different frequency ranges.

Therefore the circuit method is showing more and more limitations in high frequency ranges. On the other hand, the pure field analysis of an EM system with lumped elements is basically unnecessary and impossible. From system analysis points of view, the EM field inside each lumped element does not to be simulated. It is normally very complicated and has quite different mechanisms other than EM theory. The characteristics of all the lumped elements are the topics of other areas and assumed available for our usage. The focus in an EM system simulation is the behavior of the whole system, such as the scattering parameters of the system, the EM field distribution in the system, and the EM radiation of the system. Therefore, a good approximation of a practical system is very helpful for us to understand the property of the EM system.

A hybrid system model is built for the system analysis purpose. The build-up of a hybrid system is based on the assumption of lumped elements, which are electrically small elements compared with EM wavelength. Each lumped element is simplified as a current lying on the FDTD grid and the complicated distributed structure is put into the FDTD grid. The system behaviors, including the interaction of lumped elements and EM field and other field effects, can be obtained in one time FDTD simulation run.

Although the computational cost is higher than that of circuit methods, it provides a comprehensive description of the system without too much simplification in the simulation. By one time run, the time domain and wide band spectrum responses can be obtained. As the computer speed increases, it will be more plausible in the analysis and design for practical EM systems.

4.3. Modified Lumped Current Algorithm

As shown in Figure 2.3 in Chapter 2, a hybrid system contains a distributed system and a lumped element. The whole FDTD computational domain is filled with Yee cells, surrounded by absorbing boundaries because the system is an open system. A and B are two nodes between which the lumped element is connected with the distributed system. According to [Sui et al 1992], a lumped current generated by the lumped element flows from A to B. The cells through which the lumped current passes are called lumped cells.

Without losing generality, assume that line AB, as shown in Figure 2.3, is parallel to x-axis and positions for A is (i_s, j, k) and B is (i_e, j, k). Maxwell's equations modified by the lumped current algorithm are

$$\oint \boldsymbol{E} \cdot d\boldsymbol{l} = -\oiint \mu \frac{\partial \boldsymbol{H}}{\partial t} \cdot d\boldsymbol{S} \tag{4.1}$$

$$\oint \boldsymbol{H} \cdot d\boldsymbol{l} = I_{lumped} + \oiint (\varepsilon \frac{\partial \boldsymbol{E}}{\partial t} + \sigma \boldsymbol{E}) \cdot d\boldsymbol{S} \tag{4.2}$$

The lumped current I_{lumped} shown in (4.2) represents the effects of the lumped element between A and B. Because the lumped current flows in x direction, only the Ex FDTD equation is modified as

$$\oint \boldsymbol{H}^{n+1/2} d\boldsymbol{l} = I_{lumped} + \frac{E_x^{n+1} - E_x^n}{dt} \oiint \varepsilon ds + \frac{E_x^{n+1} + E_x^n}{2} \oiint \sigma ds \tag{4.3}$$

The lumped current is the function of the voltage across A and B, V_{AB}, which is equal to the integration of electrical field from A to B.

$$I_{lumped} = g(V_{AB}) = g(\sum_{i=i_s}^{i=i_e} dx_i E_{xijk}) \tag{4.4}$$

Note that the time step of lumped current in (4.3) is not indicated because there are several approaches to obtain it. The lumped current expression (4.4) can be expressed in the following forms

$$I_{lumped} = f(E^{n}_{x(i_{s....e})jk}) \tag{4.5}$$

$$I_{lumped} = f(E^{n}_{x(i_{s....e})jk}, E^{n+1}_{x(i_{s....e})jk}) \tag{4.6}$$

$$I_{lumped} = f(E^{n+1}_{x(i_{s....e})jk}) \tag{4.7}$$

f is a known function coming from (4.4).

If there is only one cell between nodes A and B, normally (4.6) is utilized in the following form

$$I_{lumped} = f(\frac{E^{n}_{xi_l jk} + E^{n+1}_{xi_l jk}}{2}) \tag{4.8}$$

in which $i_l=i_s=i_e$ is the x index of the lumped element position. Then (4.3) is an equation with one unknown and can be solved by linear or nonlinear methods.

If there are multiple cells from A to B, (4.3) represents an equation system in which unknowns are Ex values in the cells between A to B. Substituting (4.5) - (4.7) into (4.3) generates explicit or implicit schemes to update electric field components, respectively.

With (4.5) substituted into (4.7), explicit expressions of Ex values can be generated from (4.3). This is the most convenient approach to couple the lumped current to FDTD equations. However, this approach drives the FDTD simulation diverge rapidly sometimes even to a linear component, such as a resistor. Generally, this pure explicit approach can only be used to small signal systems.

When the lumped element spans many cells or consists of nonlinear components, normally the semi-implicit form (4.6) has to be used into (4.3) to update the electrical

field of the lumped cells. Semi-implicit scheme generally improves numerical stability. However the computational cost is much higher than that of explicit one. With this scheme, (4.3) represents an equation system, which may be linear or nonlinear depending upon the lumped element characteristic. For some extremely nonlinear lumped elements, the FDTD time step has to be reduced to compromise the stability. [Ciampolini et al 1996] designed an adaptive time step scheme to reduce the computational burden.

An alternate explicit expression of I_{lumped} can be substitute into (4.3). Suppose Ex value in the cell i=p is be updated by (4.3). The expression form of I_{lumped} of this cell is

$$I_{lumped} = g(dx_i E_{pjk}^{n+1} + \sum_{\substack{i=is \\ i\neq p}}^{i=ie} dx_i E_{xijk}^{n}) \tag{4.9}$$

in which the E_x^{n+1} at p cells and E_x^n at the rest cells are used to express I_{lumped}.

Compared with pure explicit expression (4.5), (4.9) improves the stability when the lumped element spans only two or three cells due to one Ex value used implicitly in (4.9). Several equations, each of them has only one unknown, have to be solved. If there are many cells between nodes A and B, the stability performance of this semi-explicit scheme is very close to the pure explicit scheme.

The scheme proposed in this dissertation substitutes (4.7) into (4.3) to obtain an implicit scheme. Like the semi-implicit scheme, this scheme normally generates an equation system of Ex. However, this equation system can be simplified according to the following derivation.

With I_{lumped} defined at the same time when the electric field components are evaluated, (4.3) can be rewritten as

$$\oint \boldsymbol{H}^{n+1/2} d\boldsymbol{l} = I_{lumped}^{n+1} + \frac{E_x^{n+1} - E_x^n}{dt} \oiint \varepsilon ds + \frac{E_x^{n+1} + E_x^n}{2} \oiint \sigma ds \tag{4.10}$$

With the consideration of inhomogeneous media and three-dimensional non-uniform grid, both sides of (4.10) are discretized as

$$LHS = (H_{yijk-1}^{n+1/2} - H_{yijk}^{n+1/2}) \cdot \frac{dy_{j-1} + dy_j}{2} + (H_{zijk}^{n+1/2} - H_{zij-1k}^{n+1/2}) \cdot \frac{dz_{k-1} + dz_k}{2} \tag{4.11}$$

$$RHS = I_{lumped}^{n+1} + (E_{xijk}^{n+1} - E_{xijk}^{n})A + (E_{xijk}^{n+1} + E_{xijk}^{n})B \tag{4.12}$$

where

$$A = \frac{\sum_{p=j-1}^{j} \sum_{q=k-1}^{k} \varepsilon_{ipq} dy_p dz_q}{4dt} \tag{4.13}$$

$$B = \frac{\sum_{p=j-1}^{j} \sum_{q=k-1}^{k} \sigma_{ipq} dy_p dz_q}{8} \tag{4.14}$$

From (4.11) and (4.12), the expression of E_x^{n+1} at cell position (i,j,k), ($i_s \le i \le i_e$) is

$$E_{xijk}^{n+1} = -I_{lumped}^{n+1} \cdot \Gamma_{ijk} + \mathrm{K}_{ijk} \tag{4.15}$$

where

$$\Gamma_{ijk} = \frac{1}{A+B} \tag{4.16}$$

$$\mathrm{K}_{ijk} = \frac{1}{A+B} LHS + \frac{A-B}{A+B} E_{xijk}^{n} \tag{4.17}$$

The voltage between A and B is equal to the integration of E_x^{n+1} from A to B,

$$V_{AB}^{n+1} = \sum_{i=i_s}^{i_e-1} dx_i \cdot E_{xijk}^{n+1} = -I_{lumped}^{n+1} \sum_{i=i_s}^{i_e-1} dx_i \Gamma_{ijk} + \sum_{i=i_s}^{i_e-1} dx_i \mathrm{K}_{ijk} \tag{4.18}$$

(4.18) can be rewritten in the following form

$$I_{EM}^{n+1/2} = \frac{V_{AB}^{n+1}}{R_{grid}} + I_{lumped}^{n+1} \tag{4.19}$$

where

$$I_{EM}^{n+1/2} = \frac{\sum_{i=i_s}^{i_e-1} dx_i \mathrm{K}_{ijk}}{\sum_{i=i_s}^{i_e-1} dx_i \Gamma_{ijk}} \tag{4.20}$$

$$R_{grid} = \sum_{i=i_s}^{i_e-1} dx \Gamma_{ijk} \tag{4.21}$$

In (4.19), I_{lumped}^{n+1} and V_{AB}^{n+1} is a current and voltage pair that defines a two-terminal lumped element connected to the EM system. The lumped element can be any arbitrary complex circuit, active and nonlinear, and solved by Newton-Raphson method or, in general, by a circuit simulator like SPICE. The current (I_{lumped}^{n+1}) flows through the lumped circuit terminal. With Equations (4.15) and (4.19), it is coupled into the EM system by updating the electrical field at each lumped cell in each iteration. It can be easily shown that the integration of the newly updated Ex along the lumped cells' path equals to V_{AB}^{n+1}.

Thus starting from (4.8), the equation system caused by an implicit expression of I_{lumped} is replaced to a single equation (4.19) and a bunch of explicit expressions of Ex from (4.15). Compared with the semi-implicit scheme, this scheme greatly releases the computational burden. Compared with the alternate explicit scheme derived from (4.10), with a significant improvement of stability, it even has less computational cost.

4.4. Hybrid System Co-Simulation Model

In the above discussion, the focus is on the computational cost and stability of the FDTD simulation process. Furthermore, the modified lumped current algorithm, represented by (4.15) and (4.19), provides a systematic approach for modeling and solving hybrid systems.

Equation (4.19) provides the interface between a distributed system, computed by FDTD, and a lumped element, described by circuit method. It can be represented as an equivalent model, field-circuit model, illustrated in Figure 4.1. R_{grid} is an equivalent resistor determined by the grid length, material properties (conductance, permittivity, and permeability) around lumped cells and also the FDTD time increment, as shown in (4.21). When the media properties do not vary with EM field, R_{grid} is a constant for a given FDTD grid and simulation parameters. $I_{EM}^{n+1/2}$ is a controlled current source in circuit simulation and its current value is determined by the EM field values at previous time step, as shown in (4.20).

Figure 4.1 shows the interaction between the EM distributed system and an embedded lumped circuit in a hybrid system co-simulation. From the EM system point of view, the effect of the lumped circuit is treated as an external current (I_{lumped}^{n+1}) added into Ampere's law. From the lumped circuit point of view, the effect of the distributed EM system is treated as an equivalent controlled current source ($I_{EM}^{n+1/2}$) and an equivalent resistor (R_{grid}). In every FDTD iteration, in order to update the electrical field components in lumped cells, FDTD has to provide the information of the controlled current source value at this time step to its corresponding equivalent lumped circuit. Once the values of the controlled current source and R_{grid} are known, a circuit simulation can be performed, therefore providing the terminal lumped current value for next FDTD iteration.

By the field-circuit model discussed above, the simulation of a hybrid system is de-coupled into two separate processes, FDTD and circuit simulations, which are interconnected by two simple intermediate parameters, $I_{EM}^{n+1/2}$ and I_{lumped}^{n+1}. Each process is undertaken by its corresponding numerical method, respectively. In the FDTD iteration,

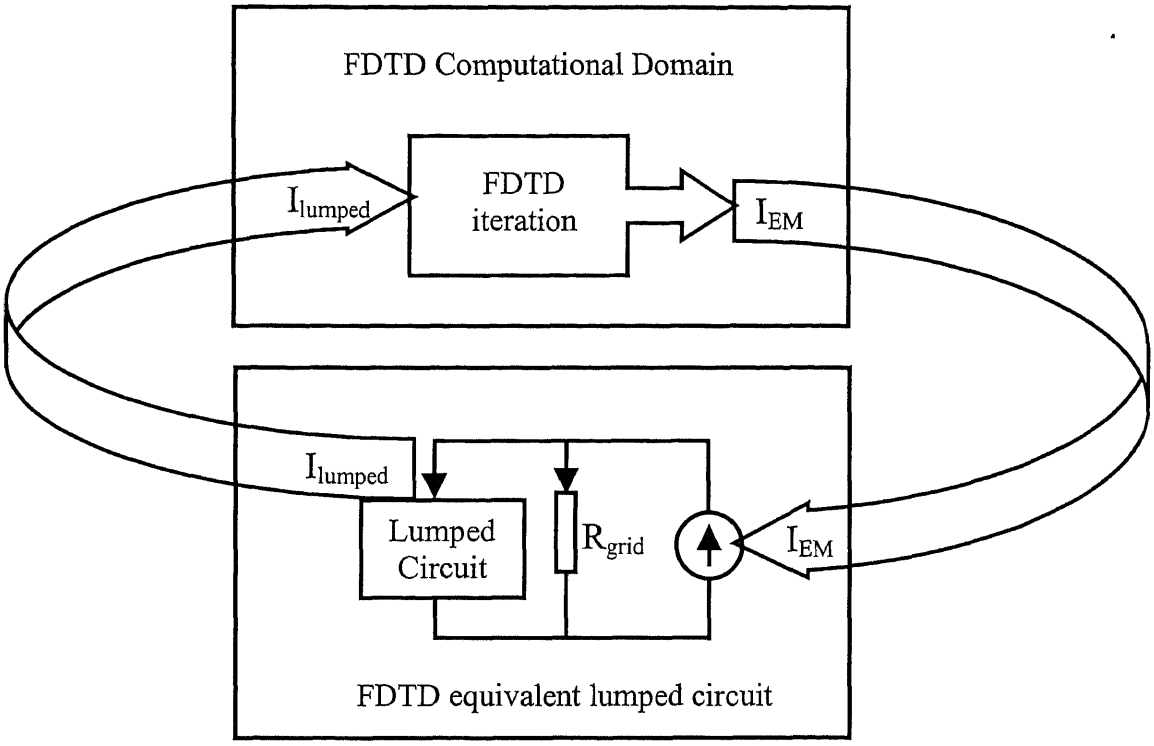

Figure 4.1 Field-circuit model for hybrid system co-simulation

the only parameter needed from the lumped circuit is the lumped current value of the present time step; in circuit simulation, only $I_{EM}^{n+1/2}$ is needed. Hence, the simulation of a hybrid system is completed by co-simulation process, which consists of FDTD and circuit simulations interacted through the proposed field-circuit model.

One important note about the field-circuit model is, during its derivation, no assumption for field distribution across the lumped cells is made. Therefore, spatial distribution of EM field in lumped cells can be calculated accordingly, not under uniform assumption. For the FDTD simulation, the use of implicit I_{lumped}^{n+1} in the lumped FDTD formulation improves the stability due to embedded linear or nonlinear lumped elements. For the circuit simulation, only a positive resistor and a linear controlled current source are added into its original circuit, the stable condition of the circuit simulation does not change. As demonstrated by the test cases in the following section, the time increment based on CFL criterion does not need to be changed to make the FDTD algorithm stable and accurate, even in very large signal cases, meaning that the FDTD computational efficiency is not compromised with the presented model.

4.5. Numerical Validation

Several hybrid system examples are used to verify the accuracy and stability of the newly developed field-circuit co-simulation model.

Figure 4.2 shows a two-dimensional hybrid system configuration that is used in many test cases. Different types of lumped elements are connected as the lumped load at the right-hand side of the parallel-plate lossless transmission line. In these examples, large signals and specifically designed circuit status that caused instability in the previous

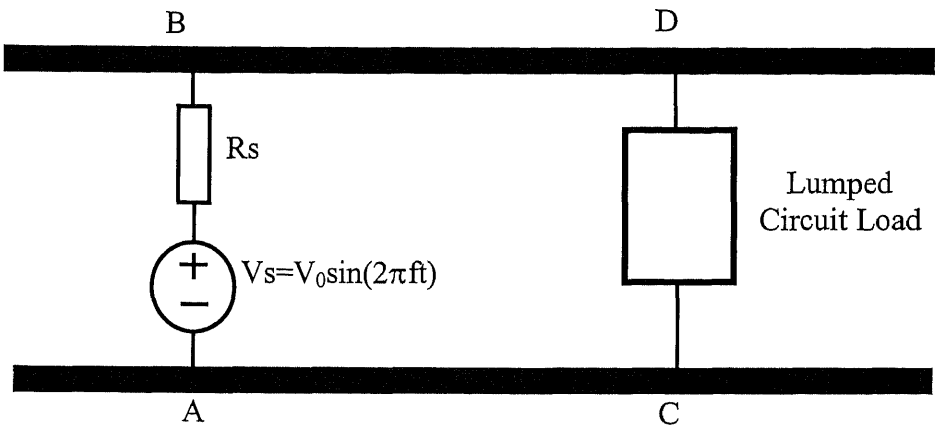

Figure 4.2 A hybrid system configuration.

lumped current algorithm are chosen to test the stability of this new model. Unless otherwise mentioned, the FDTD grid is uniform with cell size of 0.001m and time step of 1.667ps. Each metal plate of the air-filled transmission line is modeled as one layer of cells, and its conductance is 10^7 Ω/m.

In this chapter, 2D simulations are utilized in order to provide satisfactory matching result to the existing commercial EE software. In the two-dimensional co-simulations, the near field effects and transient process are non-significant. In commercial EE software they cannot be taken into account. Thus the simulation conditions of the commercial EE software and our model are very close in the 2D simulation and they should bring very close results to the same structure. In Chapter 6, 3D simulations of several hybrid systems will be presented using this hybrid system co-simulation model.

4.5.1. Resistive Voltage Source with Capacitance Load

The lumped load, as shown in Figure 4.2, is a capacitor (C=1μF), Rs is chosen to be very small (Rs=0.0014Ω in this test case). The solution of hybrid co-simulation agrees very well with that SPICE simulation, as shown in Figure 4.3. Previous standard lumped current algorithm [Sui et al 1992] diverges quickly when Rs is very small. The resistive lumped voltage source of this test case is also discussed in [Xu et al 1997], where a linear equation set was solved in order to get a stable FDTD result when Rs is small. In the field-circuit model, the value of Rs does not influence the simulation stability at all.

If the Rs is so small that the transient process is faster than FDTD iteration speed, then FDTD methods can not provide an accurate result. However, it is still stable for the field-circuit model and the steady state response may be still valid in some situations.

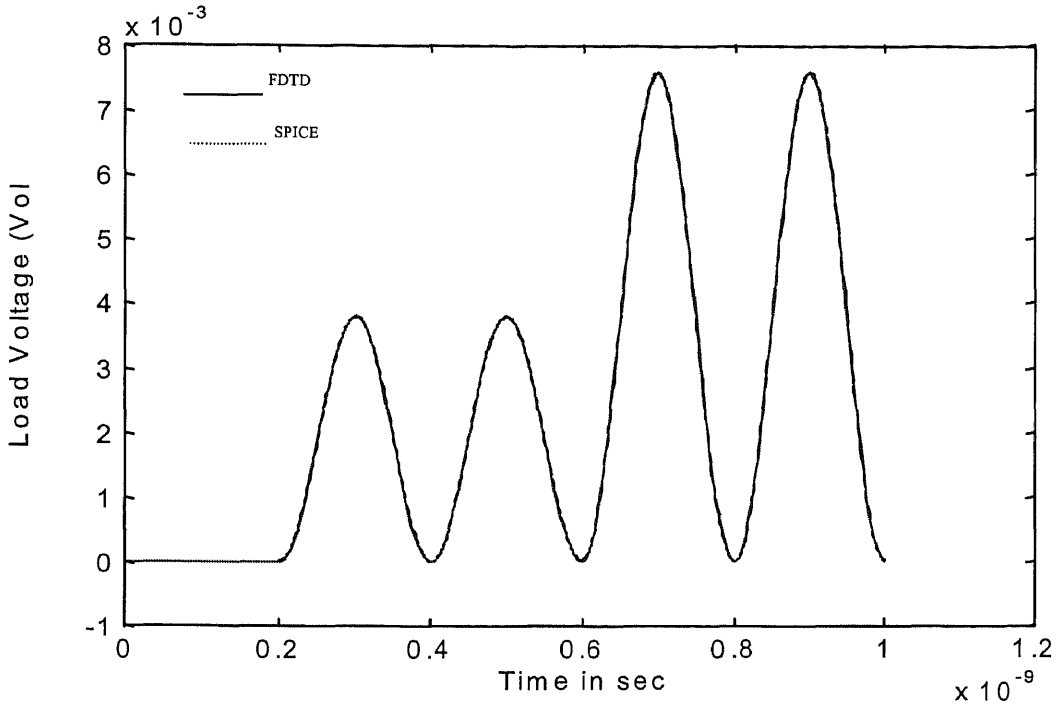

Figure 4.3 Test Case 1: agreement of the co-simulation method and SPICE. Source: R_s=0.001Z0, V_0=90V, f=5GHz; transmission line in Figure 4.2: BD=0.06m, AB=0.008m, Z0=3.01379Ω; Load: C=1μF

Figure 4.4 shows the result of an exponential-rise resistive Dc voltage source charging a capacitor made of parallel metal plates. The EM field starts from the source then spreads to the volume of the capacitor in a wave propagation manner. In this case the voltage source first charges the area nearby, thus the transient charging time constant is so small that the FDTD temporal increment cannot catch the speed of the change of the charging current. This process is significantly shown in a high-speed transient process. When the system approaches its steady state, for an electrically small system like that shown in Figure 4.4, the wave propagation has smaller effect. The theoretical solution in Figure 4.4 is obtained by assuming the capacitor is a lumped element, which means that the EM field in the capacitor changes uniformly and the wave propagation from source to the other places is accomplished instantly. This assumption is true when the wave propagation has negligible effect to the system response. As shown in Figure 4.4, initially, the FDTD solution oscillates around the theoretical solution with very big amplitude because of the wave propagation effects and the transient process with speed higher than that of the FDTD simulation. But, when the current changing is small, the FDTD solution converges to the theoretical one very well. In this case, it still can be seen that the wave propagation causes the deviation of FDTD results from the theoretical solution, but its effect is much smaller than that during the initial time. This shows the robustness of the proposed field-circuit model.

4.5.2. Resistive Voltage Source with Diode Load

Next the lumped load in Figure 4.2 is replaced by a Schottky diode, with its I-V relation given by

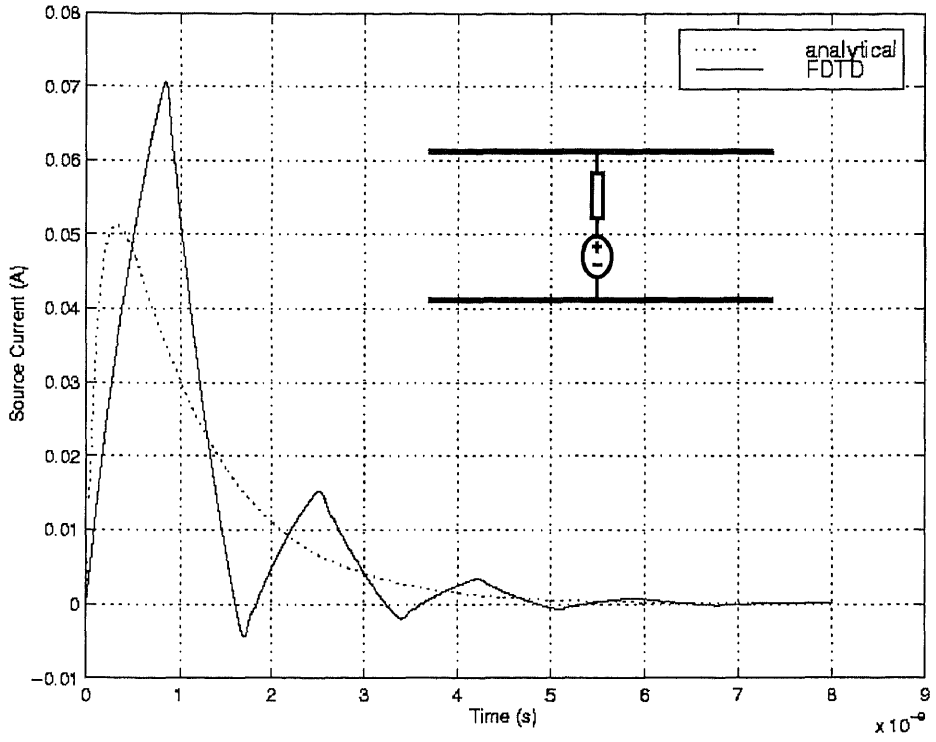

Figure 4.4 The charging current to a capacitor by an exponential-rise resistive Dc voltage source. Rs=2Ω, Voltage source: V=1-exp(-t/τ), τ=1ns, and C is made a pair of parallel metal plates, 80mm*80mm*8mm, filled with air. Dashed line is the theoretical solution and the solid line is the co-simulation solution

$$I_d = I_0(e^{\frac{qVd}{nkT}} - 1) \tag{4.22}$$

where V_d is the voltage across the diode, k is Boltzmann constant, T is operating temperature, n is the diode ideality factor and it is set to be 1 in the simulations.

This circuit has been studied previously to see how to solve the instability caused by the nonlinear lumped circuit [Picket-May et al 1996, Durney et al 1996, Caimpolini 1996 et al]. In order to challenge the stability of the new model, the amplitude of the voltage source is set to be very high. As shown in Figure 4.5, the hybrid FDTD and SIPCE results match very well when the load voltage is 30V. In fact, a much higher voltage, peaked diode voltage of 120V, was tested and good agreement between SPICE and FDTD still holds.

4.5.3. The Bipolar Junction Transistor Load

The circuit is shown in Figure 4.6 (a), where Vcc and Rc provide bias DC voltage and current to the transistor, and the transmission line is the same as that of Case 1. Ebers-Moll model is used to model the bipolar junction transistor (BJT) here.

From the FDTD grid side, one can see just the base-emitter junction across the transmission line. The existence of other parts of the transistor circuit is represented by their influence on the current flowing into the base junction. In other words, the rest of the transistor load circuit is hidden in the lumped circuit box, as shown in Figure 4.6(a).

The lumped circuit for the transistor load case based on field-circuit model is shown in Figure 4.6(a). According to the Ebers-Moll transistor model shown in Figure 4.6(b), the following two equations (4.23) and (4.24) handle the coupling the current in *be* and *bc* junctions

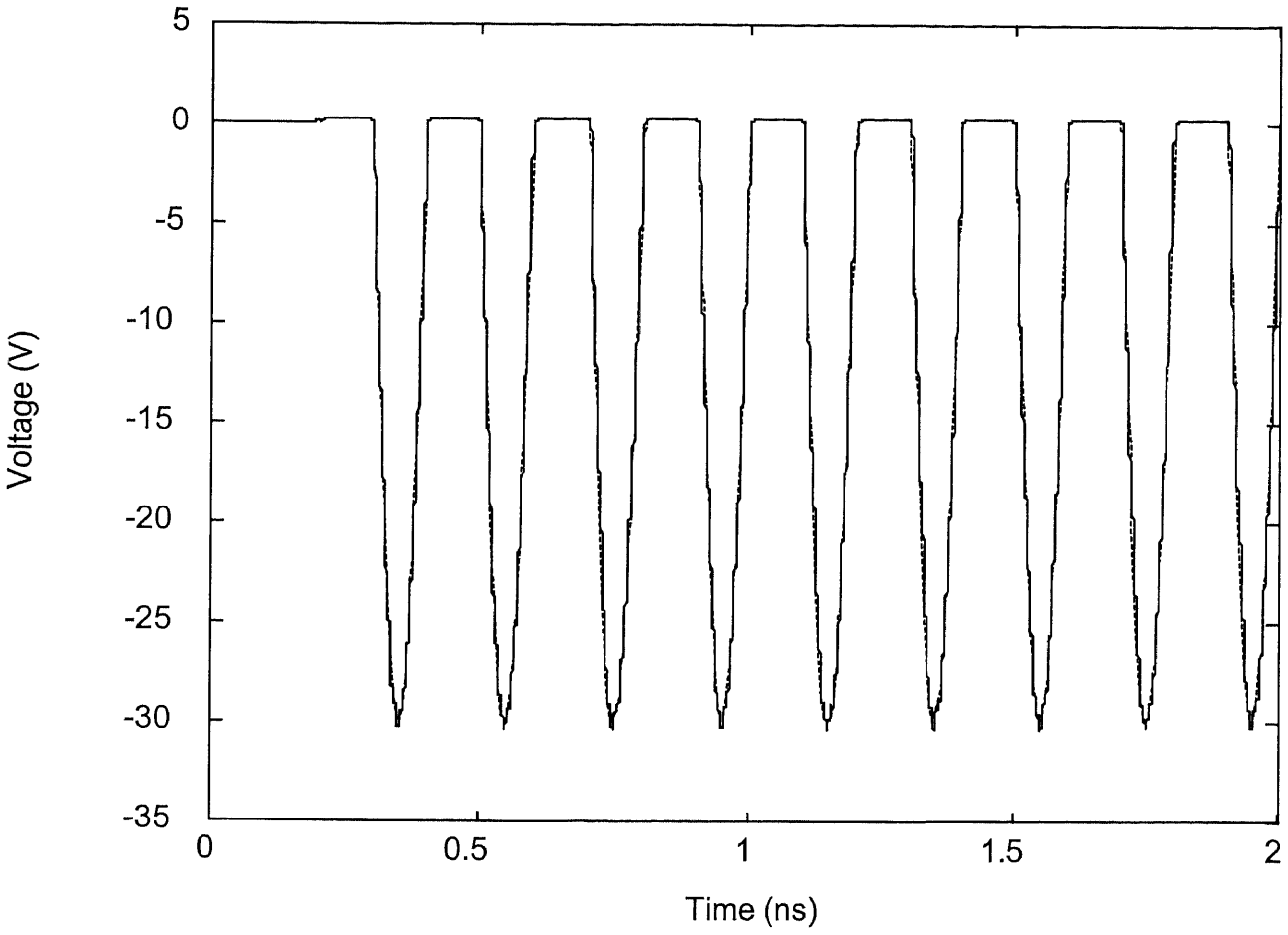

Figure 4.5 Test case 2: Voltage profile of the Schottky diode load shown in Figure 4.2. Dashed line: SPICE solution. Solid line: co-simulation solution

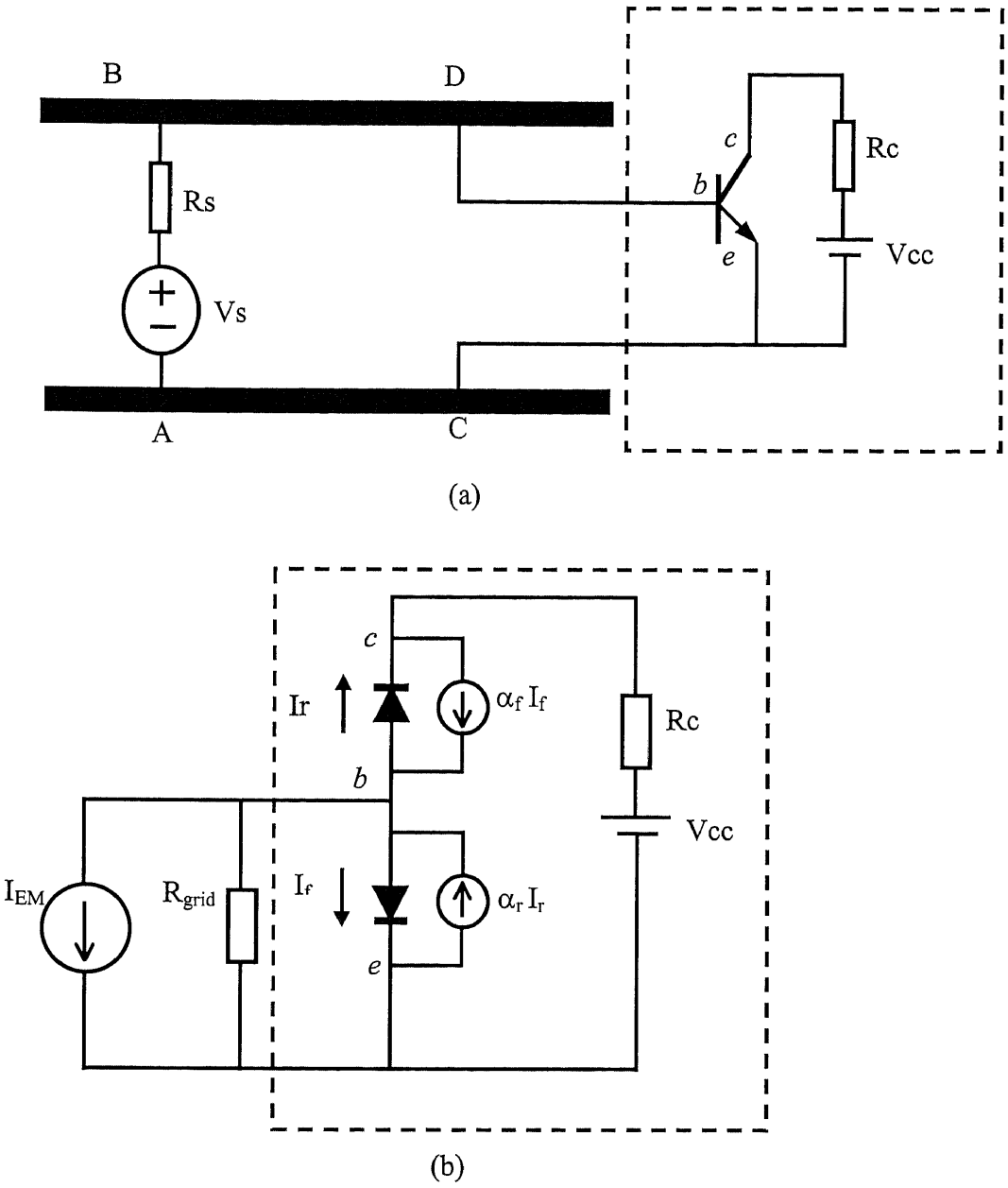

Figure 4.6 Bipolar juncture transistor load. (a) a hybrid system. (b) Ebers-Moll model of Bipolar jucture transistor and the co-simulation model.

$$I_f = I_0(e^{\frac{qV_{be}}{kT}} - 1) \tag{4.23}$$

$$I_r = I_0(e^{\frac{qV_{bc}}{kT}} - 1) \tag{4.24}$$

Given I_{EM}, the following equation set is solved by Newton-Raphson method to obtain all the currents and voltages at present time step:

$$I_{EM} = \frac{V_{be}}{R_{grid}} + (1-\alpha_f)I_0(e^{\frac{qV_{be}}{kT}} - 1) + (1-\alpha_r)I_0(e^{\frac{qV_{bc}}{kT}} - 1) \tag{4.25}$$

$$V_{cc} = V_{be} - V_{bc} - R_c(\alpha_f I_0(e^{\frac{qV_{be}}{kT}} - 1) - I_0(e^{\frac{qV_{bc}}{kT}} - 1)) \tag{4.26}$$

$$I_{lumped} = I_{be} = I_{known} - \frac{V_{be}}{R_{grid}} \tag{4.27}$$

The FDTD result shows perfect agreement with the SPICE result, as shown in Figure 4.7. Because of the high amplitude of the source voltage, the transistor works in saturation and cut-off regions alternatively. The result shows that the co-simulation handles the highly nonlinear circuit well. This is very important for high-speed digital system simulation.

4.5.4. Short Pulse Generator

Figure 4.8 shows a circuit for generating very narrow electric pulse from a sine wave. To test the multiple-cell field-circuit model, the transmission line has been filled with three dielectric layers. The lumped circuits are crossing multiple dielectric layers where the EM fields are not uniformly distributed.

Utilizing the phase difference of the voltage and current of an inductor and the strong non-linearity of a diode, very short pulse is generated when a sine wave propagates

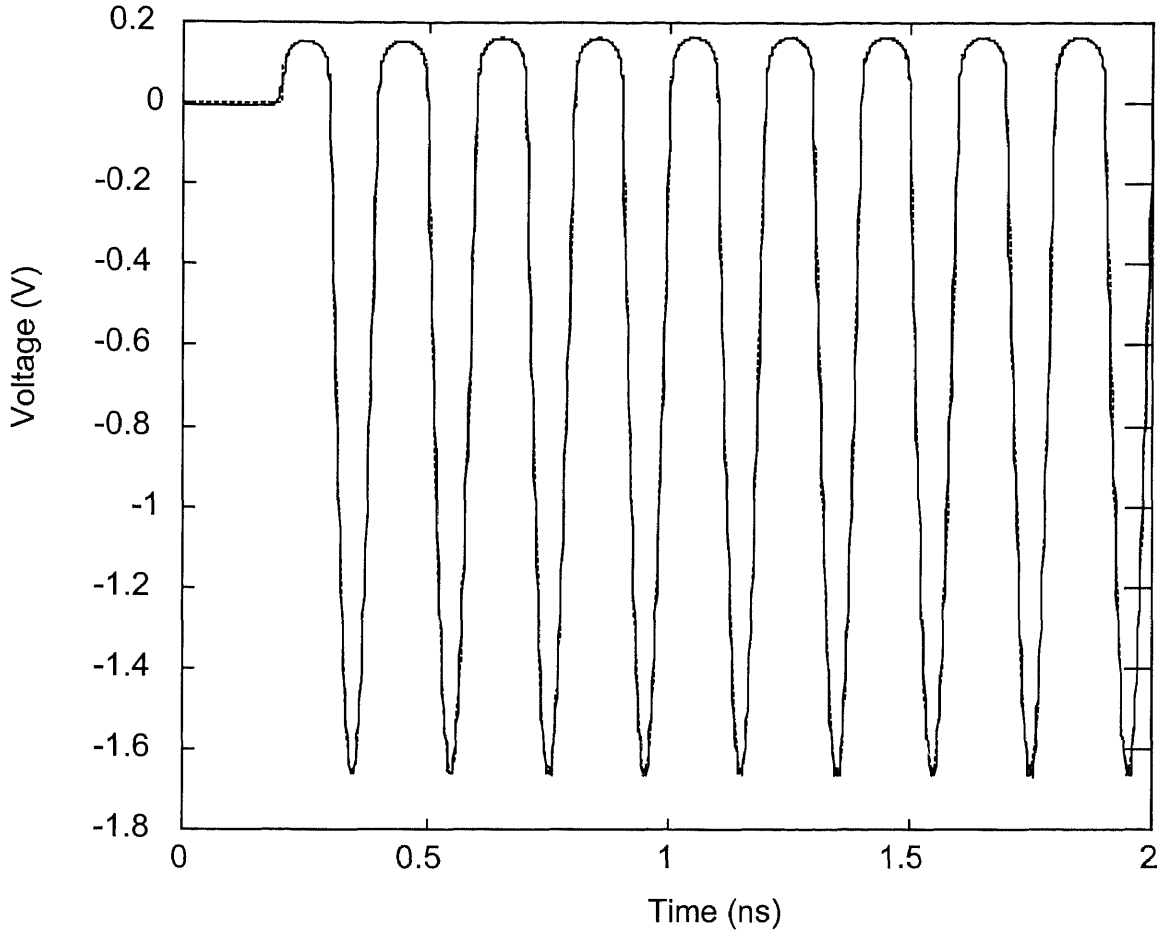

Figure 4.7 Test case 3: Voltage profile of BE junction of the transistor load shown in Figure 4.6.

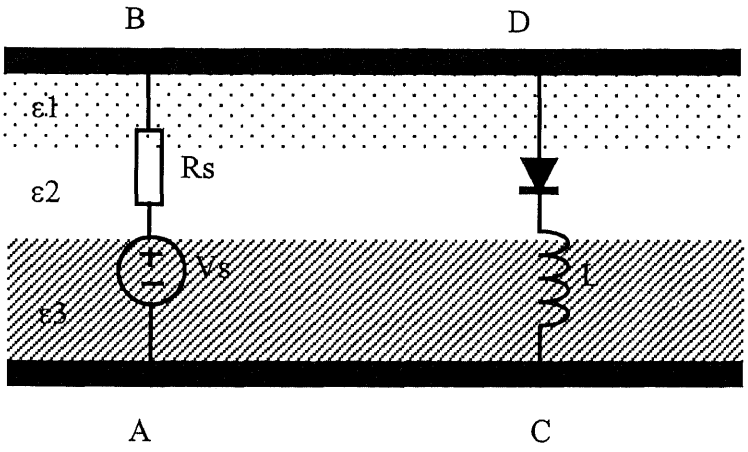

Figure 4.8 Circuit structure of a narrow pulse generator. $Vs=V_0\sin 2\pi ft$, $V_0=90V$, $f=200MHz$, $Rs=3\Omega$, $L=1\mu H$, $AB=8mm$, $BD=30mm$, $\varepsilon_1=2$, $\varepsilon_2=4$, $\varepsilon_3=20$. Schottky Diode parameters are $I_0=0.5mA$ and $T=298K$.

through the inductor and diode in series [Maas 1998]. The combination of high non-linearity, large signal magnitude and very short pulse would drive a standard LCA to divergence quickly. Figure 4.9 shows the result from our proposed field-circuit co-simulation model and demonstrates its stability in extremely nonlinear, large signal magnitude and very short pulse cases.

4.5.5. Diode Mixer

Mixer is one of the most important components in a wireless communication system. The design and simulation of mixers are not trivial. Current design methodologies of mixers are mostly based on circuit simulation method and in frequency domain [Kollberg 1984, Rizzoli and Neri 1991, Chew and Itoh 1996]. Conventional analog circuit simulators, using a frequency-domain harmonic balance method, cannot handle the phenomenon caused by the signal propagation, cross talk and other field effects. Higher operating frequency and smaller physical size of the electronic systems cause the field effects one of the dominating design considerations, therefore making mixer design and analysis much more difficult. The combination of high nonlinearity and associated field effects need a time-domain, full-wave technique for the analysis and design of mixers.

Naturally being a hybrid system, a mixer can be divided into a distributed system, made of a multiple-layered substrate transmission line in open space or packaging and open/shunt strip lines, and embedded lumped elements, like diode and LC filtering elements. Since the lumped current algorithm has been developed and expended for analyzing hybrid systems consisting of distributed systems and its embedded lumped elements, FDTD is used in the mixer designs [Chen et al 1997, Chen et al 1998].

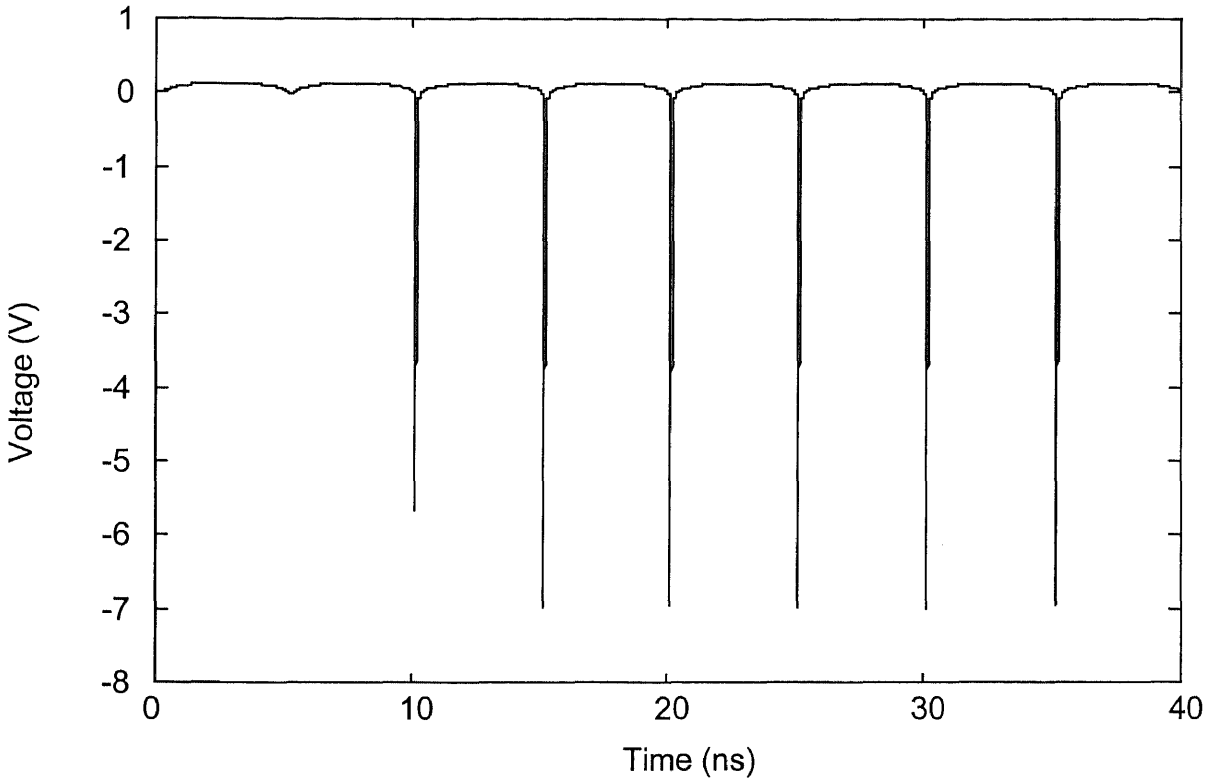

Figure 4.9 Voltage profile of the inductor shown in Figure 4.8 by co-simulation method

However the FDTD simulation of mixers mostly were based on single-cell lumped current formulation.

In this section, the field-circuit model is applied for simulating mixers, which include high nonlinear component and multiple-layer structures. Although the discussed mixer configurations are relatively simple compared with those practical ones, they cannot be easily simulated by other available frequency-domain design tools. Simulation results show that the field-circuit model has promising potential for the analysis of mixers and other high frequency EM systems.

The function of a mixer in transceiver circuits is to multiplex received radio frequency (RF) signal with a local oscillation (LO) signal to generate the intermediate frequency (IF) signal, which has the frequency equal to the frequency difference between those of LO and RF signals. Mixer structures used later are fairly simple and two-dimensional FDTD simulation results given here are for the demonstration purpose.

Figure 4.10 shows a diode mixer where RF and LO signals are combined together at a single input port. Both signals are mixed by a Schottky diode connected to a parallel-plate transmission line. Through a bandpass filter, IF signal is selected from the output signal spectrum. The bandpass filter is a standard 3 level filter and its passing frequency is set to be centered around IF frequency. The structure of the bandpass filter is shown in Figure 4.11, and it may not have been optimized for the best gain performance. The metal plate thickness of the transmission line is 0.001m with conductivity of 10^7 Ω/m.

The I-V relation of the Schottky diode used in the mixers is described by (4.22)

Using the field-circuit co-simulation briefly described in Sections 2 and 3, the simulation results for the mixer structure given in Figures 4.10 and 4.11, are shown in

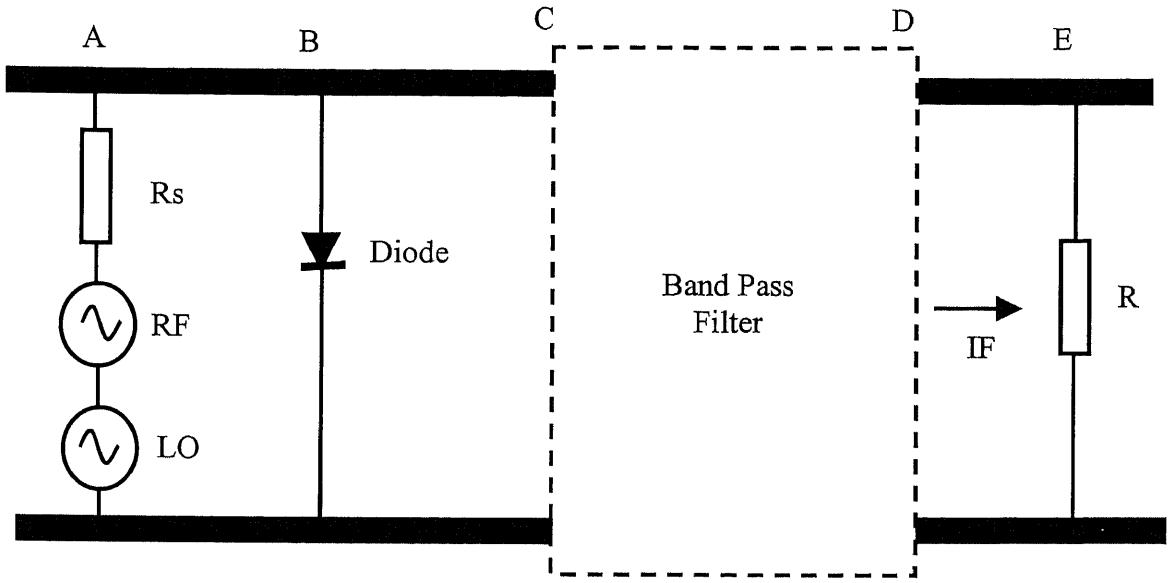

Figure 4.10 Illustration of a one-port mixer structure. AB=0.06m, BC=0.12m, CD=0.008m, DE=0.032m and Rs=Z0; LO signal parameters are f=10GHz, V0=10V; RF signal parameters are f=2GHz, V0=10V; Schottky diode parameters are I0=5mA, T=298K; Load R=Z0Ω.

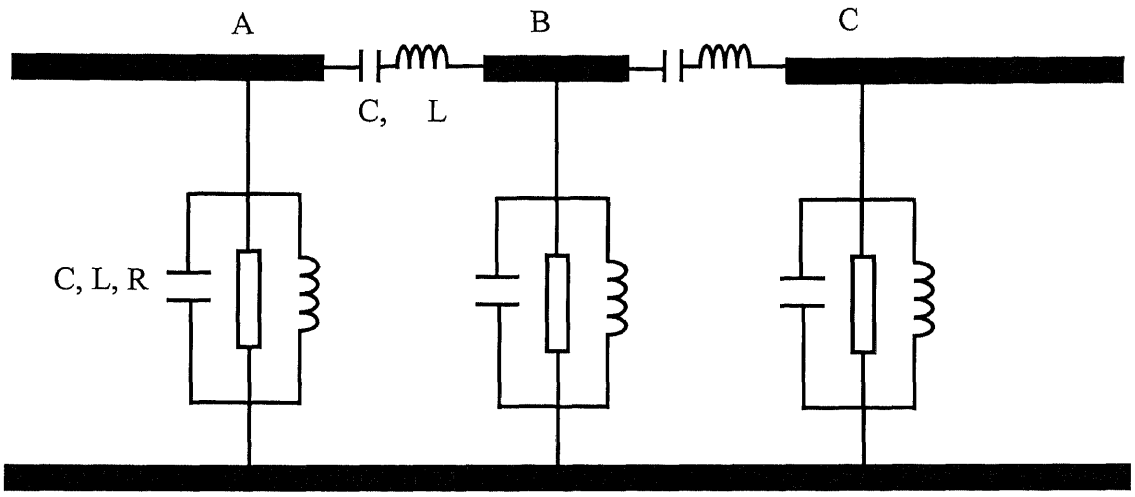

Figure 4.11 Illustration of a bandpass filter used in co-simulation

Figures 4.12 - 4.14. Figure 4.12 plots the transient voltage across the diode. The very close results from FDTD and SIPCE simulations indicate good accuracy of our field-circuit co-simulation model under large-signal condition. Figures 4.13 and 4.14 show the spectrum of the signal, before and after passing the bandpass filter respectively. Apparently the output voltage after the filter has the desired frequency component.

To test the feasibility of applying the field-circuit model to multiple-layered structures, a two port diode mixer configuration is simulated. As shown in Figure 4.15, the mixer is filled with three types of dielectric medium at different locations of the transmission line. The LO and RF signals (20GHz and 100GHz, respectively) are fed into the mixer from two different ports. A bandpass filter similar to that in Figure 4.11 is connected at the output port. Uniform FDTD cell size 0.1mm and time increment of 0.1667ps are used in the calculation. The simulation results of the mixer are shown in Figures 4.16 and 4.17, where both signal spectrums before and after the bandpass filter are given. IF signal (80Ghz) is obtained after the filter as desired.

Although the mixer structures here are relatively simplified, the simulation results, nonetheless, show that the field-circuit model is appropriate for analyzing mixers with more complicated structures. Using the field-circuit model in FDTD, multiple-layered structures can be simulated, with good accuracy and stability, without much additional computational cost.

The band pass filter used in this simulation is also a hybrid system, as shown in Figure 4.10. Actually, the whole system with many lumped elements is simulated by one time run. The number of the lumped elements does not influence the computational cost of FDTD. By the field-circuit co-simulation model, the FDTD simulation treats all the

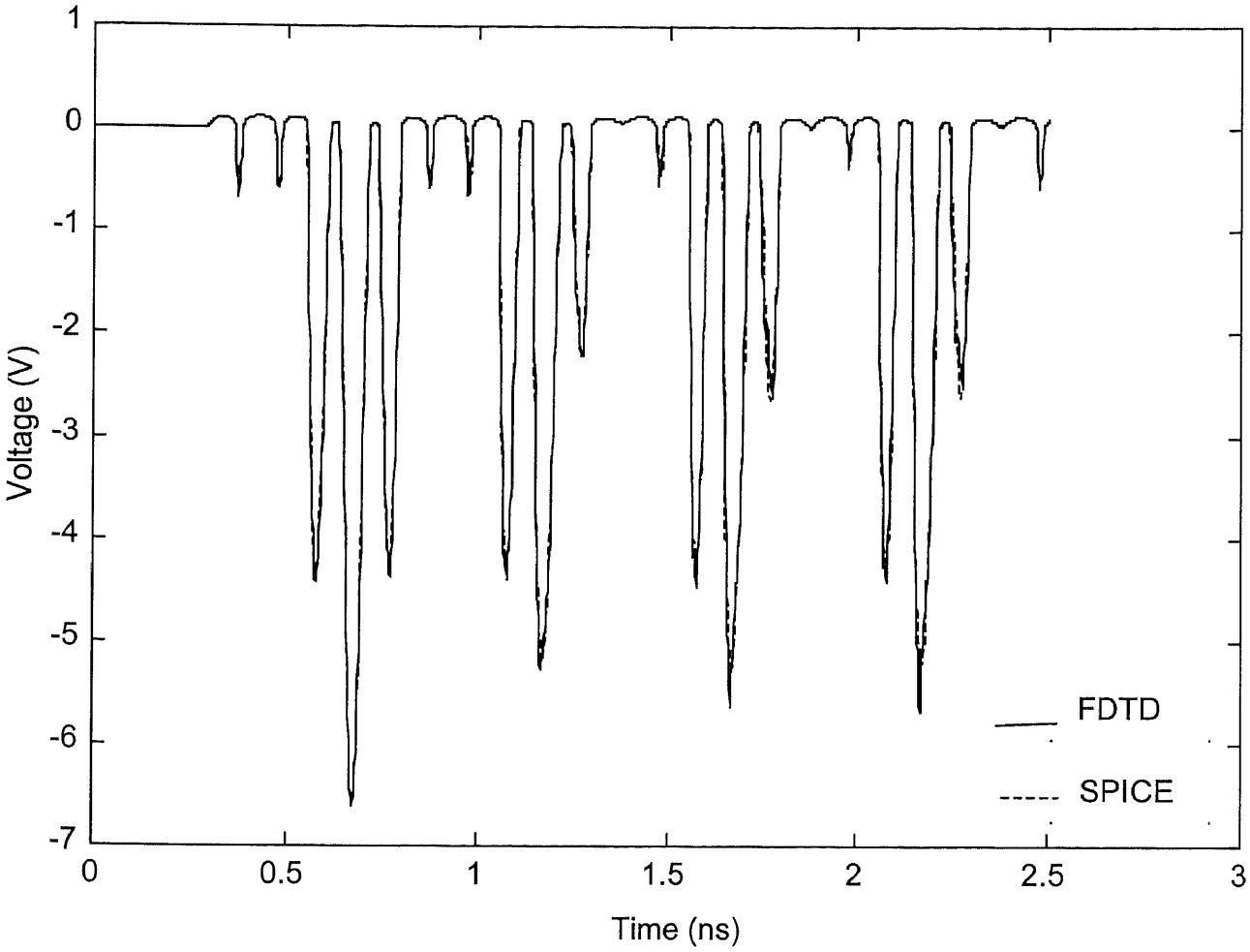

Figure 4.12 Simulation results of the mixer, shown in Figure 4.10. Comparison of simulation results: Diode voltages from FDTD field-circuit model (solid line) and SPICE (dashed line) are both plotted.

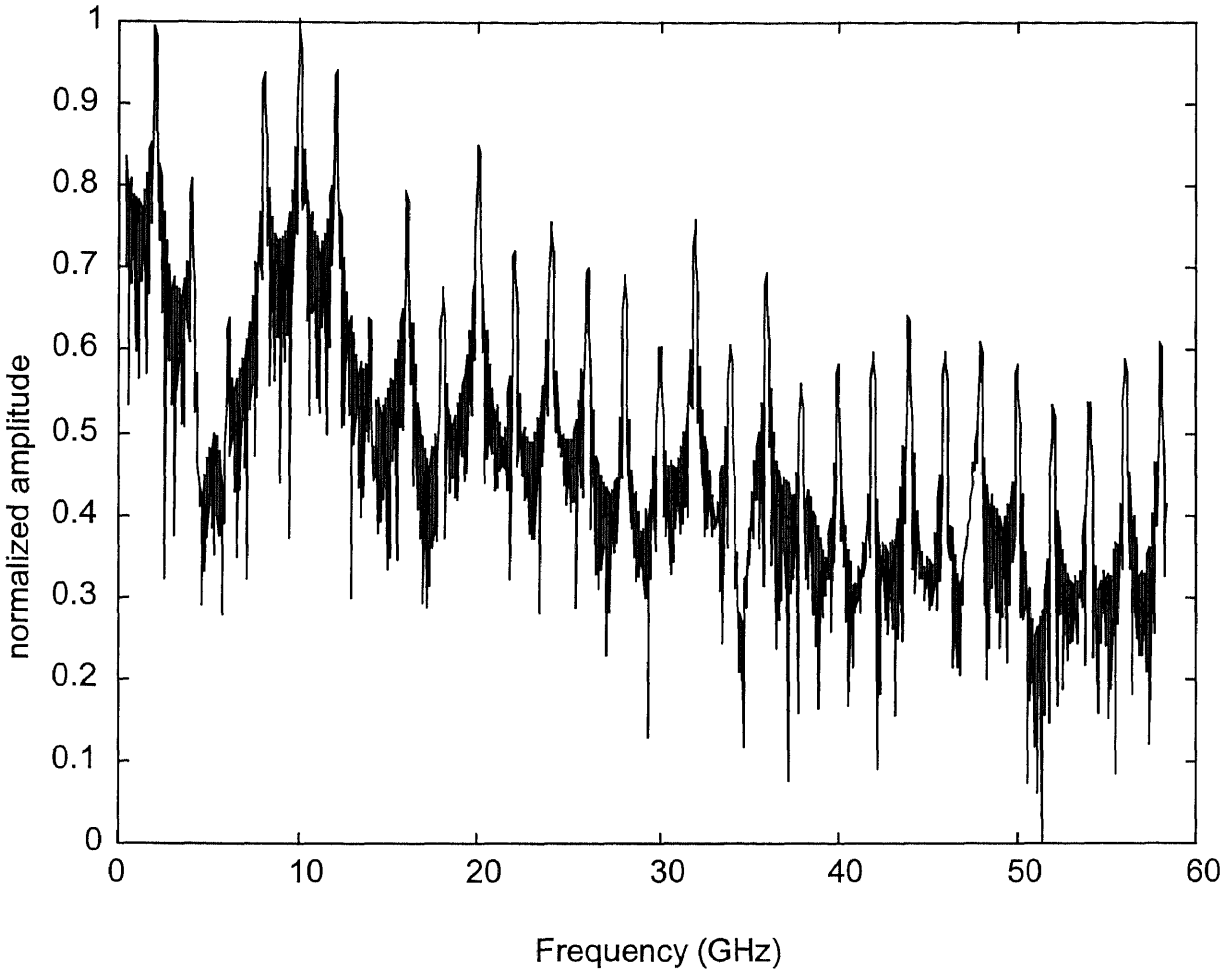

Figure 4.13 Simulation results of the mixer shown in Figure 4.10. Spectrum of voltage of the diode (before filter) obtained from FDTD field-circuit co-simulation model

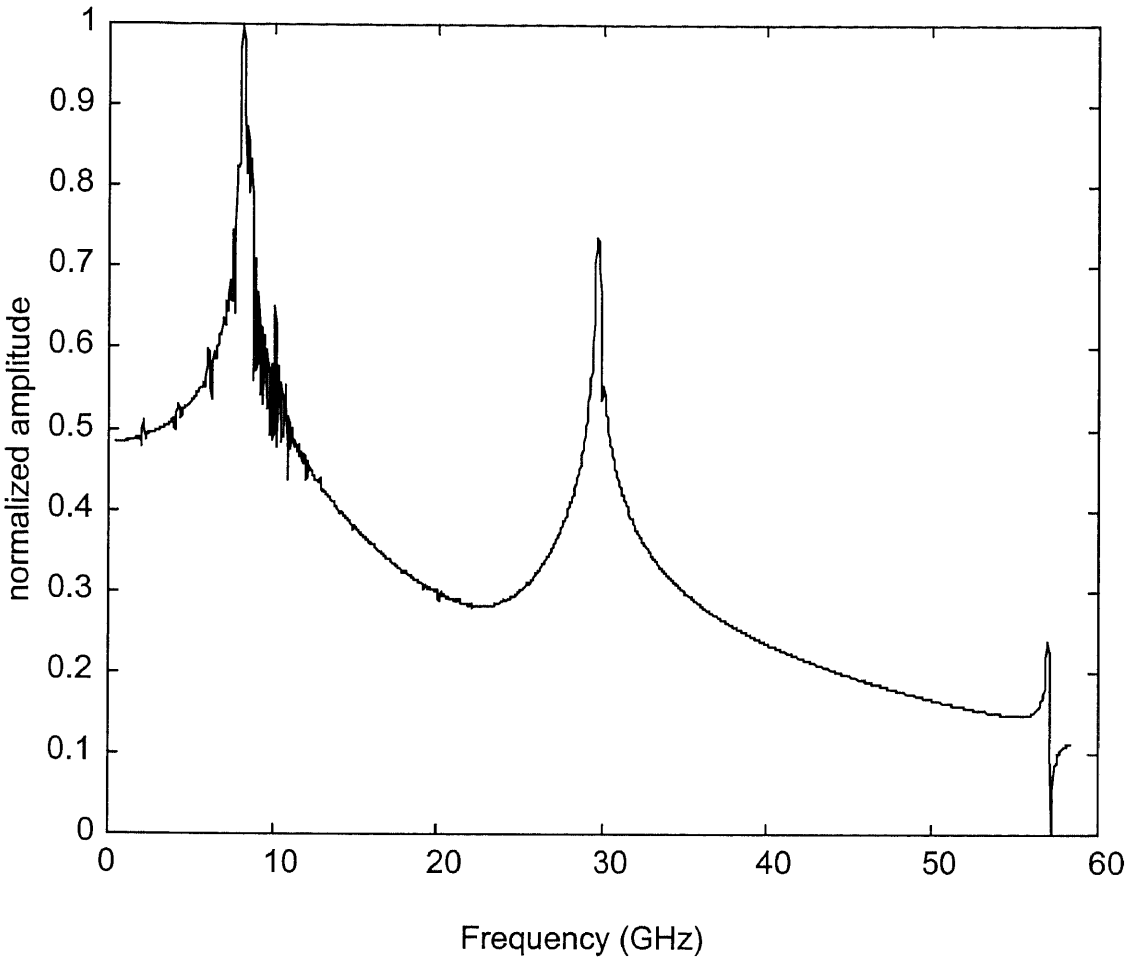

Figure 4.14 Simulation results of the mixer shown in Figure 4.10. Spectrum of voltage of the diode (after filter) obtained from FDTD field-circuit co-simulation model

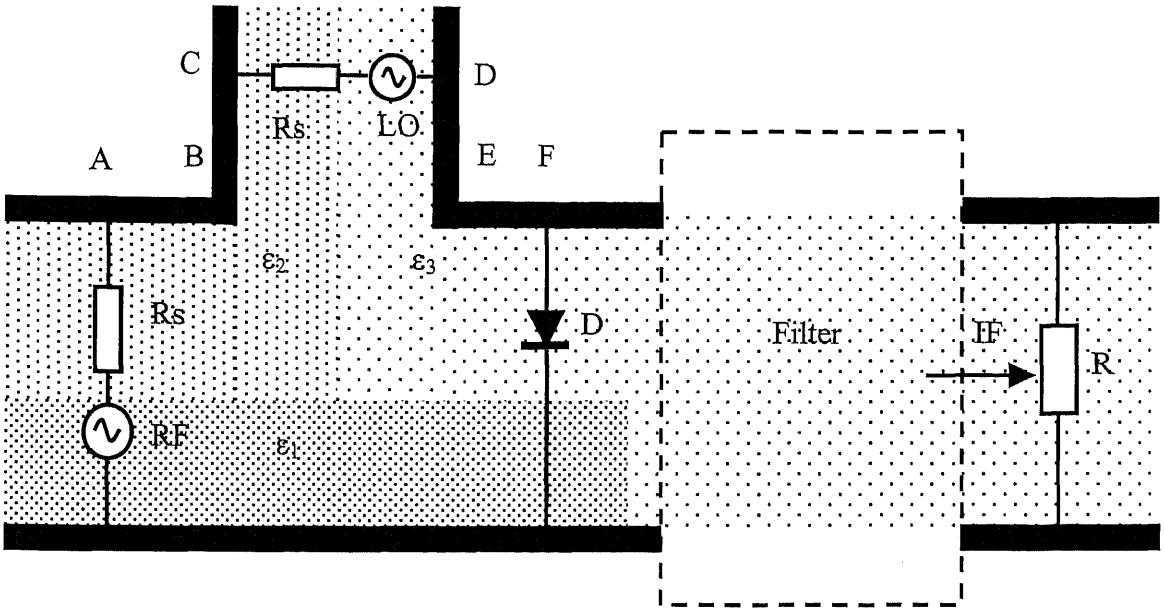

Figure 4.15 Illustration of a two-port input mixer structure with multiple-dielectric layers. AB=0.003m, BC=0.002m, CD=0.0008m, EF=0.002m. ε1=20, ε2=4, ε3=2; LO signal parameters are f=100GHz, V0=5V, Rs=300Ω; RF signal parameters are f=20GHz, V0=5V, Rs=300Ω; R=266Ω.

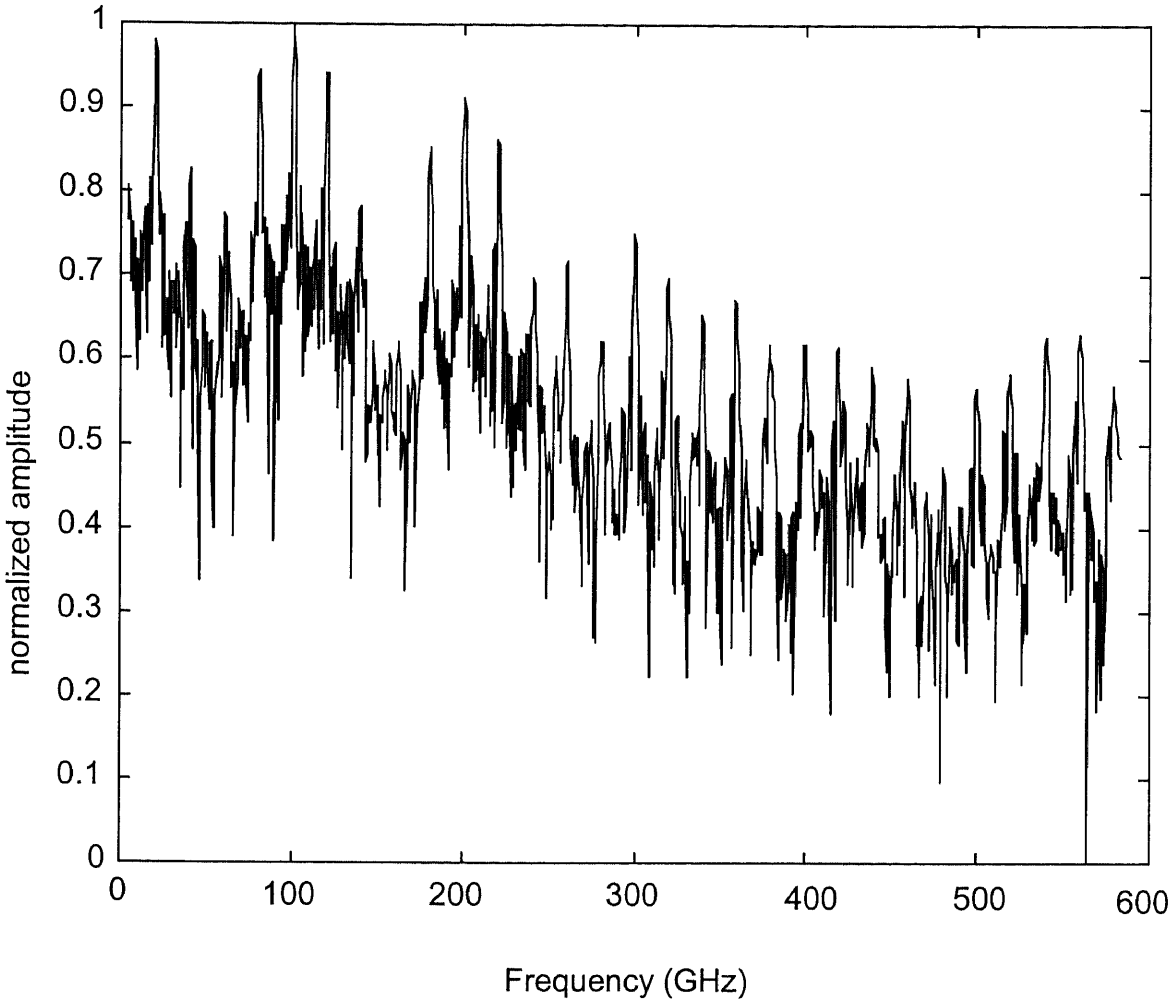

Figure 4.16 FDTD simulation results for the mixer shown in Figure 4.15. Spectrum of the mixing diode voltage.

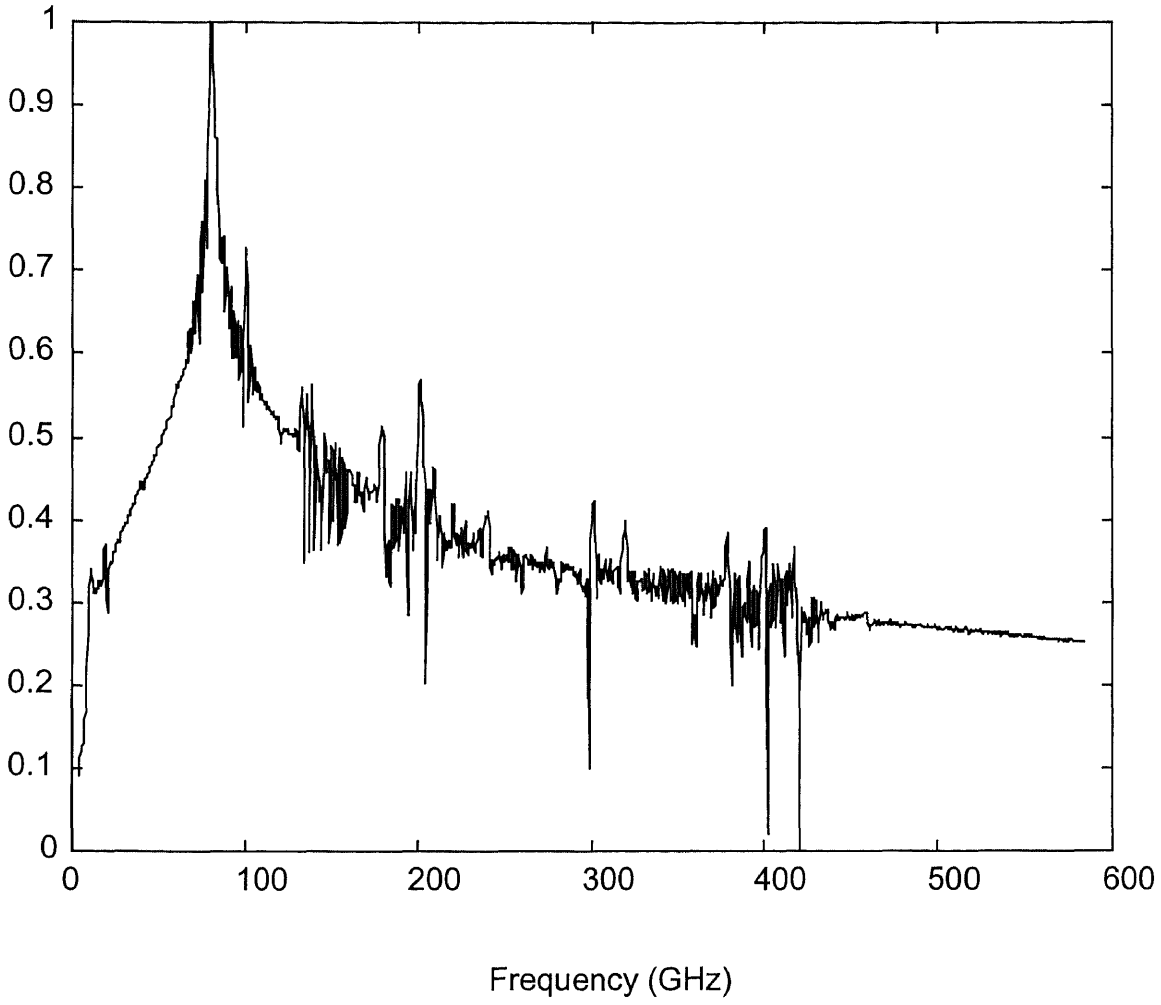

Figure 4.17 FDTD simulation results for the mixer shown in Figure 4.15. Spectrum of the load resistor voltage (after bandpass filter).

lumped elements in the same way. This benefits to the implementation of this model for more complicated structures. Future promising application for such a technique in mixers and other high-speed electronic systems is anticipated.

4.6. Conclusion

This chapter demonstrates a field-circuit co-simulation model to solve a hybrid EM system with lumped elements embedded in it. The lumped current algorithm provides an opportunity to simulate a hybrid EM system that consists of lumped elements and distributed structures. In the system, field effects and the interaction between lumped elements and the EM field have significant influence on the characteristics of the system. In other words, the wave propagation cannot be ignored in the simulation of such systems.

In this chapter, a general multiple-cell FDTD formulation is proposed to interface FDTD with an analog circuit simulator by a highly stable field-circuit co-simulation model. Using the model, any hybrid system simulation can be divided into two parts, the EM fields solved by FDTD and current/voltage solutions obtained from the analog circuit solver. These two systems have a simple interface for field and circuit interaction. From the FDTD points of view, a lumped element is included by an additional current term in the magnetic field loop integration; from the circuit simulation points of view, the distributed structure filled by the FDTD grid is treated as a couple of equivalent lumped elements. Numerical features in the formulation, like de-coupling of field and circuit simulation, and implicit expression for lumped current in time, contribute to the algorithm's supreme stability even under very large signal nonlinear situation and keep

the same computational load as that in conventional FDTD. The proposed technique provides the flexibility for extending circuit simulator to include a field-solver module or vise versa; it makes overall co-simulation of complicated hybrid systems, like active array antennas and mixers, possible.

CHAPTER 5

EXTENSION OF PML ABSORBING BOUNDARY CONDITIONS

5.1. Introduction

A common situation of EM system simulation is that only part of the system is simulated or within the computational capability. Therefore the numerical grid has to be truncated into a limited FDTD computational domain. This causes numerical considerations of simulating an outgoing wave without artificial reflections at the truncated boundaries. These boundary conditions are called absorbing boundary conditions (ABCs).

For an open space problem where the simulation target is surrounded by air, absorbing boundary conditions [Bayliss 1980, Mur 1981, Berenger 1994, Katz et al 1994] have been developed to confine the FDTD computational domain. Berenger's PML method [Berenger 1994 1996] has been considered as the most accurate method. Compared to other approaches, PML has stronger ability to absorb the EM waves in a wide frequency range and incident angles. This property is necessary for modeling EM waves in high frequency nonlinear circuits where dispersion and multi-mode waves are common phenomena.

When microwave circuits with dielectric and metal layers are modeled, these materials often extend into a boundary, meaning they are infinite in that direction as the simulation concerns. PML boundary conditions have been modified to take such numerical considerations. Reuter et al [1994] utilized PML in two-dimensional FDTD to simulate the parallel-plate waveguide with layered dielectric media and showed that the reflection coefficient was under –75dB. As a widely used circuit building block,

microstrip line has been intensively analyzed by three-dimensional FDTD simulation [Housmand, Itoh and Piket-May 1998]. One important issue about microstrip line FDTD modeling is again how to truncate the microstrip line with lowest possible reflection. Because of the inhomogeneous nature of the PML layer at the presence of the microstrip line, the interface between different media has to be treated carefully.

Before the publication of PML, Mur's absorbing boundary conditions [Mur 1988] had been extended into microstrip line model [Sheen 1990, Fang 1989]. Then PML technique was used to model waveguide [Bahr et al 1995] and multilayered structure [Reuter et al 1995, Verdu et al 1995], all in 3D FDTD analyses. PML shows much better performance than Mur's ABCs but it is much more complicated. In [Reuter et al 1995, Verdu et al 1995], in order to model the interface of the different layers, dielectric permittivity of PML has to be treated differently in different directions depending on the PML sub-component of the electric field to be calculated. These additional dependencies made the PML formulation more complicated and not easy to be implemented.

It is highly desired to formulate a general approach that can implement PML to inhomogeneous media. This chapter presents such a formulation to model PML for multi-layer structure in non-uniform FDTD grid. Instead of differential equation forms, the discretization of PML equations start from their integral forms, which was used in FDTD equations of non-uniform FDTD grid to handle the boundary conditions between different media layers. Then these equations are discretized by the central finite difference scheme. By this approach, no special numerical treatment is necessary to handle the boundary conditions at the dielectric-dielectric and conductor-dielectric interfaces inside PML media. In FDTD simulation, especially the analysis of multi-layer

structure, non-uniform grid is commonly used to improve the efficiency and accuracy of the simulation for complicated circuit structures. As another advantage of the approach in this chapter, non-uniform grid is seamlessly handled by the proposed formulation.

In [Berenger 1996], geometric loss profile is utilized in 3D FDTD analysis to deal with the inhomogeneous boundary. The PML condition with geometric loss profile has better performance than the quadratic profile conventionally used. In order to apply the geometry profile to non-uniform FDTD grid, an extended PML layer parameter set of geometric profile for PML loss is also presented.

5.2. Generation of PML Layers for Inhomogeneous Boundary

The Berenger's PML absorbing boundary conditions split each electric or magnetic component into two sub-components, which satisfy the equations (2.46) - (2.57).

Generally speaking, regardless of the frequencies and angles of the incident waves, the EM waves propagate through the PML layers with exponential decay and generate no reflection if the following conditions are satisfied:

$$\frac{\sigma_x}{\varepsilon} = \frac{\sigma_x^*}{\mu}, \frac{\sigma_y}{\varepsilon} = \frac{\sigma_y^*}{\mu}, \frac{\sigma_z}{\varepsilon} = \frac{\sigma_z^*}{\mu} \tag{5.1}$$

The PML layer generates little numerical reflection at the boundary, but the standard formulation has to be extended to work at some situations other than the homogeneous media and uniform FDTD grid. For example, when a multi-layer microstrip line extends into one of the FDTD grid boundaries, some modifications have to be made to the PML equations to take different media into consideration.

Without losing generality, we assume that our FDTD cells are small enough to describe the geometry of an EM system. In other words, the medium within one cell is

homogeneous. In many EM systems, the lossless linear electric media and the metal with very high conductivity are widely used. In our consideration, the media are limited to those media mentioned above.

First, metallic boundary cells are considered. Because lossy media considered are metal with very large conductivity, they are treated as quasi-PEC. Under this quasi-PEC condition, if a Yee cell on boundary has non-zero conductivity, in any one of its adjacent PML cell and the PML cells along the line of the two cells, the electrical loss values in three directions, σ_x σ_y, and σ_z, are set to be equal to the conductivity of the boundary Yee cell. The magnetic loss values in three directions, σ^*_x σ^*_y, and σ^*_z, are set to be zero.

To stretch the non-metallic cells into the PML, the permittivity and permeability in the PML are kept the same distribution as that of the cell before reaching the boundary. In this arrangement, each PML cell has only one permittivity value instead of three values as in [Reuter et al 1995, Verdu et al 1995].

Generally speaking, in this scheme, the parameters in PML cells, except the specific parameters for PML cells, keep the same distribution as those in Yee cells. This arrangement is used to simplify the construction of the PML layers. Later we will see that this simplification benefits from the utilization of the integral PML equations to generate the discretized PML equation forms.

Taking sub-components E_{yx} and H_{yx} of an EM field as examples to demonstrate the construction of the electrical loss and magnetic loss for the non-metal cell. In this case, σ_x and σ_x^* satisfy (5.2) and σ_y, σ_y^*, σ_z and σ_z^* are set to be zero. Figure 5.1 shows the

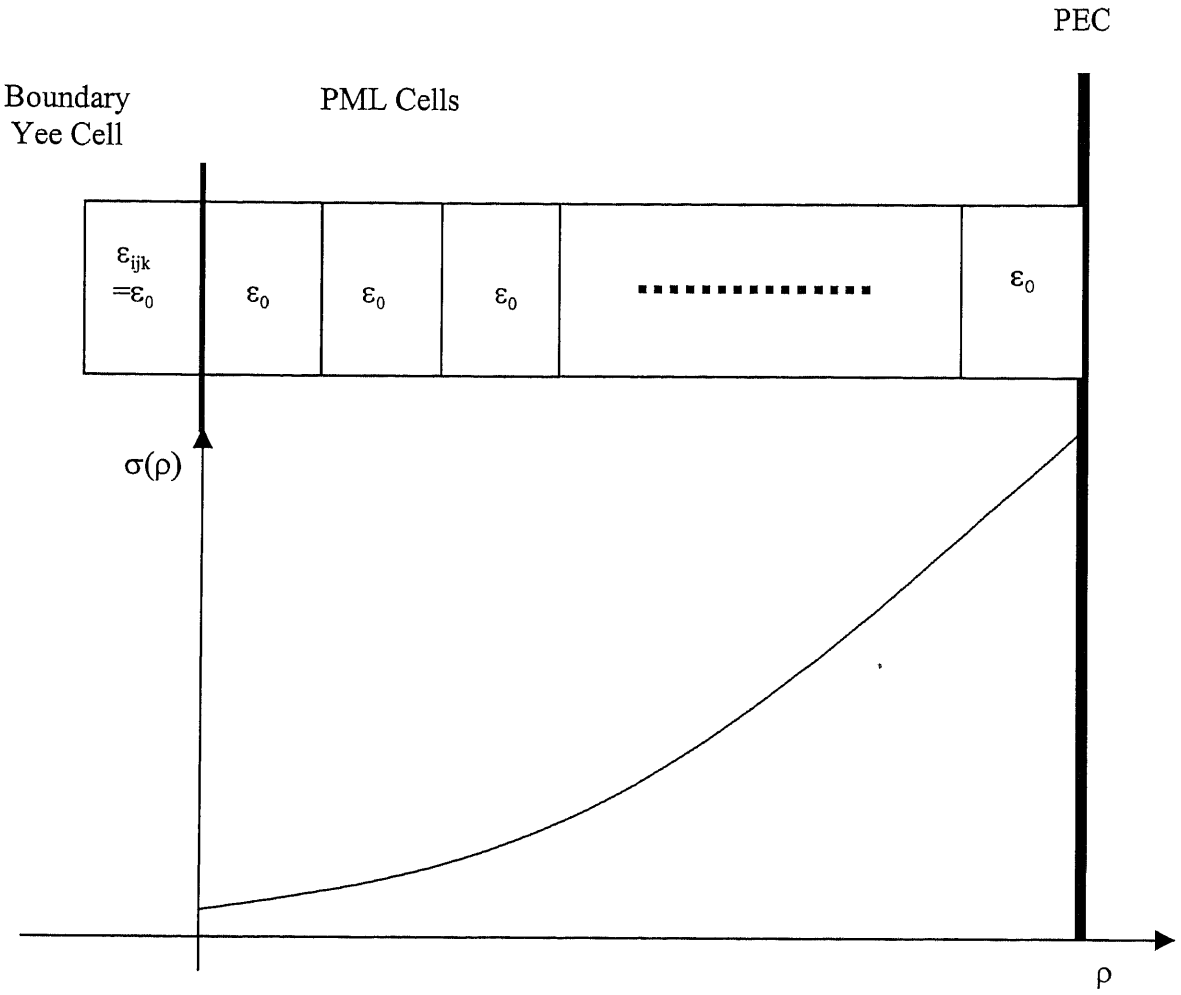

Figure 5.1 The construction of the electric loss of PML cells

construction of the electric loss of PML cells. In Figure 5.1, the permittivity of all PML cells is ε_0 and the loss of a PML cell is a function of distance from the cell to its corresponding boundary Yee cell. This is called the PML loss profile, $\sigma(\rho)$.

Because of the discretization error, the perfectly matching performance of PML cannot be reached numerically. The error is smaller if the electrical losses of two adjacent layers are closer. Thus in order to reduce the numerical error, the smaller electrical loss value is better. On the other hand, in order to absorb the outgoing wave within a finite number of PML layers, the electrical loss has to reach a certain amount of value. Therefore, with the consideration of both the numerical error and absorbing performance, $\sigma(\rho)$ has to be an increasing function of ρ.

The relation of σ and ρ can be many profiles, such as linear, quadratic and geometric. The geometric profile demonstrates higher performance than others do [Berenger 1996]. Let

$$\sigma(\rho) = \sigma_0 (g)^{\frac{\rho}{d}} \tag{5.3}$$

where g is the scaling factor, σ_0 is the electric loss at the interface between PML and Yee cells, and d is the cell size of PML cells.

The electrical loss at the grid point is implemented as the average value in the cell around the index position

$$\sigma_x(L, j, k) = \frac{\varepsilon_{rijk}}{dx} \int_{\rho(L)-dx/2}^{\rho(L)+dx/2} \sigma(x) dx \tag{5.4}$$

where L is the distance from the current point to the interface between Yee cells and PML cells in x direction, L=0,1/2,1,3/2.... Not that in (5.4) the different media are

considered by taking the permitivities as a scaling constant of the electric loss of the PML cell.

Substitute (5.3) into (5.4), we have

$$\sigma_x(0,j,k) = \varepsilon_{rijk}\sigma_0 \frac{\sqrt{g}-1}{\ln g} \tag{5.5}$$

$$\sigma_x(L,j,k) = \varepsilon_{rijk}\sigma_0 \frac{g-1}{\sqrt{g}\ln g} g^L, \quad L=1/2,\ 1,\ 2/3,\ldots. \tag{5.6}$$

The corresponding σ_x^* can be obtained from (5.2) to keep the PML's perfectly matching property.

Thus in order to construct a PML media in one direction, three parameters have to be decided, N, the number of the PML layers, σ_0, the initial electrical loss, and g, the scaling factor of the geometric profile.

Although there are several publications discussing the systematic construction of the PML layers [Berenger 1997, Fang 1996], the implementations of all kinds of PML are empirical. In this dissertation, according to our experience, some suggestions about the essential consideration of PML parameters are in the following.

1. N normally depends on the accuracy limit one wants to reach. If one is looking for high absorption effect, N is normally chosen higher value, such as 12 or 16; otherwise, N could be 4 or 8. N also depends on the distance from the discontinuity to the boundary. If the distance is very close and there are many evanescent waves around the boundary, N should be larger. If one cannot obtain a good absorption with a larger N, increasing the distance would be a good solution.
2. σ_0 is the electrical loss at the interface of the dielectric media and PML media. Intuitively consider the PML layer as a lossy medium. A higher frequency EM

wave penetrates more into a lossy medium than a lower frequency one does. Thus the performance of a PML layer is decided by its absorption to low frequency waves. The media with lower conductivity would allow more EM wave to pass through it than that with higher conductivity does. Therefore in order to allow more low frequency EM wave to penetrate into PML media, σ_0 should be as low as possible. However, it has to be a certain value to get the EM wave absorbed in PML media. Therefore, the σ_0 value depends on the lowest frequency in the simulation, which is decided by the total run time of the simulation. The conclusion is that σ_0 is decided by the total run time.

3. g is the increasing rate of the electric loss of PML media. The geometric profile has the property that the electric loss of any adjacent layers has the same ratio everywhere in the PML media. According to the observation in [Berenger 1996], a large value of g generates oscillations heavily and it must be lower than a certain value, which is related to other parameters empirically. Although in [Berenger 1996] there is reference data of g in some situations, it is based on two-dimensional FDTD simulations and has to be adjusted to fit to three-dimensional simulations. Therefore, in order to validate g value in a three-dimensional FDTD simulation, numerical experiments have to be done to adjust the g value. Actually, with the more reference in hand, g value can be decided within one or two numerical experiments. A systematic procedure to optimize g is under investigation.

The above discussions can be applied to both uniform and non-uniform FDTD grids. Theoretically, our PML formulation can handle the non-uniform cell size in PML media.

However the PML performance under the non-uniform grid is not established and may cause additional reflection or instability. In this dissertation, the cell sizes in one direction, in which PML has absorbing function, are set to be uniform and the cell sizes in other two directions, in which PML does not have absorbing function, are decided by the cell sizes in the FDTD grid. Figure 5.2 is an example in two-dimensional cases.

In Figure 5.2, the cell sizes of PML cells at different boundary locations vary according to cell sizes of normal Yee cells adjacent to them. Because the cell sizes of Yee cells are nonuniform, it is possible that the cell sizes in the PML layers are different in different boundary locations. Without losing generality, assume that the numbers of PML layers in all six outer boundaries are different. The non-uniform cell sizes at each boundary cause different amount of reflections because the decay of the EM waves caused by the PML media is related to the distance in this medium traveled by the waves. Also from our numerical experiences, g is sensitive to the cell size of the boundary and it needs to be adjusted according to the cell size and other parameters, such as N and σ_0. Thus, in order to get good absorption at all boundaries, different sets of g, σ_0, and N at different boundary locations have to be defined. There are 6 sets including totally 18 parameters to be defined for 6 PML boundaries in 3D FDTD computational domain, i. e.,

g_{x-}, σ_{0x-}, and Nx- for the x- boundary,

g_{x+}, σ_{0x+}, and Nx+ for the x+ boundary,

g_{y-}, σ_{0y-}, and Ny- for the y- boundary,

g_{y-}, σ_{0y+}, and Ny+ for the y+ boundary,

g_{z-}, σ_{0z+}, and Nz- for the z- boundary, and

g_{z-}, σ_{0z-}, and Nz+ for the z+ boundary, respectively.

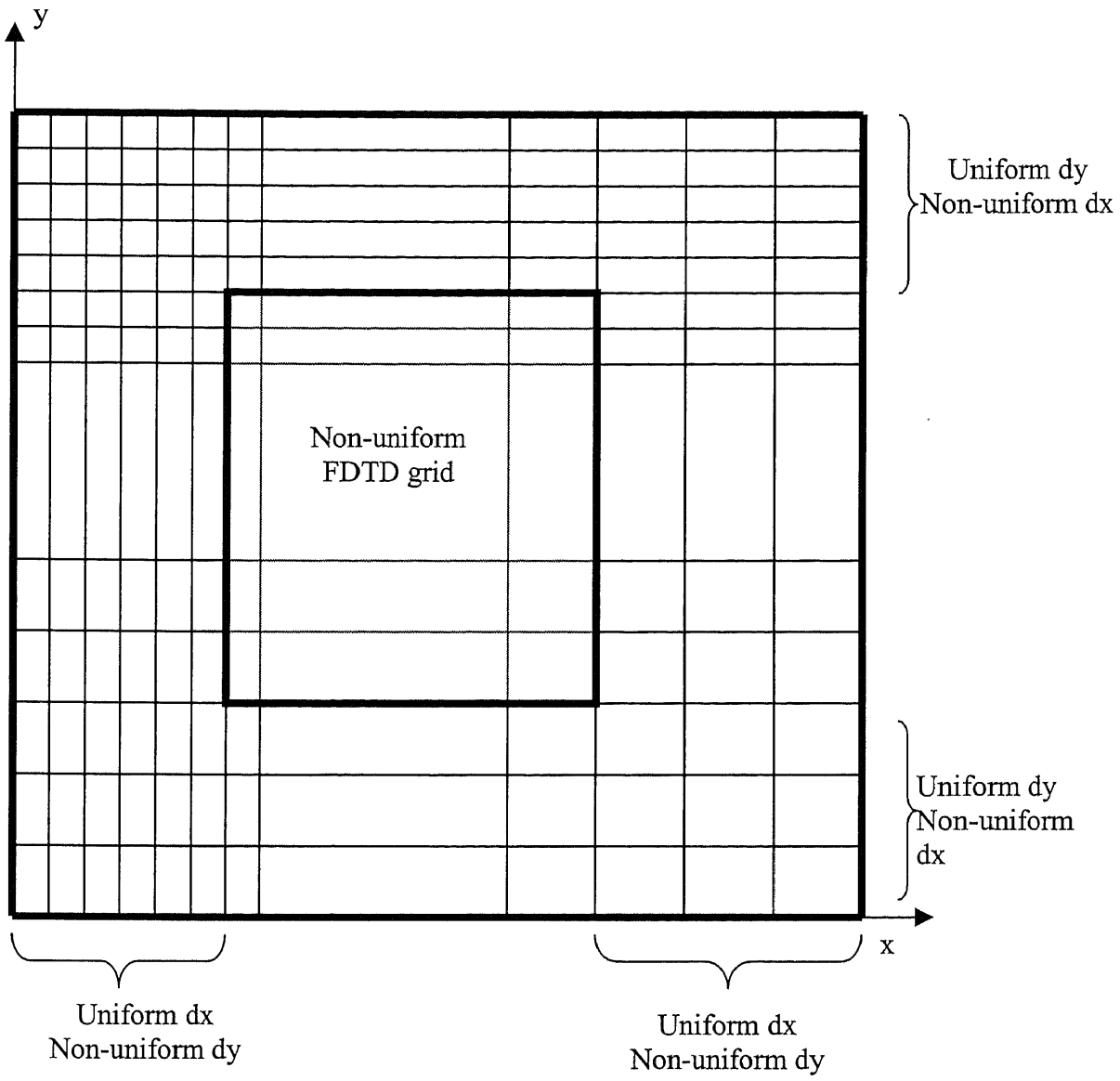

Figure 5.2 PML grid for non-uniform FDTD grid

Now, the PML media for the non-uniform FDTD grid are constructed. The optimal parameter set of g and σ_0, and the number of the PML layers for more accurate and efficient three-dimensional FDTD simulation depends on the establishment of the dispersion relation of the PML media with the geometric loss profile. The inhomogeneous media made this problem more difficult. Although this problem is not discussed in this dissertation, it is raised here as an important and interesting issue for the future research.

With this PML construction, it is flexible to choose the PML parameters in FDTD model files. For example, in many circuits, there is a metal ground assumed to extend to the infinity. For the boundary connecting to the metal ground, we need define only the PML layer number to be zero because the ground shields any EM field in the boundary. This arrangement reduces our computational cost. In the place that the media are smooth or homogeneous, we can consider using a smaller number of PML layers. In the places that the boundary is complicated, more PML layers can be used to improve the accuracy.

5.3. Derivation of PML Equations

As mentioned in Chapter 2, an integral form of Maxwell's equation is appropriate to derive the FDTD equations for inhomogeneous media. In the inhomogeneous PML media, we take the advantage of integral PML equation forms to derive our PML discrete equations.

Rewrite equation (5.1.1) for the inhomogeneous PML boundary in an integral form

$$\iint_S (\varepsilon \frac{\partial E_{yx}}{\partial t} + \sigma_x E_{yx}) ds = -\iint_S \frac{\partial H_z}{\partial x} ds = -\oint_C H_z dl \tag{5.7}$$

The surface integral area in (5.7) is the rectangular region inside the loop C of Figure 5.3.

By the same method, other PML equations can be written in the following

$$\iint_S (\varepsilon \frac{\partial E_{yz}}{\partial t} + \sigma_z E_{yz}) ds = \oint_C H_x dl \tag{5.8}$$

$$\iint_S (\varepsilon \frac{\partial E_{xy}}{\partial t} + \sigma_y E_{xy}) ds = \oint_C H_z dl \tag{5.9}$$

$$\iint_S (\varepsilon \frac{\partial E_{xz}}{\partial t} + \sigma_z E_{xz}) ds = -\oint_C H_y dl \tag{5.10}$$

$$\iint_S (\varepsilon \frac{\partial E_{zx}}{\partial t} + \sigma_x E_{zx}) ds = \oint_C H_y dl \tag{5.11}$$

$$\iint_S (\varepsilon \frac{\partial E_{zy}}{\partial t} + \sigma_y E_{zy}) ds = -\oint_C H_x dl \tag{5.12}$$

$$\iint_S (\mu \frac{\partial H_{xy}}{\partial t} + \sigma_y^* H_{xy}) ds = -\oint_C E_z dl \tag{5.13}$$

$$\iint_S (\mu \frac{\partial H_{xz}}{\partial t} + \sigma_z^* H_{xz}) ds = \oint_C E_y dl \tag{5.14}$$

$$\iint_S (\mu \frac{\partial H_{yx}}{\partial t} + \sigma_x^* H_{yx}) ds = \oint_C E_z dl \tag{5.15}$$

$$\iint_S (\mu \frac{\partial H_{yz}}{\partial t} + \sigma_z^* H_{yz}) ds = -\oint_C E_x dl \tag{5.16}$$

$$\iint_S (\mu \frac{\partial H_{zx}}{\partial t} + \sigma_x^* H_{zx}) ds = -\oint_C E_y dl \tag{5.17}$$

$$\iint_S (\mu \frac{\partial H_{zy}}{\partial t} + \sigma_y^* H_{zy}) ds = \oint_C E_x dl \tag{5.18}$$

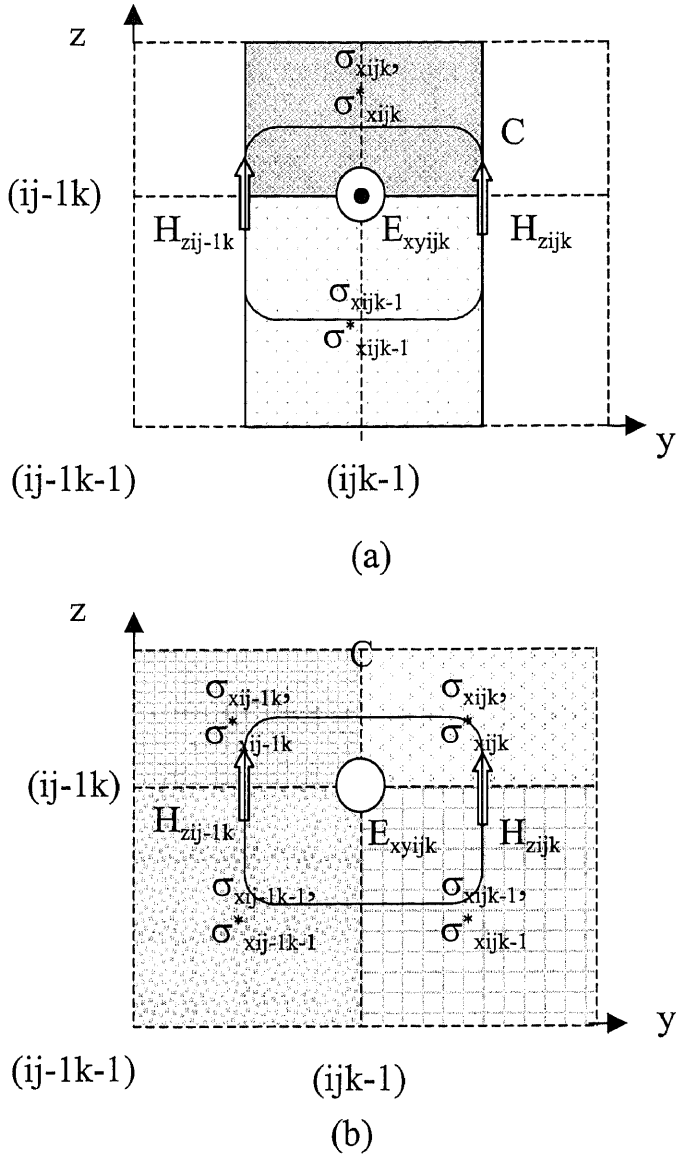

Figure 5.3 Discretization scheme of PML equations. (a) EM subcomponent locates inside its corresponding PML layers, (b) EM subcomponent does not locates inside its corresponding PML layers.

Note that S and C in the above equations are different in the equations from (5.7) to (5.18), but are defined in the same manner as shown in Figure 5.3.

As an example, the FDTD discretization form of (5.7) is derived to show the implementation of the integral PML equation form. Rewrite (5.7) in a discretized form

$$\iint_S (\varepsilon \frac{E_{yxijk}^{n+1} - E_{yxijk}^{n}}{dt} + \sigma_x \frac{E_{yxijk}^{n+1} + E_{yxijk}^{n}}{2}) ds = -\oint_C H_z^{n+1/2} dl \tag{5.19}$$

in which $E_{yxijk}^{n+1/2} = \frac{E_{yxijk}^{n+1} + E_{yxijk}^{n}}{2}$ is used.

In Figure 5.3, the electric field inside surface S is assumed to be uniform, the boundary media are inhomogeneous, and different PML electric or magnetic loss is loaded as mentioned previously. Considering carefully the PML loss of dielectric media defined in (5.5) and (5.6) and the PML loss of the conductive media, (5.19) has to be expanded according to two cases shown in Figure 5.3 (a) and (b), respectively.

Figure 5.3 (a) shows cells inside the PML media in x direction. The electric loss is defined in the x-index position and it changes in different y-position because of the direct extension of inhomogeneous media from the FDTD grid region to PML region. In this case, (5.19) can be expanded as

$$E_{yxijk}^{n+1} = \frac{\frac{\eta_{av}}{dt} - \frac{\varphi_{xav}}{2}}{\frac{\eta_{av}}{dt} + \frac{\varphi_{xav}}{2}} E_{yxijk}^{n} - \frac{(dz_k + dz_{k-1})/2}{\frac{\eta_{av}}{dt} + \frac{\varphi_{xav}}{2}} (H_{zijk}^{n+1/2} - H_{zi-1jk}^{n+1/2}) \tag{5.20}$$

where

$$\eta_{av} = \frac{\varepsilon_{ijk} dx_i dz_k + \varepsilon_{i-1jk} dx_{i-1} dz_k + \varepsilon_{ijk-1} dx_i dz_{k-1} + \varepsilon_{i-1jk-1} dx_{i-1} dz_{k-1}}{4} \tag{5.20.a}$$

$$\varphi_{xav} = \frac{(dx_i + dx_{i-1})(\sigma_{xijk} dz_k + \sigma_{xijk-1} dz_{k-1})}{4} \tag{5.20.b}$$

Figure 5.3(b) shows another situation where instead of being located in x boundary, a PML cell is located in a boundary of the other two directions. In free space, the electric and magnetic losses are zero. But when there are metal or lossy dielectric materials extending to the boundary surface, some PML cells still have non-zero electric loss. In this case, the electric loss is defined inside the four-cell cubic, just like that in normal Yee cells. Equation (5.8) has a slightly different discretization form from (5.20) in the term of φ_{xav}

$$\varphi_{xav} = \frac{\sigma_{xijk} dx_i dz_k + \sigma_{xi-1jk} dx_{i-1} dz_k + \sigma_{xijk-1} dx_i dz_{k-1} + \sigma_{xi-1jk-1} dx_{i-1} dz_{k-1}}{4} \quad (5.21)$$

Similarly, finite-difference equation for E_{yz} can be derived as

$$E_{yzijk}^{n+1} = \frac{\frac{\eta_{av}}{dt} - \frac{\varphi_{zav}}{2}}{\frac{\eta_{av}}{dt} + \frac{\varphi_{zav}}{2}} E_{yzijk}^{n} + \frac{(dx_i + dx_{i-1})/2}{\frac{\eta_{av}}{dt} + \frac{\varphi_{zav}}{2}} (H_{xijk}^{n+1/2} - H_{xijk-1}^{n+1/2}) \quad (5.22)$$

where η_{av} and φ_{zav} can be calculated, similar to (5.20a) and (5.20b).

Note that in the above equations, the finite-difference expressions do not use the exponential discretization scheme in time domain, which was suggested by [Berenger 1994, Katz et al 1994]. A central finite-difference formulation is used instead, shown in (5.19). The reason of using the central linear formulation is that the wave amplitude does not decay rapidly temporarily but spatially inside PML. Therefore it does not give much improvement for accuracy or stability to use exponential discretization scheme in time domain. In fact the exponential difference scheme could potentially cause numerical instability [Veihl and Mittra 1996].

The discretization of a magnetic sub-component is similar to the electric one. For example, H_{yx} and H_{yz} have the following forms

$$H_{yxijk}^{n+1/2} = \frac{\frac{\mu_{av}}{dt} - \frac{\sigma_{xav}^*}{2}}{\frac{\mu_{av}}{dt} + \frac{\sigma_{xav}^*}{2}} H_{yxijk}^{n-1/2} + \frac{(E_{zi+1jk}^n - E_{zijk}^n)}{(\frac{\mu_{av}}{dt} + \frac{\sigma_{xav}^*}{2})dx_i} \tag{5.23}$$

in which $\mu_{av} = \frac{\mu_{ijk} + \mu_{ij-1k}}{2}$ and $\sigma_{av}^* = \frac{\sigma_{xijk}^* + \sigma_{xij-1k}^*}{2}$

Also, the finite difference for H_{yz} can be derived as

$$H_{yzijk}^{n+1/2} = \frac{\frac{\mu_{av}}{dt} - \frac{\sigma_{zav}^*}{2}}{\frac{\mu_{av}}{dt} + \frac{\sigma_{zav}^*}{2}} H_{yzijk}^{n-1/2} + \frac{(E_{xijk+1}^n - E_{xijk}^n)}{(\frac{\mu_{av}}{dt} + \frac{\sigma_{zav}^*}{2})dz_k} \tag{5.24}$$

in which $\mu_{av} = \frac{\mu_{ijk} + \mu_{ij-1k}}{2}$ and $\sigma_{av}^* = \frac{\sigma_{zijk}^* + \sigma_{zij-1k}^*}{2}$

All the PML equations for the other sub-components can be derived by the similar procedure. From the above equations, we can see that the PML equations have the forms similar to the FDTD equations. This similarity provides a great help in our programming task.

5.4. Numerical Verification

A microstrip line with dielectric media cover is chosen to show the performance of the proposed PML boundary conditions at inhomogeneous boundaries. The three-dimensional structure of the microstrip line is shown in Figure 5.4. The metal ground and the two layers of dielectric substrate (ε_{r1}=9 and ε_{r2}=6) of the microstrip line extend to the FDTD boundary in both z and y directions. The metal strip extends to the boundary in y direction and is covered by two dielectric layers (ε_{r1}=9 and ε_{r2}=6) on top.

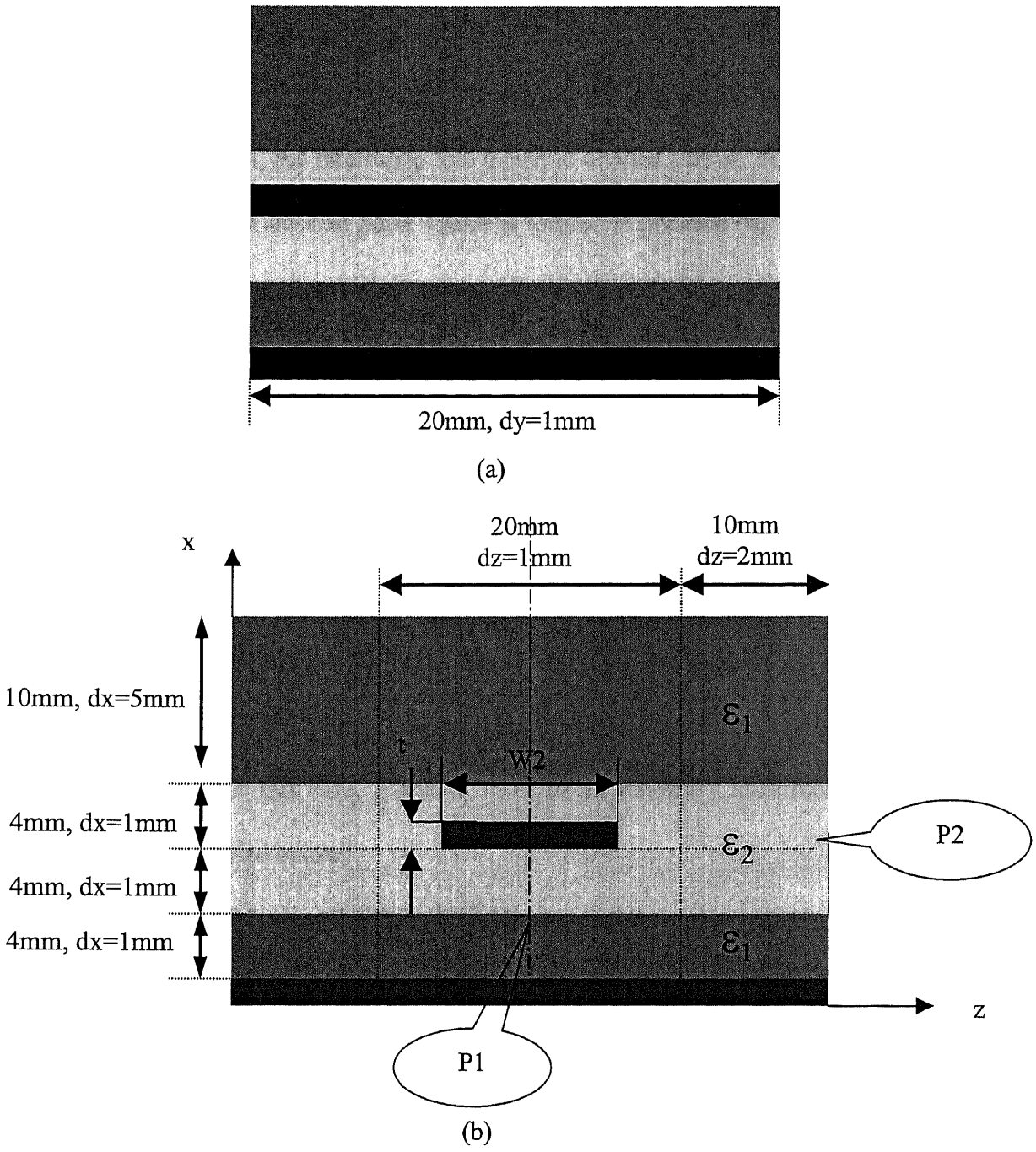

Figure 5.4 The microstrip line structure, (a) longitudinal view, (b) transverse view. D=10 cells, t=2 cells, W=12 cells, ε_1=6, ε_2=9, metal conductivity is 10^7 (S/m). P1, P2 are two observation points.

The excitation is an E_x additive hard dipole source in the center of the microstrip line and occupies only one cell. The source generates complicated wave configurations inside the structures so the general performance of the PML absorption can be investigated. The source has a Gaussian pulse profile with 75ps width and 1V/m amplitude.

Shown in Figure 5.4, the microstrip line model is divided into an FDTD mesh Ω_p of $21\times20\times30$ cells. The Gaussian pulse source is located at position (6, 10, 15). 16 PML layers wrap the FDTD mesh, which has nonuniform cell sizes in z and x directions. The cells near the metal strip have finer cell sizes, dx=dz=1mm, than the cells far from the strip, where dx=dz=2mm. The cell size in y direction is uniform, dy=1mm. The temporal increment is 4.08ps according to CFL criterion based on the smallest grid length.

As mentioned in Section II, PML layers with a geometric loss profile have empirical parameters g and σ_0. A table was given in [Berenger 1996] to decide these parameters in 2D FDTD analysis. For this 3D test case, data in that table can not be used directly. But the parameters can be selected based on the same concept. Also because the nonuniform cell sizes apply in this test case, g and σ_0 in different boundary locations are chosen different values and listed below:

x+ boundary: g_{x+}=2.1, σ_{0x+}=0.278 (mS/m)

x- boundary: g_{x-} =1.9, σ_{0x-} =0.278 (mS/m)

y + and y- boundary: g_{y+} =g_{y-} =1.9, σ_{y+} =σ_{y-}=0.278 (mS/m)

z+ and z- boundary: g_{z+} =g_{z-} =2.1, σ_{z+} =σ_{z-}=0.278 (mS/m)

In fact, many possible combinations of g and σ_0 parameters set can be used in the calculation. They have to be carefully selected to achieve better absorbing performance.

For this test case, σ_0 is set to be uniform and different values of g are tried to get the better performance.

In order to estimate the error caused by a PML layer, reference results of this model are obtained by running simulation in a large mesh, Ω_r, with the same microstrip structure. The outer boundary of Ω_r is so remote that the EM fields within Ω_p are not influenced by the reflections generated at the outer boundaries of Ω_r. In this dissertation, this mesh size is $80\times150\times140$. The error is the abstract value of the subtraction of the EM field values in Ω_p from that in the corresponding point in Ω_r.

In mesh Ω_p, two observation points, P1 and P2, are located at the interface of the PML and FDTD cells, shown in Figure 5.4 (a). The error spectrums at point P1 and point P2 are shown in Figures 5.5 and 5.6, respectively. It can be seen that in the frequency range of the reference wave, at both points the numerical errors caused by the PML boundaries are lower than 10^{-4}, that is –80 dB.

The global error due to the PML reflection versus time steps is graphed in Figure 5.7. The global error is the summation of the square of electric components all over Ω_p at each time step. Figure 5.7 also demonstrates the excellent absorbing performance of the PML formulation proposed in this dissertation.

5.5. Conclusion

The Berenger's perfectly matched layer (PML) absorbing boundary conditions are applied to terminate a microstrip line with metal strip and multilayer dielectric media extending into the PML regions. The PML absorbing boundary conditions are extended into a commonly used practical situation, which involves inhomogeneous boundary with

multi-dielectric and metal layers in a non-uniform FDTD grid. Although the media considered in this dissertation are metal and lossless media, it is suitable for many applications in the microwave and high frequency circuit simulation. In order to better handle the inhomogeneous properties of the PML layers, the integral form of the Maxwell's equations discretized by a central finite-difference scheme instead of exponential difference scheme is utilized to derive the FDTD equations for updating field components inside PML media. The derived formulae are flexible and convenient for generating and handling the PML layers in a non-uniform FDTD grid. The numerical simulation results show excellent absorbing performance to EM waves in a multilayered structure and therefore prove the validity and accuracy of the formulation. The enhanced PML method increases the FDTD ability to compute complicated structures in multi-mode and near field conditions.

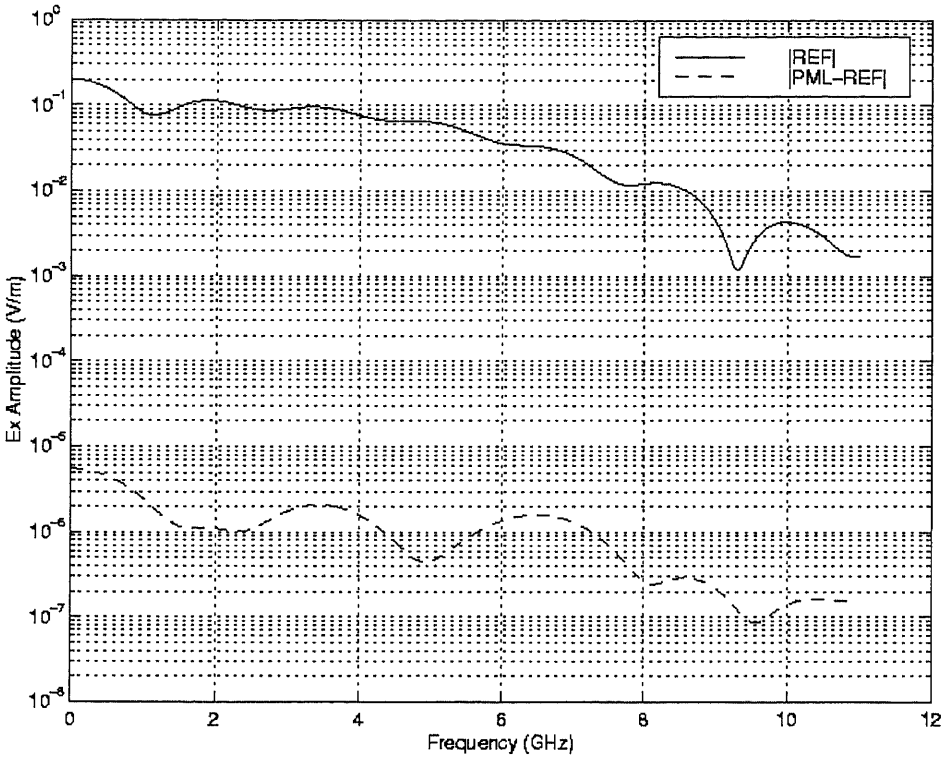

Figure 5.5 PML error spectrum distribution of point P1 in Figure 5.4.

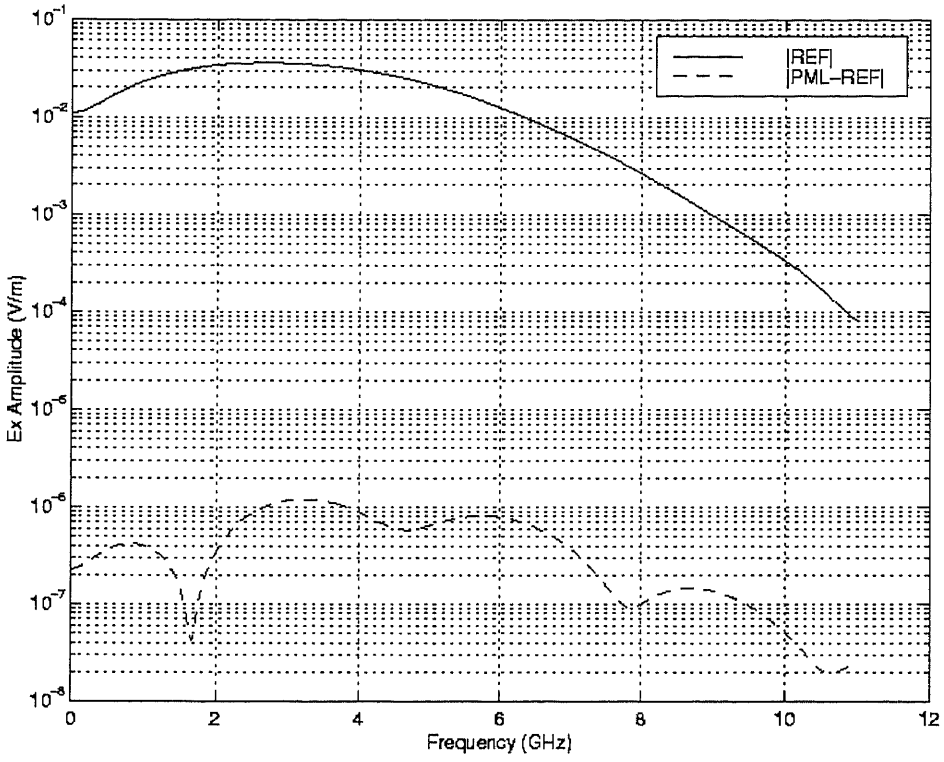

Figure 5.6 PML error spectrum distribution of point P2 in Figure 5.4.

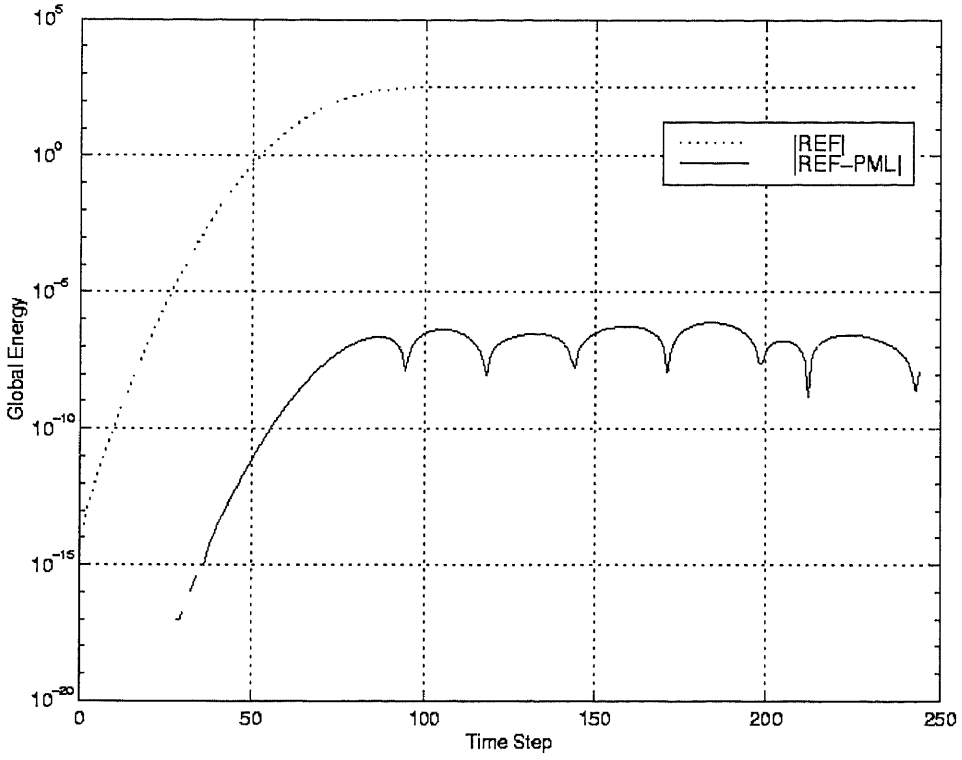

Figure 5.7 Global error (the sum of square of E_x, E_y and E_z over all the Yee cells) versus time steps.

CHAPTER 6

HYBRID CO-SIMULATION MODEL'S APPLICATIONS

6.1. Introduction

Based on the previous chapters, a three-dimensional FDTD hybrid co-simulation code is built up to apply the proposed hybrid co-simulation model to some EM system simulations. In this code, a non-uniform FDTD grid is implemented. A simple circuit simulator with a lumped element library is set up to cooperate with the three-dimensional FDTD code according to the co-simulation mechanism described in Chapter 4. The library includes some commonly used lumped components, such as resistor, capacitor, inductor, Schottky diode, Gunn diode, negative resistor, BJT, and varactor diode, etc. The boundary conditions utilized are the PML boundary conditions described in Chapter 5.

In this chapter, several microwave and high-speed systems, such as power divider, spiral inductor, and patch antenna, are simulated to demonstrate the validation and implementation of this model. Some important aspects involving the extraction of the lumped characteristics of distributed structures from the co-simulation are presented. These aspects are very important for the FDTD modeling of a newly developed system and understanding of the relation between real system responses and the FDTD simulation results.

6.2. Power Divider

The first example is a microstrip line power divider, as shown in Figure 6.1. The circuit is a hybrid system consisting of distributed microstrip branches and some lumped elements. The lumped elements in the circuit are a lumped resistive voltage source driving the power divider, two Schottky diodes loaded at two output ports and a balancing resistor between the two strip lines near the output ports. The balancing resistor is to adjust power assignments of the two ports. The dimensions of the used FDTD grid consist of 120×90×20 1mm cubes, and the time increment is 1.667ps. The characteristic impedance for all microstrip lines in the circuit is 50Ω [Wadell 1991].

Figure 6.2 shows the time domain current responses of both diodes to a 900MHz sinusoidal excitation at the input port. The currents flowing through both diodes are overlapping of each other, indicating perfect matching between two arms of the divider. In order to validate our simulation results, they are compared with the results from Serenade, Ansoft®, which can only provide steady state solutions. The steady solutions of the two simulations are basically matched.

A spatial distribution of one electrical field component (Ez) is shown in Figures 6.3 and 6.4, where strong signal reflection and coupling are clearly seen near the T-section at the input port and between the microstrip lines near the output ports. The results show that, for the simulation of an EM system with the high-speed signals and the nonlinear components, it is necessary to implement the time-domain and full-wave analysis, which is not in the Serenade and most other packages.

The balance resistor R is to balance the power assignments to the two branches. Figures 6.5-6.7 show the behavior of the power divider under an unbalanced condition

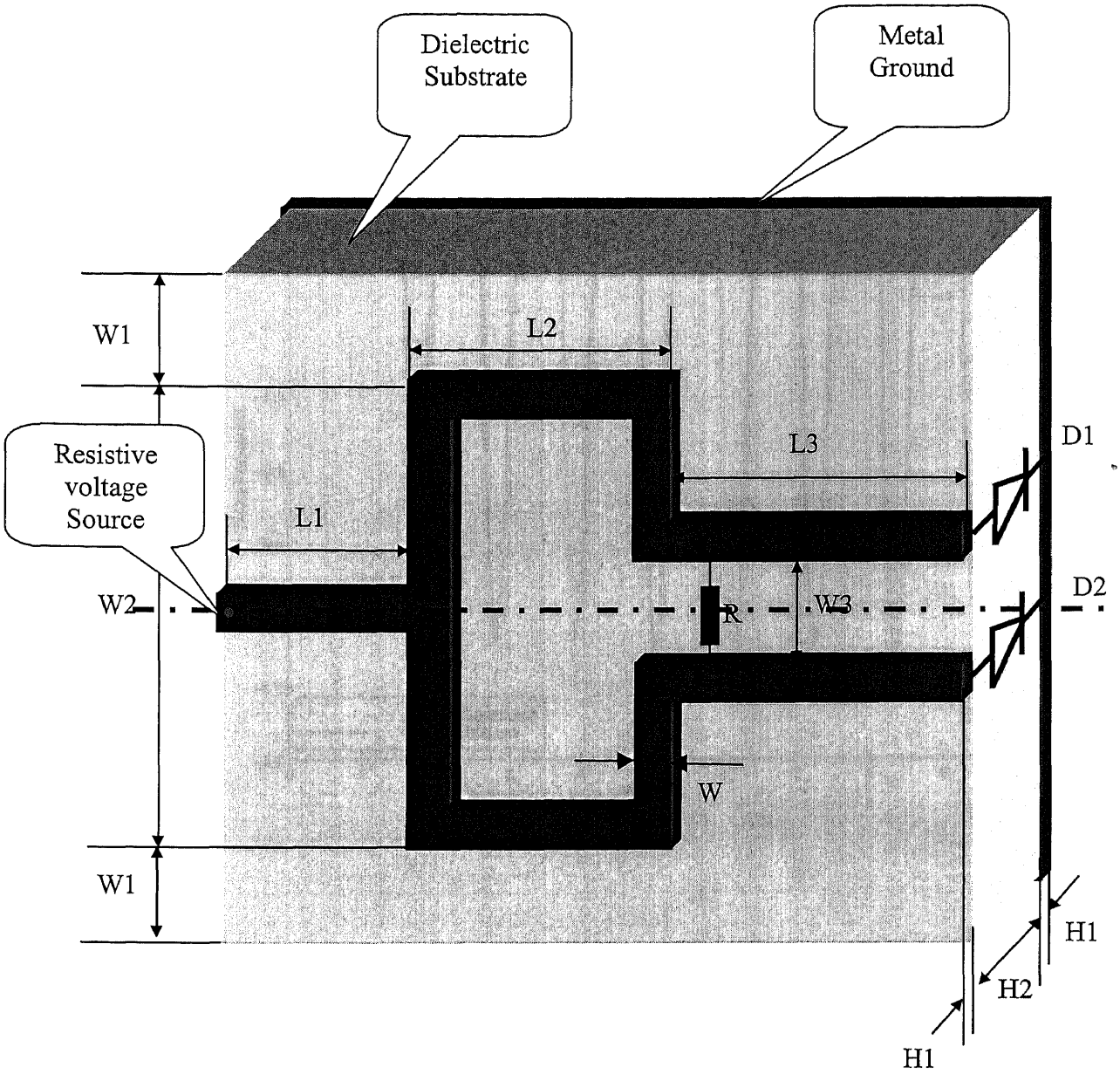

Figure 6.1 Configuration of the microstrip line power divider. In the figure (unit: mm), W=1, W1=10, W2=48, W3=12, L1=20, L2=28, L3=32, H1=1, H2=5. The substrate permittivity is 9.07 and metal conductivity is 10^7mho/m. R=50ohm, Resistive voltage source: sinual wave with 900MHz frequency, Rs=50ohm.

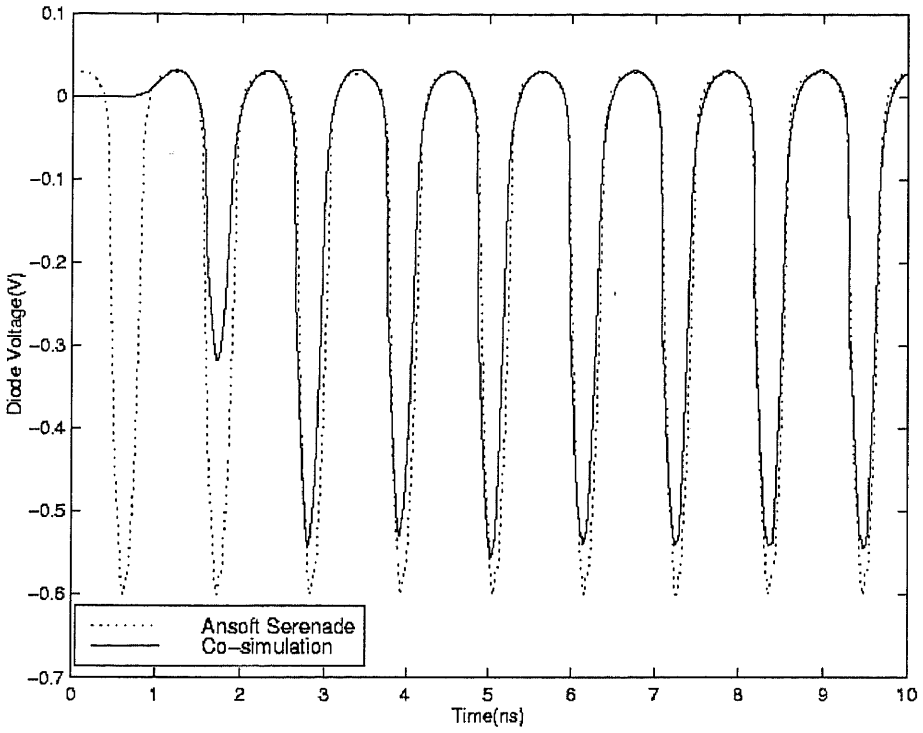

Figure 6.2 The waveform of the diode currents obtained from co-simulation and Ansoft Serenade package when the power divider is in balanced condition.

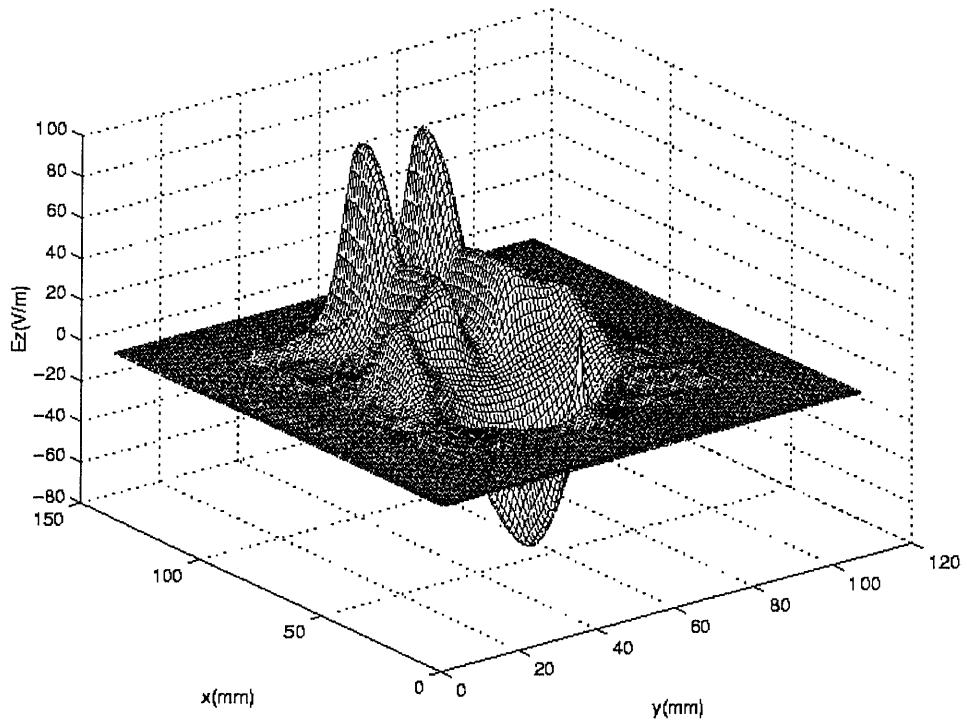

Figure 6.3 The diagram of Ez distribution of the power divider shown in Figure 6.1 under a balanced condition.

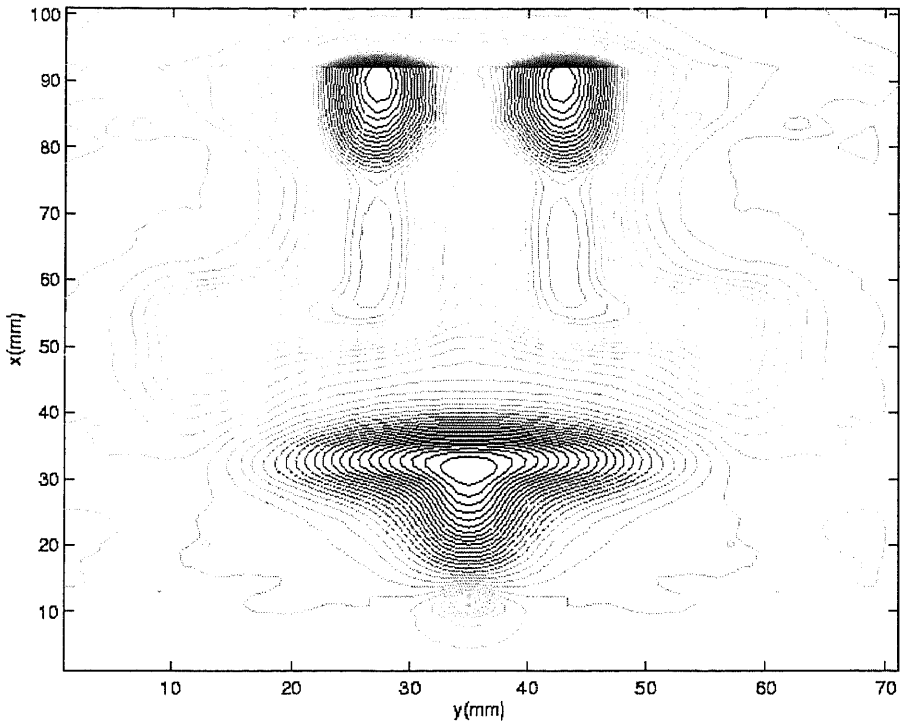

Figure 6.4 The contour of Ez distribution shown in Figure 6.3

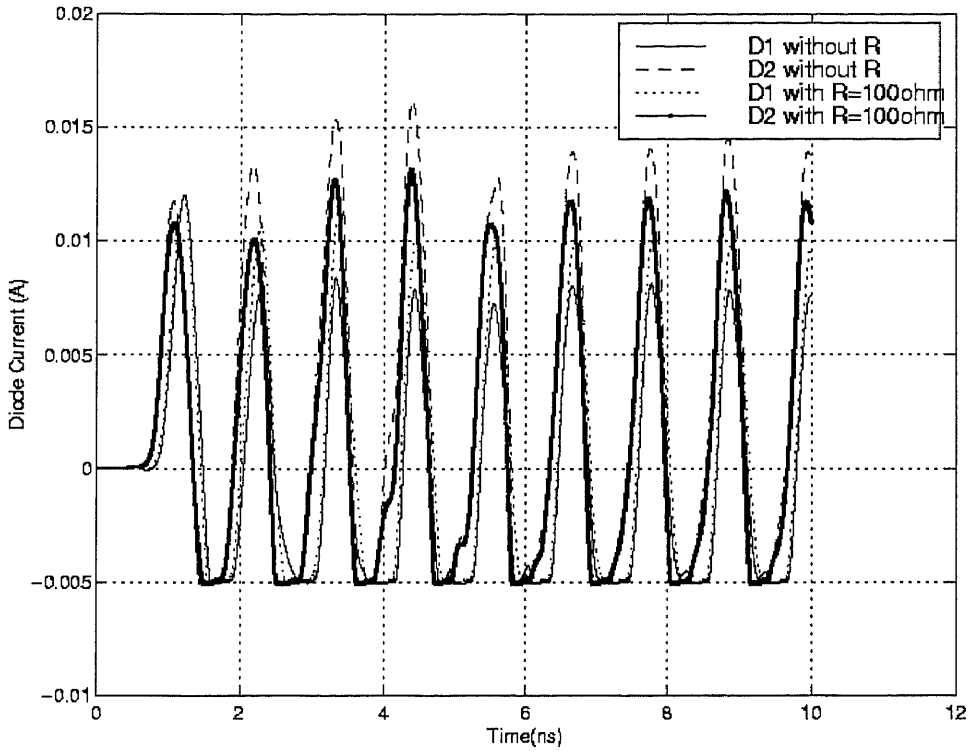

Figure 6.5 The waveforms of the diode currents obtained from co-simulation when the power divider is in an unbalanced condition.

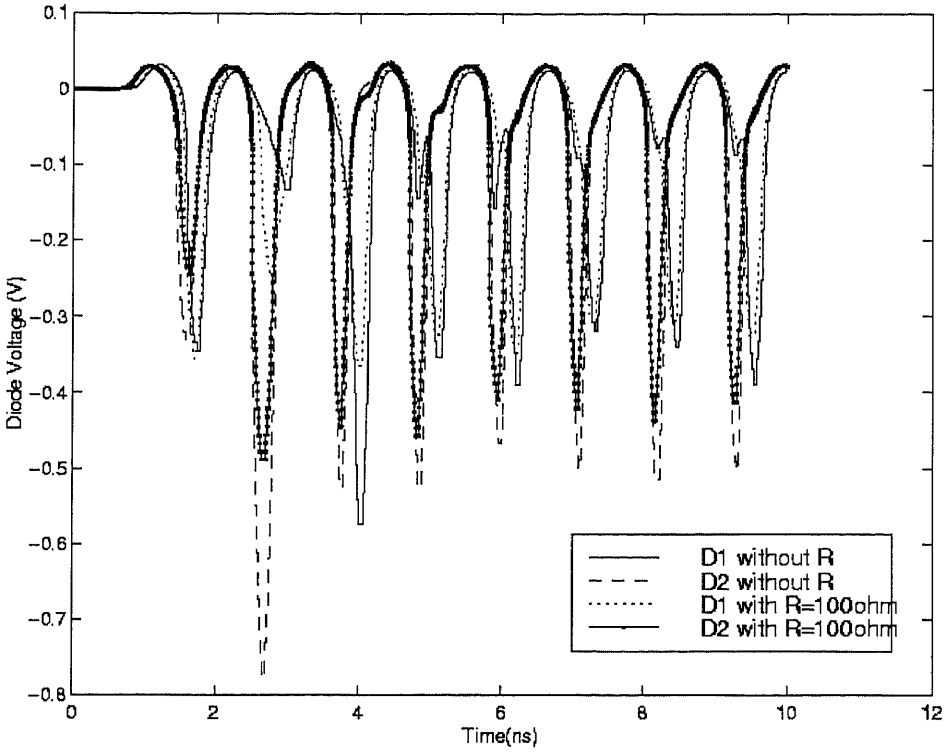

Figure 6.6 The waveform of the diode currents obtained from co-simulation when the power divider is under an unbalanced condition and R is 10 ohm.

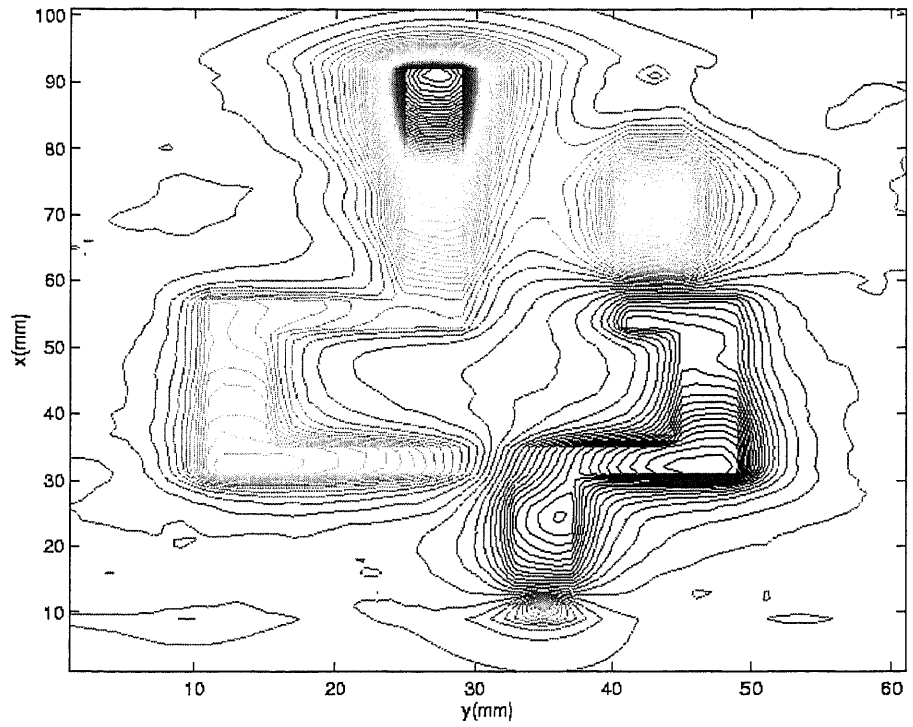

Figure 6.7 The contour of Ez distribution shown in Figure 6.3 when the two branches are not balanced.

that is made on purpose. The simulation is run under two conditions, without the balancing resistor R and with R equal to 100Ω. In Figure 6.5, the currents of the diodes in the above conditions indicate that the balance resistor effectively reduce the current difference between the two diodes. Figure 6.6 shows the voltage of two diodes in the above conditions. Combining Figures 6.5 and 6.6, we can see that the balance resistor effectively balances the power assignments to the two branches. The strong field effects are also shown in Figure 6.7, which is the spatial distribution contour of Ez in the power divider under an unbalanced condition when R is used.

Eight PML layers are used as boundary in this case. The simulation time is 3 hours with an Ultra60 workstation.

6.3. Microstrip-Fed Patch Antenna

Microstrip antennas are of low profile that are required for the applications where the weight cost, performance, easy installation, and aerodynamic profile are the constraints. With modern printed-circuit technologies, they can be manufactured inexpensively and compatible with MMIC design. Especially, the microstrip antennas have many applications in the mobile radio and wireless communications. The co-simulation can be used in the simulation of a microstrip patch antenna. In this section, a microstrip-fed patch antenna is simulated in order to demonstrate the implementation of 3D FDTD simulation with inhomogeneous boundaries. Some aspects about the extraction of S parameters are described here.

The dimensions of a microstrip antenna are shown in Figure 6.8. Non-uniform cell sizes in x direction are utilized to fit the geometry of the antenna exactly, as shown in

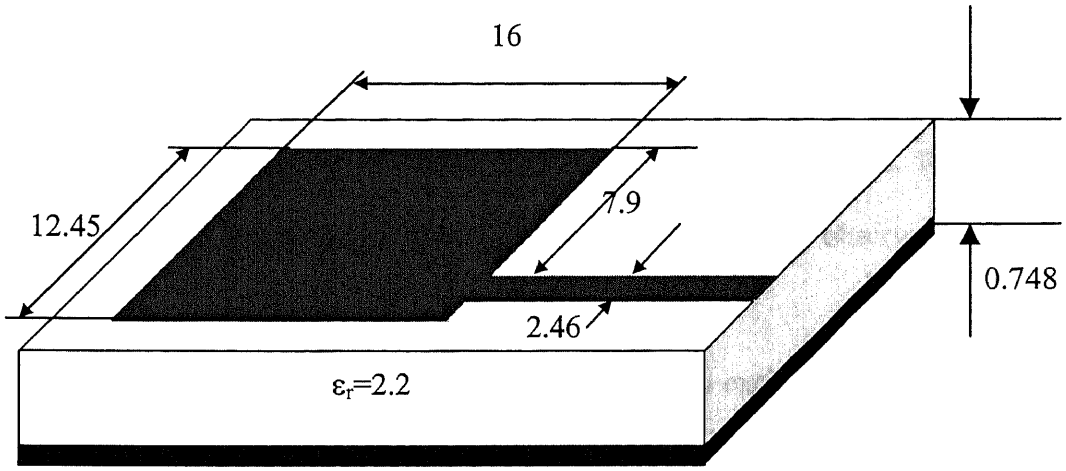

Figure 6.8 A microstrip-fed rectangular patched antenna (unit is mm).

Figure 6.9. The cell sizes in z and y directions are uniform, dy=0.4mm and dz=0.265mm. In this non-uniform grid, dx is manipulated to be as close to dy as possible to approximate a square shape cell. At the mean time, the difference between the cell sizes is minimized to reduce the numerical error caused by a non-uniform grid. The temporal increment dt is 0.441ps.

In order to obtain the S parameters, which is S11 for this one port circuit, some supplemental items of the FDTD methods have to be considered carefully.

Excitation Placement

A normal FDTD simulation starts from time step zero when the EM field components vanish everywhere. Then an excitation is launched to the system in the input port of the antenna and the EM waves propagate from the source to other places. The electrical or magnetic field components in some points, which are called observation points, are recorded during the whole simulation process.

For this microstrip-fed antenna, the excitation has to excite a vertical electrical field between the feeding microstrip and the ground. The excited field propagates along the feeding line to the patch in a plane-wave form. The excitation alignment for this simulation is shown in Figure 6.9(a) to achieve the required input wave mode. There are several sources between the strip and ground. They have the same waveform and are adjacent to each other in the FDTD grid. The sources are transparent to any wave passing them by using soft electrical source model, in which the electrical field of the source is the summation of the forced value and the electrical field value calculated by FDTD equations.

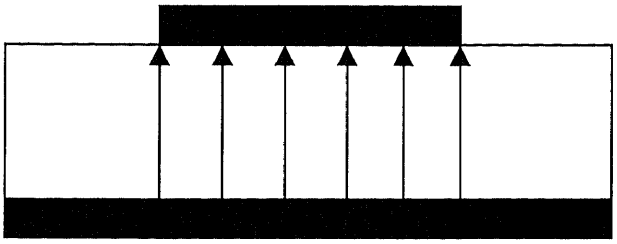

(a)

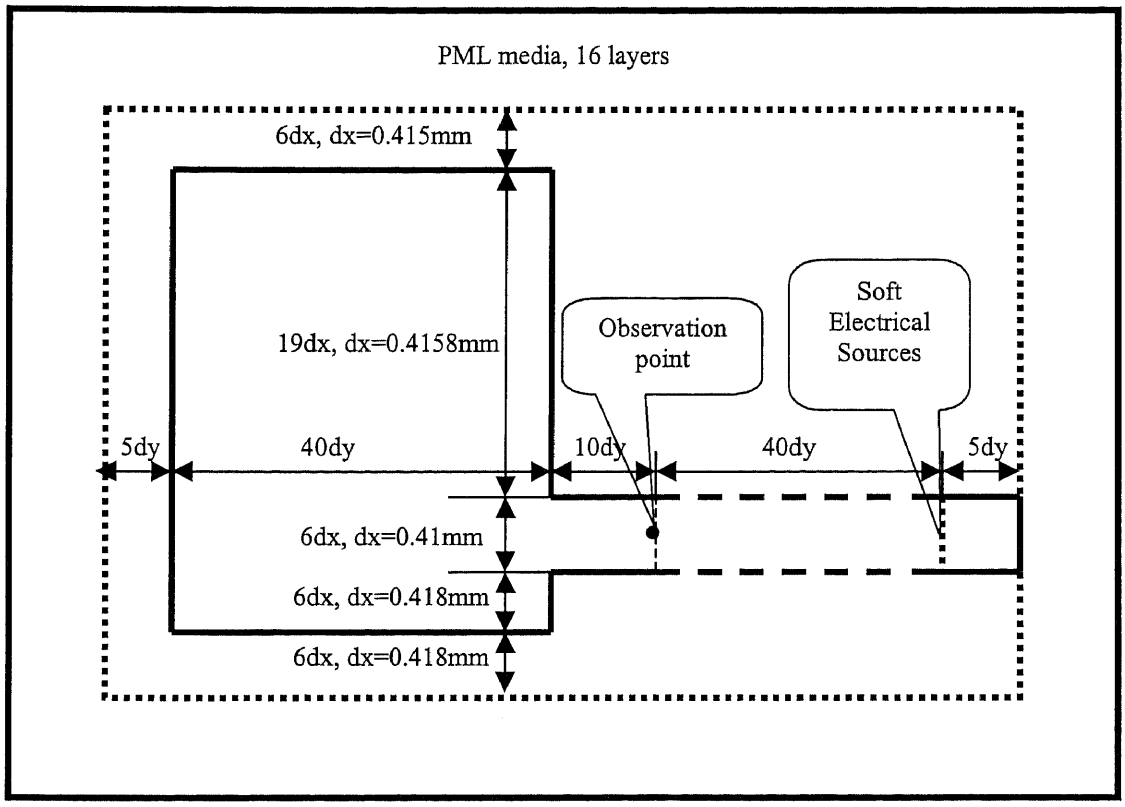

(b)

Figure 6.9 FDTD mesh of the microstrip-fed rectangular patched antenna shown in Figure 6.8, (a) Source alignment (side view), (b) mesh configuration (top view).

The EM field near the sources has strong near field effects. Because a plane wave has to be fed into the structure to extract S parameters from the simulation, the sources have to be put enough distance away from the discontinuity. Otherwise, the near field effects around sources make the amplitude of the traveling plane wave mode very small compared with that of other high order modes and evanescent modes. Under this condition, it is very hard, if not impossible, to extract S parameters from the FDTD simulation.

The generation of a plane wave in the feeding microstrip line may need a feeding line longer than that in the practical system. The distance between the excitation and discontinuity is about one to two wavelengths of the EM wave with frequency of 20GHz, which is the highest frequency required.

Excitation Pulse Shape

A Gaussian pulse is a good profile to be used for the excitation because it provides a wide band spectrum. It is widely used to obtain the spectrum parameters from FDTD simulations. The profile of the Gaussian is

$$e^{-(\frac{t-t0}{t_w})^2} \tag{1}$$

The selection of t_w depends upon the required frequency range and the FDTD cell size. To this antenna, the required frequency range is from 0 to 20GHz. t_w is chosen to be 20ps which corresponds to frequency 50GHz larger than 20GHz, the highest required frequency. The selection of t_w also depends on the FDTD cell size is considered. In this case, the cell size is approximately 0.4 mm, which is between 1/10 and 1/20 of the wavelength of the wave with 50GHz frequency. If a narrower pulse were chosen, the FDTD dispersion error would be higher.

In order to load the Gaussian pulse smoothly, the delay of the Gaussian pulse, t_0, has to be bigger than the pulse width t_w. Normally, t_0 equal to $3t_w$ makes the pulse smooth enough.

Observation Position

At an observation position, the voltage between the microstrip and ground is recorded at every FDTD iteration. The voltage is the integral of the electrical field from the ground to the microstrip line. In transverse (y) direction of the feeding line, the observation point is in the center of the strip. In longitudinal (x) direction, the observation point is in a place between the discontinuity and the source. This position has to be considered carefully to match the simulation results to the measured ones.

The S parameters of a device are measured by a network analyzer. Matching transmission lines are connected from the analyzer to the ports of the device. The EM signal generated from the analyzer propagates to the device and the reflecting or transmitting signal caused in the device propagates to the analyzer. This process allows the analyzer to calculate the S parameters from the detected signals. The signal obtained by the analyzer has to travel a certain distance from the device to the analyzer. Thus only the traveling waves in the matching transmission line are used in the calculation of S parameters. Suppose there is a strong evanescent wave in the device. Because it decays rapidly through the matching line, the analyzer cannot detect it at all. Therefore, the evanescent wave is not presented in the S parameters from measurement. In the FDTD simulation, if an observation point is put in the discontinuity of the system, all the EM waves, including traveling waves and evanescent waves are recorded. The S parameters from simulation, which is based on the record of this point, can not match the

measurement result if the evanescent wave is strong. Therefore, the observation point has to be kept a distance from the discontinuity to eliminate the evanescent wave.

Also, the observation points for S parameters extraction have to be kept an enough distance from the excitation source because near the source, the electrical field is not represented well by a plane wave.

The excitation position, observation position and the discontinuity of the circuit are shown in Figure 6.9(b) with the considerations of the source placement and the evanescent waves caused by the discontinuity. The distance between the excitation and the continuity is about 50 cells. The distance between the observation point and the discontinuity does not need to be as long as the distance between the observation point and the excitation when the interested circuit has no active source. As shown in Figure 6.9(b), the observation point is in a place between the source and discontinuity, and closer to the latter.

Scattering (S) Parameters

S parameters are normally used to describe a distributed system. Suppose we have a two port network, S parameters of this network is defined as

$$\begin{bmatrix} V_r^1 \\ V_r^2 \end{bmatrix} = \begin{bmatrix} S_{11} & S_{12} \\ S_{21} & S_{22} \end{bmatrix} \begin{bmatrix} V_i^1 \\ V_i^2 \end{bmatrix} \tag{2}$$

In which i means an input signal and r means a reflecting signal.

In order to obtain the S parameters for the response of port 1, namely S11 and S21, from the FDTD simulation, we have to run the FDTD simulation twice, as shown in Figure 6.10. First, obtain the input signal V^1_i by running the FDTD simulation for a distributed structure that has only the feeding microstrip line. Second, obtain the total signal V^1_t, which is the summation of the input signal and reflecting signal, by running

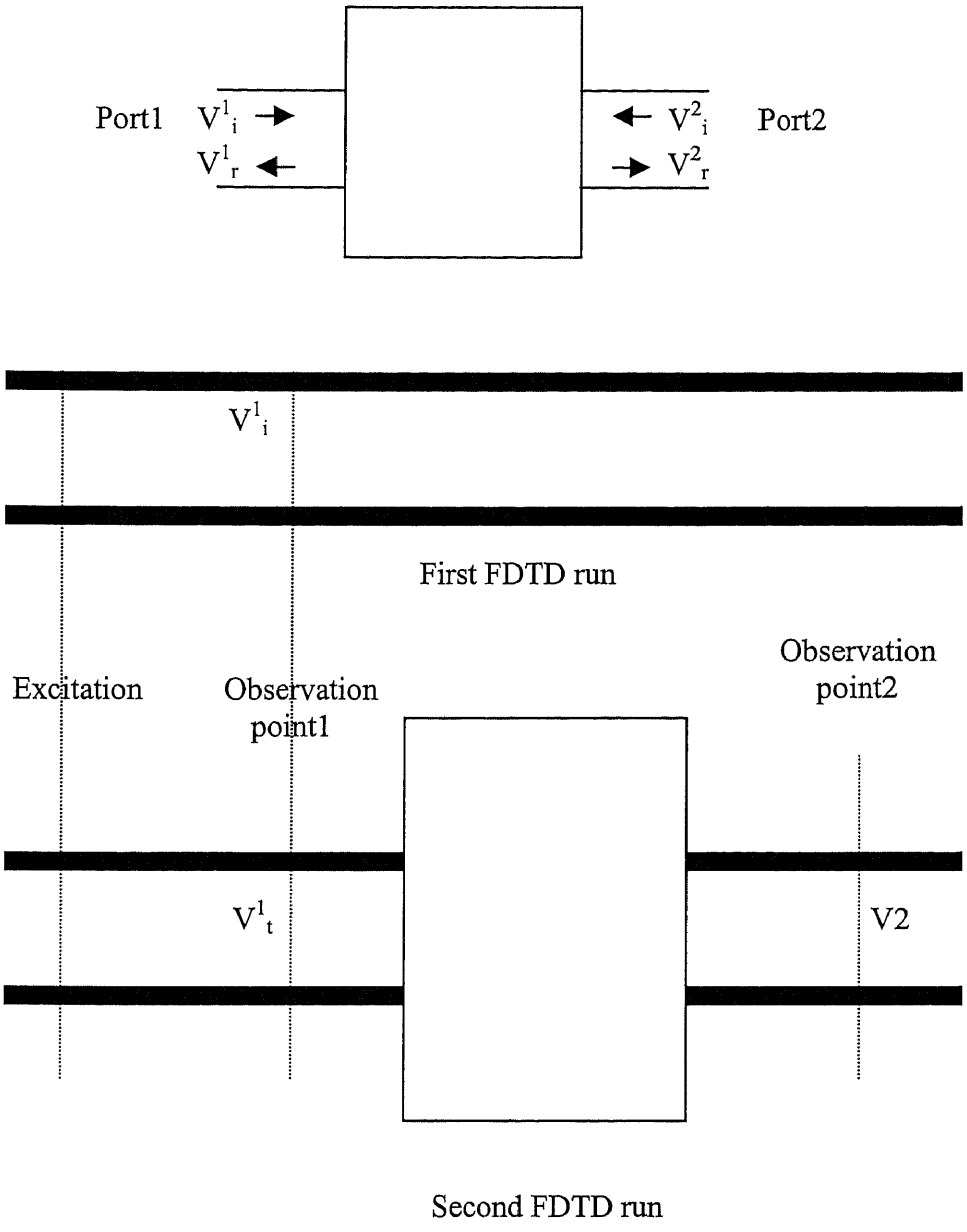

Figure 6.10 S parameter extraction scheme from FDTD

the FDTD simulation for the whole system. Then the reflecting signal is the substraction of input signal from total signal. The S parameters are obtained by exerting DFT to the obtained time-domain input and reflecting signals

$$S_{11} = \frac{fft(V_t^1)}{fft(V_i^1)} \tag{3}$$

$$S_{21} = \frac{fft(V_r^2)}{fft(V_i^1)} \tag{4}$$

The simulation results are shown in Figure 6.11. This example comes from Sheen's publication [Sheen et al 1990], in which, a three-dimensional FDTD simulation with Mur's secondary order boundary condition was done and the simulation result was compared with the measurement result and they showed a good agreement. Compared with our results, closer to the measurement result in terms of the S11 amplitude, we think the boundary conditions are the main difference of these two. Another reason would be that in our simulation, the non-uniform grid matches exactly the geometry shape of the antenna to make the simulation more accurate.

6.4. Spiral Inductor

Due to the enormous market potential of wireless communications, improvements of RF circuit elements for the cellular and PCS bands are in strong demand. These elements enable the on-chip-matching network that, in turns, minimizes the RF circuitry as well as the board space. One of the major components is the inductor. In these frequency ranges, the traditional microwave transmission line approach is not practical because of the longer wavelength that results in much larger circuit sizes. So the MMIC elements such as spiral inductors are common used in these applications.

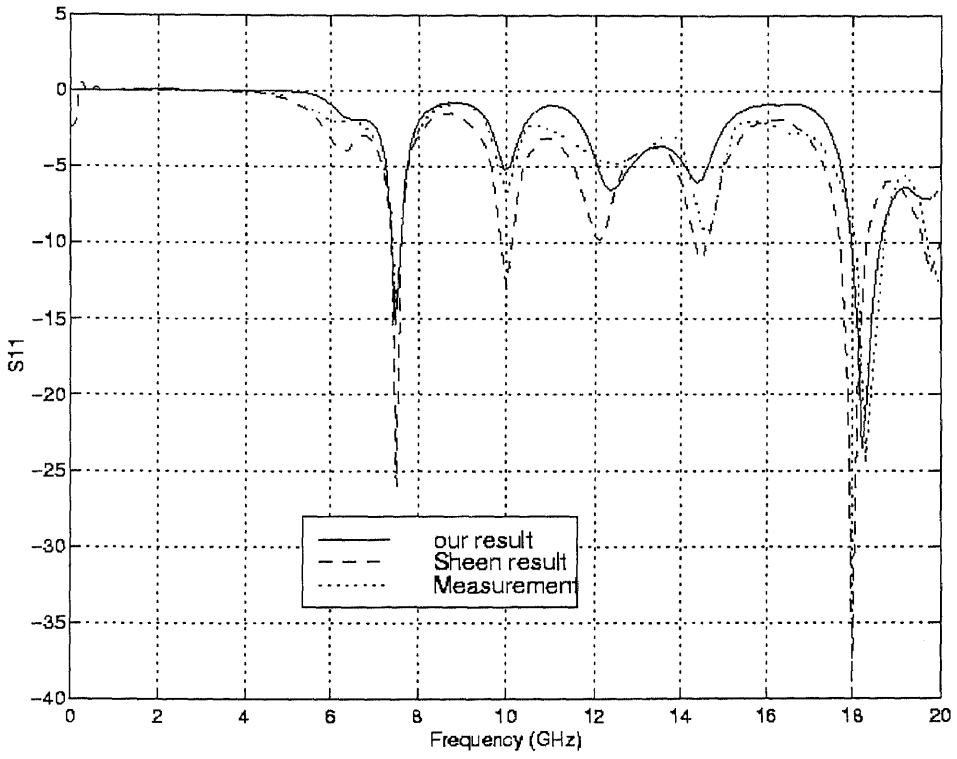

Figure 6.11 S11 of the microstrip patch antenna shown in Figure 6.8. Solid line: measurement result, dashed line: result from [Sheen et al 1990], dotted: result of this dissertation

In this section, a MMIC impedance matching circuit consisting of a spiral inductor and a lumped capacitor is analyzed by our proposed field-circuit co-simulation. The dimensions of the circuit are shown in Figure 6.12. The spiral inductor has two turns and width of the strip is 15μm and the spacing between strips is 10 μm. The simulation purpose is to obtain the scattering (S) parameters of the circuit.

The challenge for the circuit to our simulation is its very small physical dimensions. This matching circuit is utilized in a relatively low microwave frequency range, less than 20GHz. The wavelength of the signal is larger than 15000 μm in free space. Thus the very small circuit dimensions make the FDTD grid too fine compared with the wavelength. This introduces s a heavy computational burden to the simulation. If a uniform cell size 10μm is chosen, according to CFL stability criterion, the time increment is about 16.67fs. In order to obtain the spectrum responses in the range of 0-20GHz, the total simulation time is about 10ns. Thus totally 600 thousand iterations have to be run to accomplish this simulation. For three-dimensional simulation, this number is huge in terms of the computational cost and numerical stability of boundary conditions becomes a question.

As mentioned in the above section, in order to obtain the S parameters of a circuit, the excitation and observation point have to keep a certain distance from the discontinuity. Otherwise the EM wave in the observation point is no longer a traveling plane wave and the results obtained do not provide correct information about the reflecting and transmitting response of the circuit to an incident wave. The distance is about 1 to 2 wavelengths of the EM wave with the highest interested frequency. In free space, the distance is about 15000 μm, and in the dielectric layer with permittivity equal to 13 it can

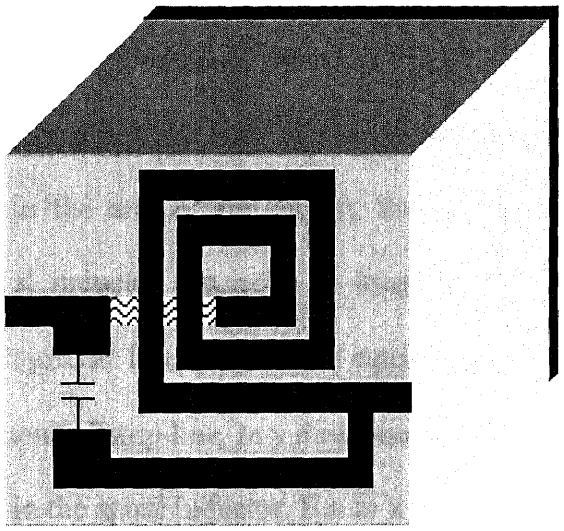

(a) circuit idagram

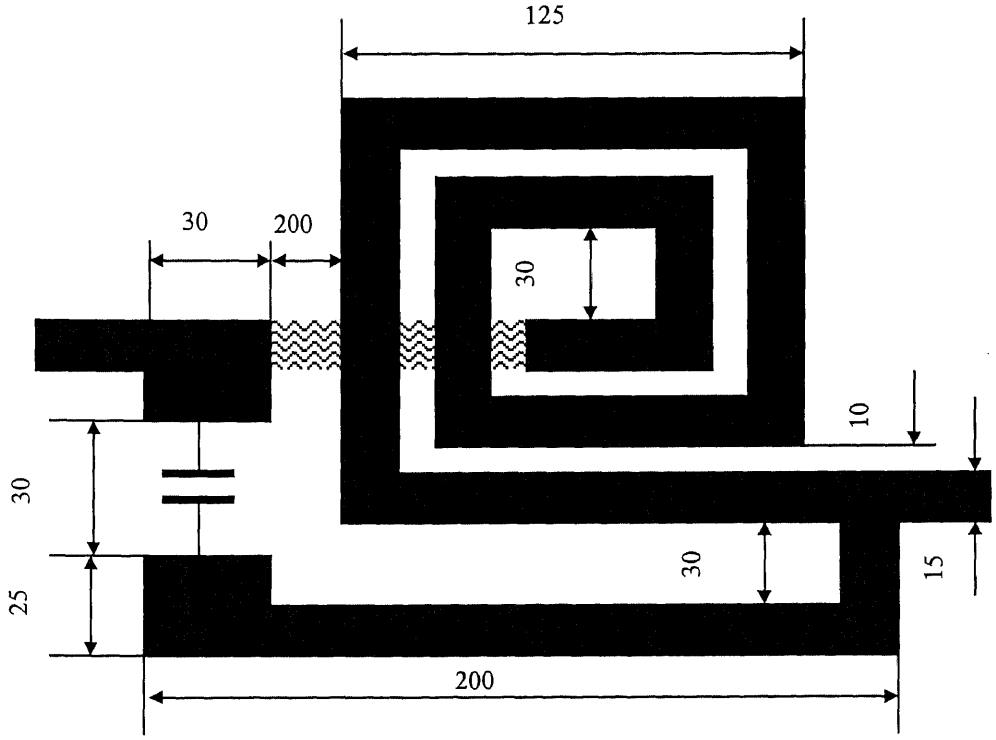

(b) front view

Figure 6.12 An impedance matching circuit with a spiral inductor and a lumped capacitor

be reduced to 5000 μm approximately. This is still much longer than the dimensions of the circuit itself that is about 200 μm. Thus, in order to release the computational burden, a non-uniform FDTD grid needs to be utilized into the simulation.

The FDTD grid has two regions, the area of the spiral inductor and the area of the extended microstrip line. In the area of the circuit, the cell size is chosen to fit the geometric shape of a spiral inductor precisely. In longitudinal (x) and transverse (y) directions, dx and dy are 10 μm or 15μm, which are equal to the strip spacing or the strip width. In the area of the extended strip line, in y direction, the cell size distribution has to be kept as the same as that in the spiral inductor. But in x direction, the cell sizes increase from 15 μm to 265 μm from the discontinuity to the feeding line, and then is kept uniform until the boundary. In vertical (z) direction, from the ground to strip, dz decreases from 40um to 10 um.

The reason to enable us to choose the non-uniform grid in the simulation is that as long as the cell size is much smaller than the wavelength, the numerical error of the simulation is small. The biggest concern of the non-uniform grid is the influence of the cell shape to the simulation result. In this grid arrangement, in some place, the dimensions of the cell is 265 μm ×10 μm ×10 μm, which deviates to the normal cubic shape significantly. In order to estimate the numerical errors in this non-uniform FDTD grid, two-dimensional numerical error estimations based on the results of Chapter 3 are performed. Figures 6.13 and 6.14 are the numerical errors of transmission angle and reflection coefficient due to the different cell sizes, 10 μm and 265μm. They show about one percent the numerical errors in this case. Although this estimation is not sufficient for

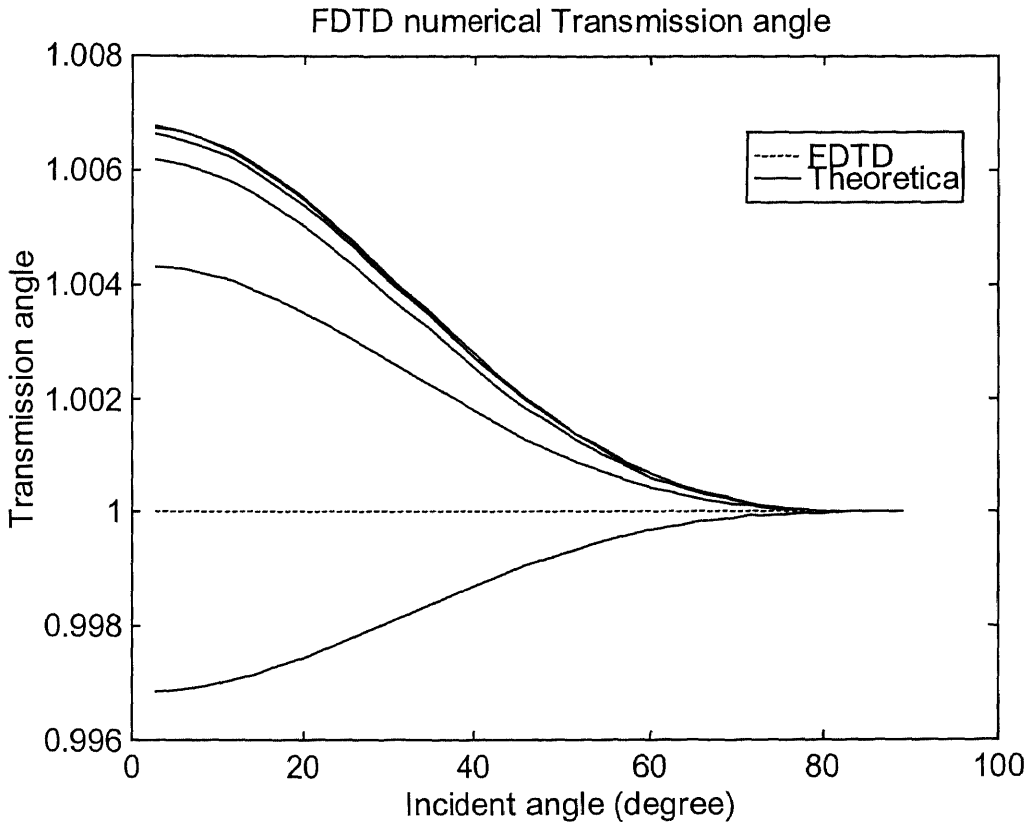

Figure 6.13 FDTD numerical transmitting angle in a non-uniform grid, f=20GHz, dx1=265μm. Dashed line: theoretical solution, solid line: FDTD numerical solutions, from bottom to top, dx2=320, 160, 80, 40, 20, 10μm, ε=13.

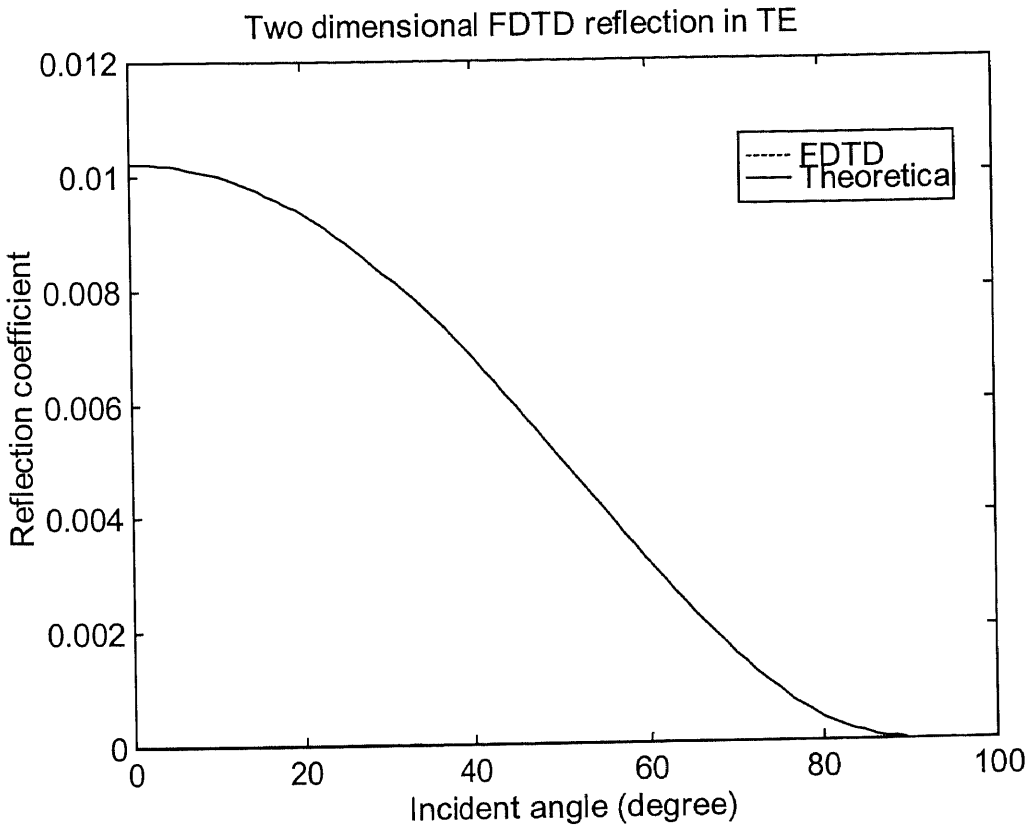

Figure 6.14 FDTD numerical reflection coefficient in a non-uniform grid, dx1=265μm. dx2=10μm, f=20GHz ε=13.

three-dimensional FDTD simulation, it provides very useful information to help us generate the FDTD grid.

Because of the extremely non-uniform FDTD grid and the big disparity of the permittivity of dielectric substrate and the air above the metal strip, PML construction mentioned in Chapter 5 is carefully performed. The initial conductivity of the PML layers is decided according to the total running time, which is 10ns in this case [Berenger 1996].

$$\sigma_0 = 2\pi\varepsilon_0 \frac{1}{10D_c} \tag{5}$$

where D_c is the total running time. The number of PML layer is chosen to be 16 because this relatively large number of PML layers provides a smoother PML loss profile needed by the very large number of FDTD iterations. Because the cell sizes at boundaries have two values, 265 μm and 10 μm, two g values are chosen, 1.78 for 265 μm and 2.34 for 10 μm.

A Gaussian pulse is added as an excitation. Its width is 20ps and delay is 60ps. The observation point at port 1 is located at 40 cells away from excitation in x direction and the observation point at port 2 is at 10 cells away from the discontinuity near port 2.

The total required memory for this model is 112Mbytes.

The simulation results are shown in Figures 6.15-6.20. The measurement results are shown in Figures 6.19 and 6.20, which are done by Bell Labs, Lucent Technologies, where this matching circuit is used for wireless communication applications.

Figures 6.15 and 6.16 are diagrams of the input and total voltage waveforms of port1. Notice that the total simulation time does not reach 10ns that provides 0.1GHz resolution in the FFT transform. The wave amplitudes are near zero after about 1ns, as shown in Figures 6.15 and 6.16. Thus, we add more zeros to the time sequence to make the total

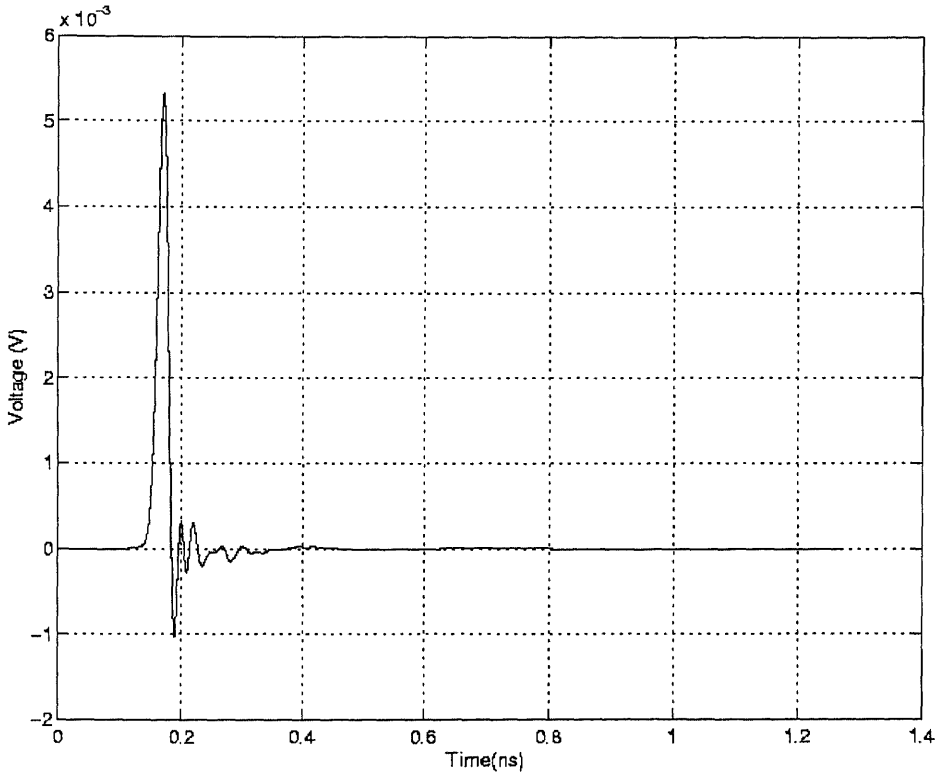

Figure 6.15 Voltage of input signal vs time of the impedance matching circuit shown in Figure 6.12.

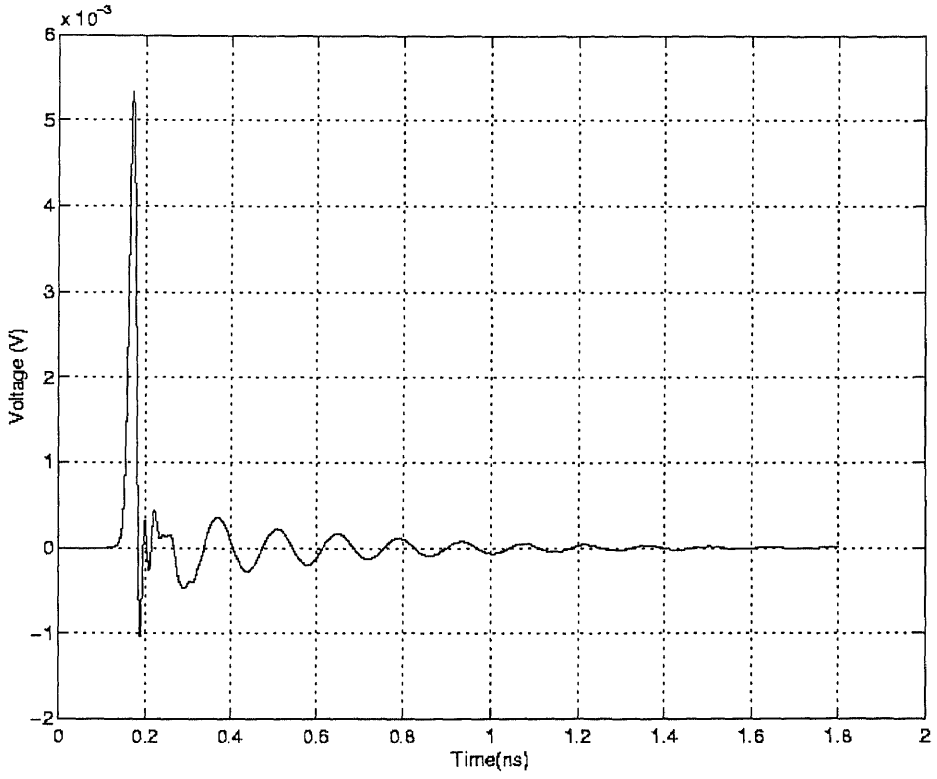

Figure 6.16 Voltage of total signal vs time of the impedance matching circuit shown in Figure 6.12.

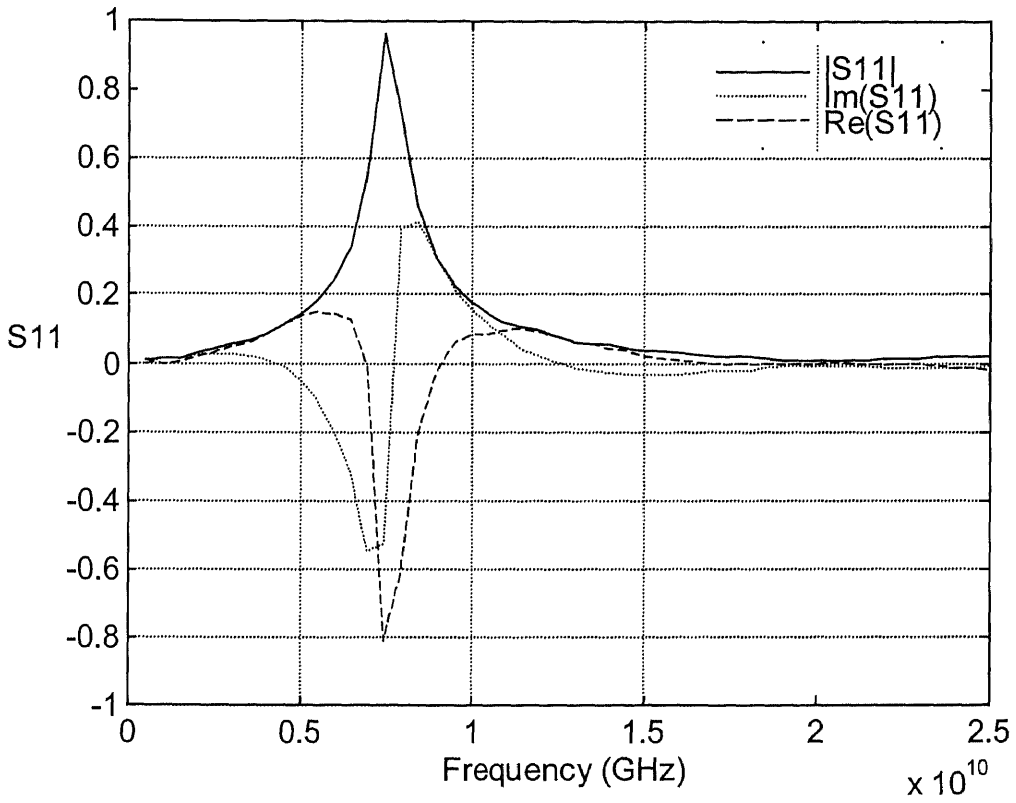

Figure 6.17 S11 diagram obtained directly from simulation to the impedance matching circuit shown in Figure 6.12

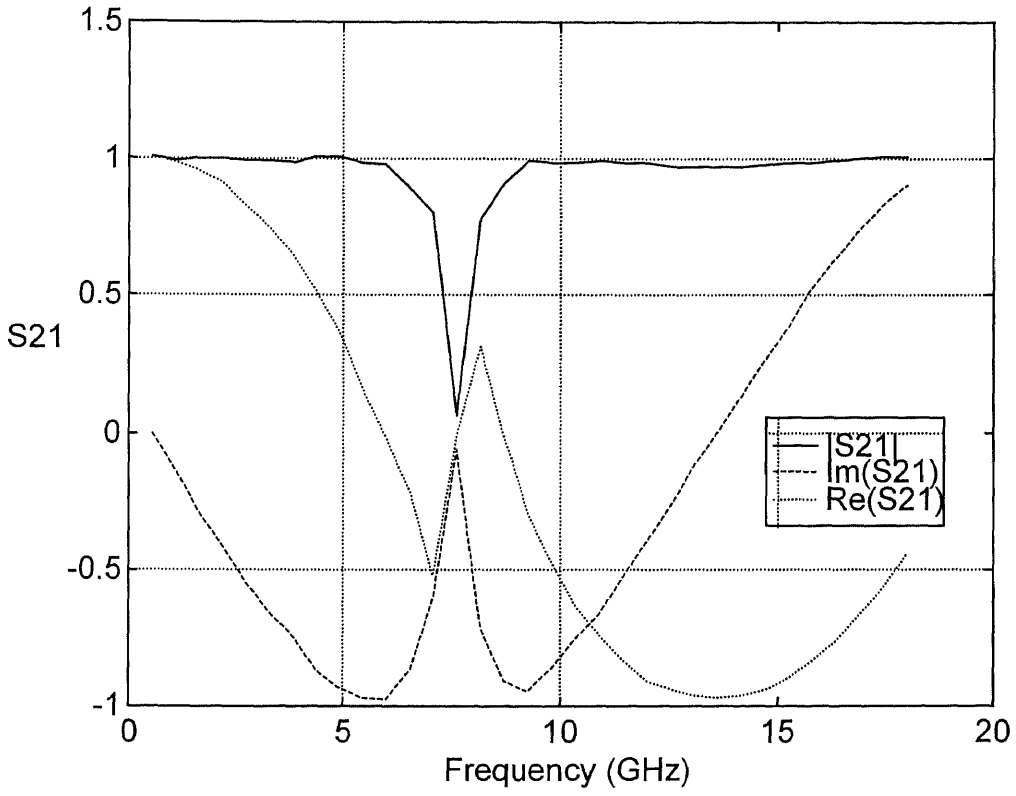

Figure 6.18 S21 diagram obtained directly from the co-simulation to the impedance matching circuit shown in Figure 6.12.

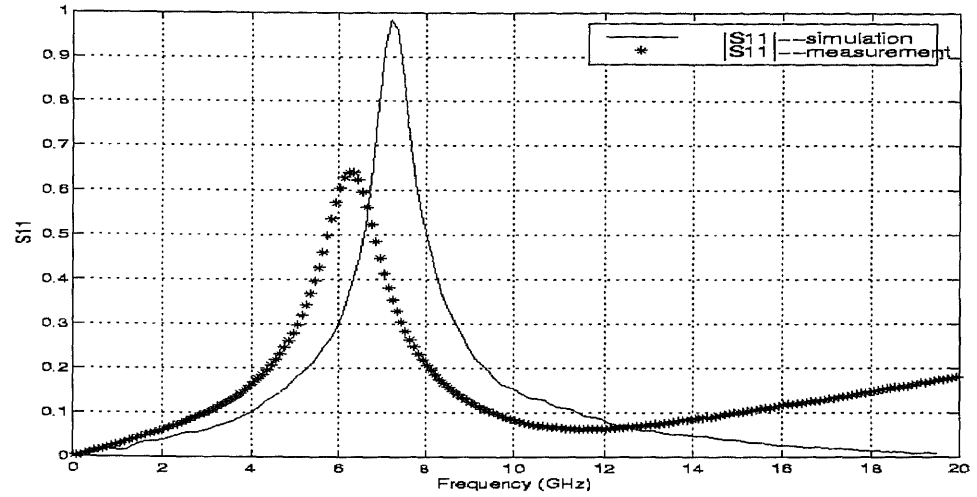

(a) Magnitude of S11

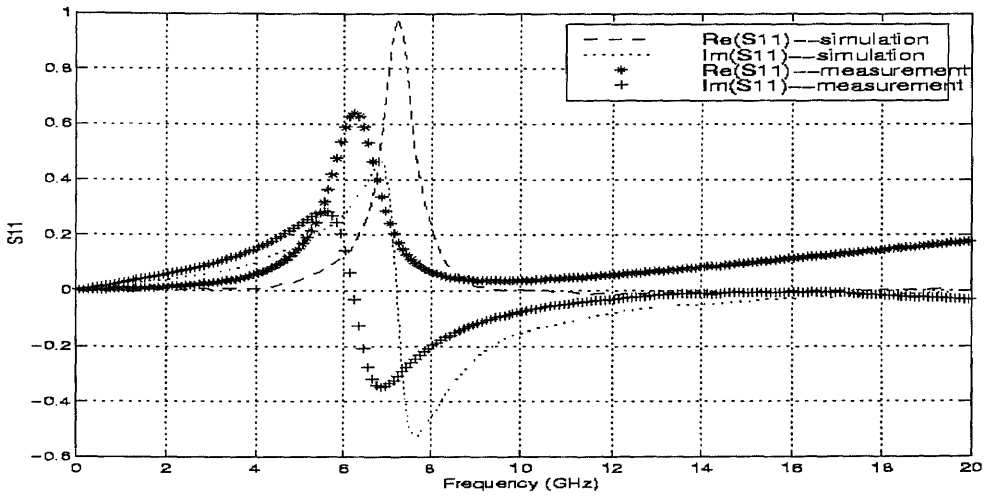

(b) Real and imaginary parts of S11

Figure 6.19 S11 diagrams of measurement and simulation results of the impedance matching circuit shown in Figure 6.12, and the latter is obtained after a phase compensation

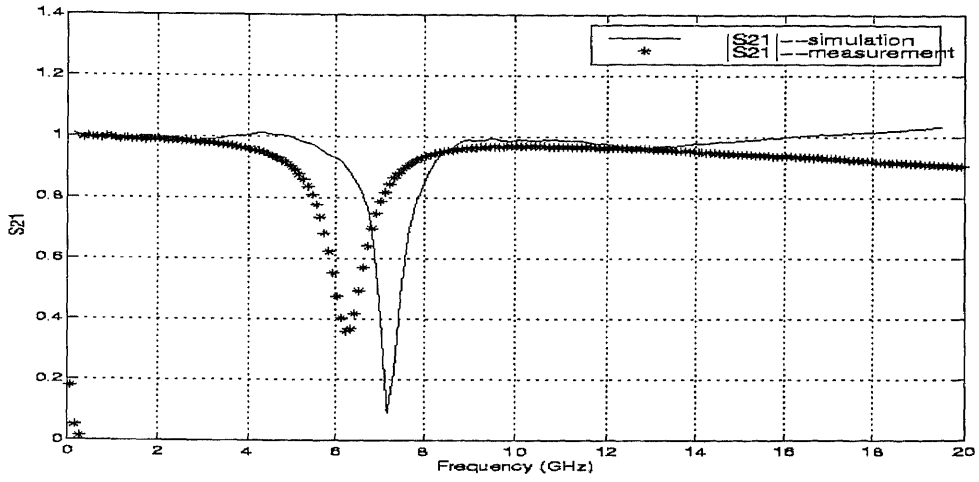

(a) Magnitude of S21

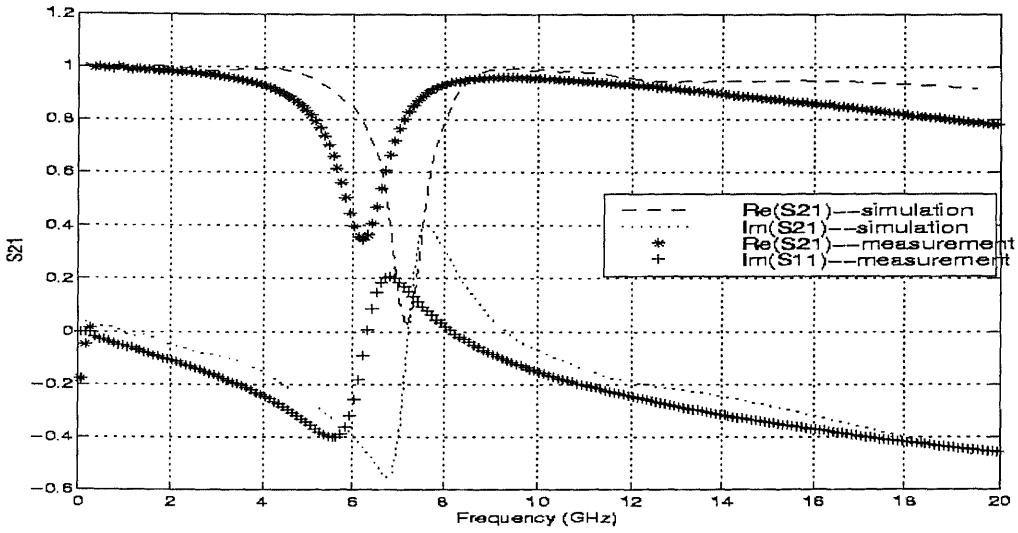

(b) Real and imaginary parts of S21

Figure 6.20 S21 diagrams of measurement and simulation results of the impedance matching circuit shown in Figure 6.12, and the latter is obtained after a phase compensation

time to be 10ns. The S11 parameters are obtained from the modified time-domain response.

Figure 6.17 shows the S11 parameters obtained directly from the time domain waveforms of Figures 6.15 and 6.16. Notice that although the magnitude of the simulation S11 value has the similar tendency compared with the measure result, as shown in Figure 6.19(a), the real and imaginary parts of S11 are quite different from the measurement results. The measurement results are shown in Figure 6.19(b).

The difference comes from the different observation points of the measurement and the simulation. The S parameters' measurement is performed by a network analyzer. The analyzer exerts an incident signal into the circuit and measures the reflection signal to compute the S parameters. The excitation position of the measurement may not be the same as that in the simulation and either does the observation point. Suppose that the observation points in the measurement and simulation are points A and B respectively. The distance between A and B is dl. Assume that the extended-out feeding line is a lossless transmission line and the effective wave phase speed is c in this transmission line. Because the S11 parameter is the reflection coefficient in port 1, the S11 parameters at points A and B have the following relation

$$S11(A) = S11(B)e^{j2\pi dl/c} \tag{6}$$

in which the single mode is assumed in the transmission line.

Given a certain value of dl/c, the S11 values in different positions can be obtained based on the S11 value in one position. The transformation by (6) does not change the magnitude of the S11 parameters, but the phase of the S11 parameter is changed in different places. In Figure 6.19(b), the real and imaginary parts of the simulation S11

values after a phase compensation of dl/c equal to 60ps, are basically matched to the measurement results.

Also, S21 parameters can be adjusted to match the measurement result in a similar manner. In Figures 6.18, the magnitude of S21 matches the measurement parameters, as shown in Figure 6.20(a), but the real and imaginary parts of S21 are quite different. Suppose that C and D are two points near port 2, S21 parameters at C and D points have the similar relation as (6)

$$S11(C) = S11(D)e^{j\omega dl/c} \tag{7}$$

By a certain value of dl/c, the phase of S21 can be compensated in different frequencies. In Figure 20(b), real value and imaginary parts of the simulation S21 results match the measurement results with a phase compensation of dl/c equal to 40ps.

In order to verify the effect of the lumped capacitor in the circuit, another simulation is done with the capacitor of doubled capacitance. Figure 6.21 shows the S11 parameters. Note in Figure 6.19, the center frequency is about 7.2GHz and in Figure 6.21 the one is about 5.2GHz. $(7.2/5.1)^2$ is about 2, which is equal the ratio of the capacitance in two simulations. This provides the consistence of our simulation.

The difference between the simulation measurement results is probably due to the connection between the probe and the circuit. This problem is still under investigation.

6.5. Band Gap Transmission Line Loaded with Plated Through Holes

Figure 6.22 shows a band pass filter made of a microstrip line with cylindrical holes between the metal strip. This is a multi-layered structure with different dielectric media as the substrate. The wall of every hole is coated by a very thin metal layer. In order to

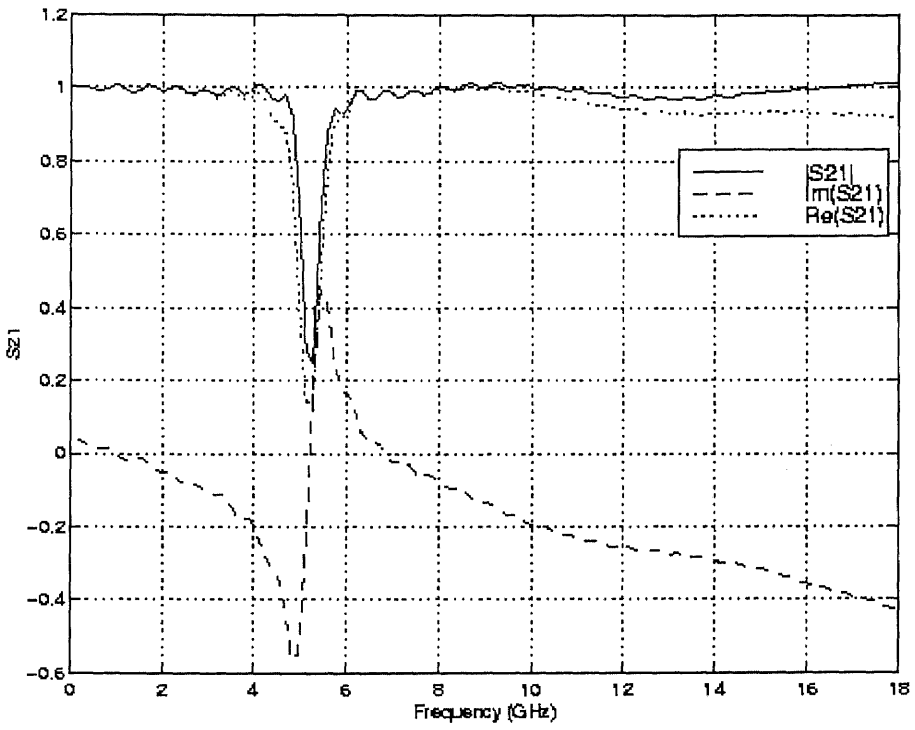

Figure 6.21 S11 of the impedance matching circuit shown in Figure 6.12 with a doubled lumped capacitor (C=2.7pF).

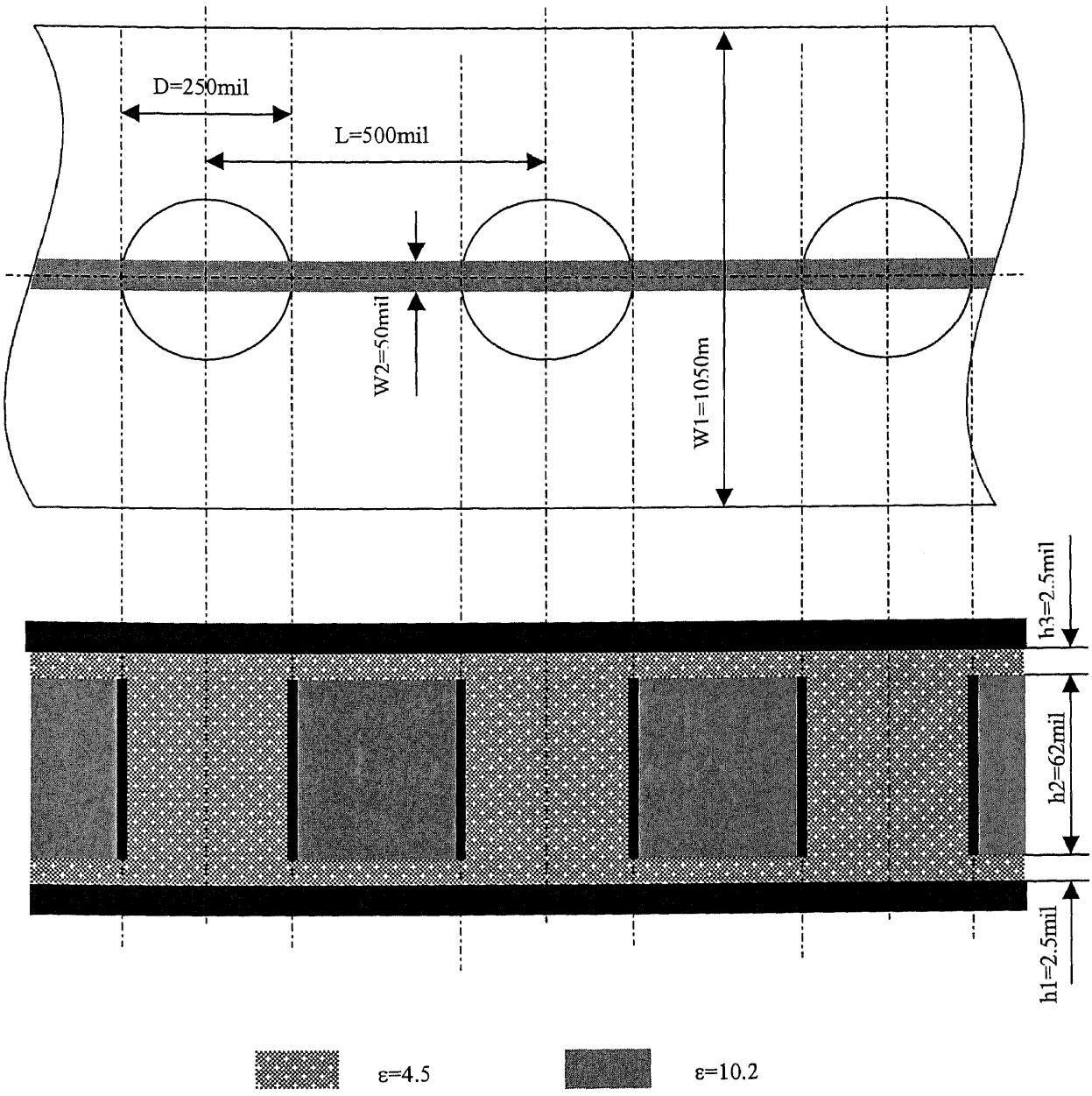

Figure 6.22 Micristrip band-pass filter with cylindrical holes through the substrate.

tune the pass band of this filter, varactor diodes are connected between the metal walls and the ground.

Our co-simulation model can be used to calculate the S parameter of the system. Two key problems have to be overcome to process the simulation, cylindrical thin metal wall and varactor modeling.

Thin metal wall

In order to perform a FDTD simulation to an EM structure, an appropriate model file to describe the construction of the structure is desired. Because the structure is discretized by a FDTD grid, the model file has to describe all Yee cells. Each Yee cell has its basic properties, such as permittivity, permeability and conductivity. In order to describe the PEC layer with zero thickness in the structure, an artificial property, which is called PEC type is defined as a property of Yee cell. The PEC property fixes some of the E components in a Yee cell to zero during all the computational time while other components are calculated by FDTD equations. Because there are three E components in one cell, there are 7 PEC types can be defined as below

Table 6.1 PEC Type of Yee Cells

PEC Type	Description
0	No components are fixed to zero
1	Ex=0
2	Ey=0
3	Ez=0
4	Ex=Ey=0
5	Ex=Ez=0
6	Ey=Ez=0
7	Ex=Ex=Ez=0

Once the PEC type is included into the model, any shape of the PEC layer can be described by the combination of all the cells with different PEC properties. With this modeling, the thickness of the very thin metal layer can be set to zero.

Staircasing is used to approximate the cylinder in the rectangular coordinates. The very thin metal cylindrical wall is treated as PEC layer.

Varactor modeling

The varactor diode is a nonlinear device and provides a voltage-dependent variable capacitance. Varactors are useful for many applications such as frequency tuning for active and passive circuits, frequency multiplication and parametric amplification.

The capacitance of a varactor is governed by the following expression [Chang, 1994]

$$C_j(V) = C_{j0}(1-\frac{V}{V_{bi}})^{-\gamma} \tag{8}$$

in which C_j is the junction capacitance, V_{bi} is the build-in voltage of the diode, V is the applied voltage, and g is a parameter depending on the doping profile. Normally, varactors operate under a negative bias condition.

The simple model of a varactor with a bias circuit is shown in Figure 6.23 (a). The capacitance of the varactor is decided by the bias voltage. If the bias voltage is much larger than the signal amplitude, the circuit can be simplified to a linear circuit shown in the dashed-line box in Figure 6.23(b).

The circuit in Figure 6.23(b) is the field-circuit model. The lumped current and lumped voltage can be obtained

$$V_{lumped}^{n+1} = \frac{I_{EM}(R_c + R_s) + V_C^n}{\frac{1}{R_{grid}}(R_{grid} + (R_s + R_c)(1+\frac{R_{grid}}{R}))} \tag{9}$$

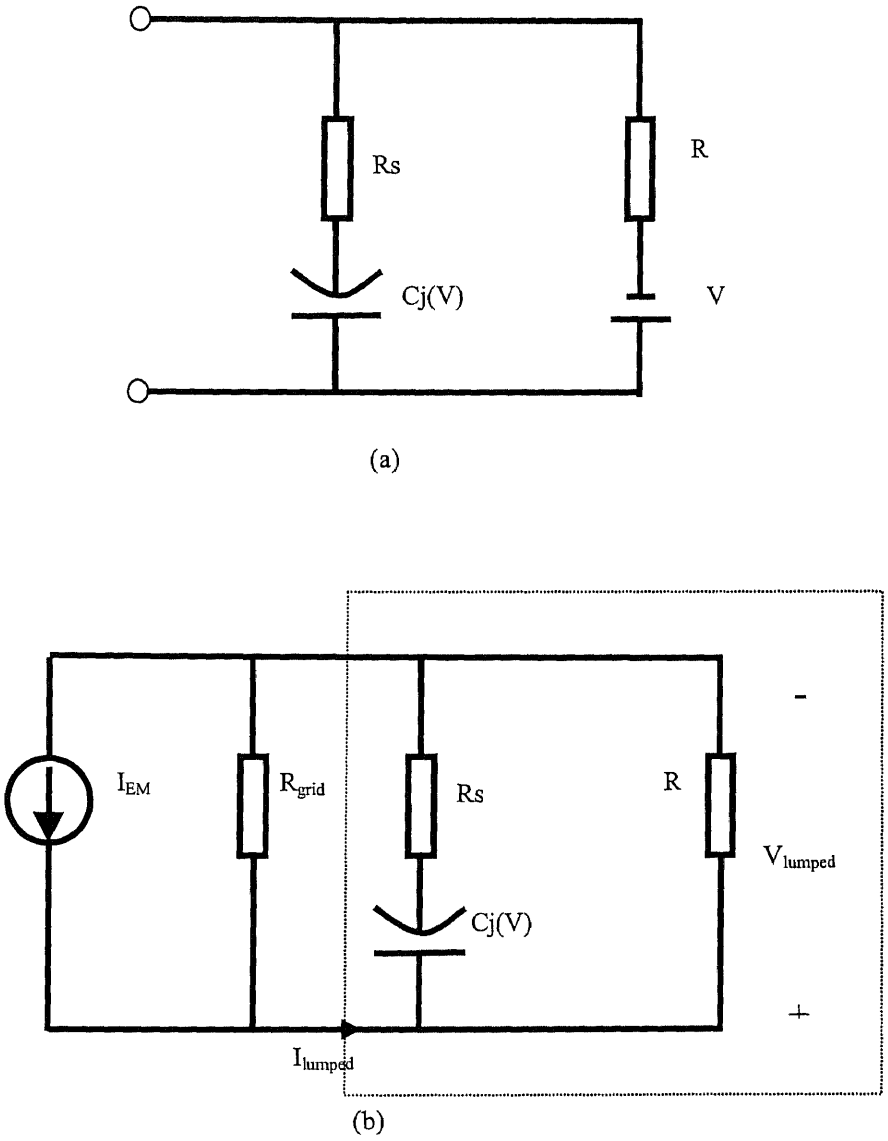

Figure 6.23 Varactor model in co-simulation. (a) simple varactor model with bias circuit. (b) field-circuit model in small AC signals. the circuit in the dashed box is the varactor and bias circuit.

$$V_C^{n+1} = \frac{V_{lumped}^{n+1} R_c + V_C^n R_s}{R_s + R_c} \tag{10}$$

in which Rc=dt/C. Once V_{lumped}^{n+1} is obtained, I_{lumped}^{n+1} can be obtained from (4.19).

In z direction, the FDTD grid is non-uniform, the smallest dz is 2.5mil and the biggest one is 10mil. In x and y directions, the grid is uniform, dx=dy=10mil. Time increment is 0.1058ps. PML boundary conditions are used in the simulation. There are 8 PML layers in each boundary.

Simulations are done to the filter structures with different number of holes and with or without varactors.

1. Three holes without varactors.

In this case, the comparison of the FDTD simulation results and the MoM simulation results done by IE3D are shown in Figure 6.24. Because in IE3D the dielectric media can only be defined in a layered structure, which means that within one layer, there is only one permittivity value allowed. Thus in IE3D simulation, the media inside cylinder has the same permittivity as that of outside, which is 10.2. By IE3D, about four hours were used to calculate the S parameters for one frequency. Totally, the simulations were performed at 20 frequency points. The two simulation results show good agreement.

In Figure 6.25, a FDTD simulation result with ε=4.5 inside the cylinder are compared with the FDTD result in Figure 6.24. It shows that the different electrical dielectric media perform a tuning function.

The computational time for FDTD simulations are about 10 hours on Ultra 60 workstation.

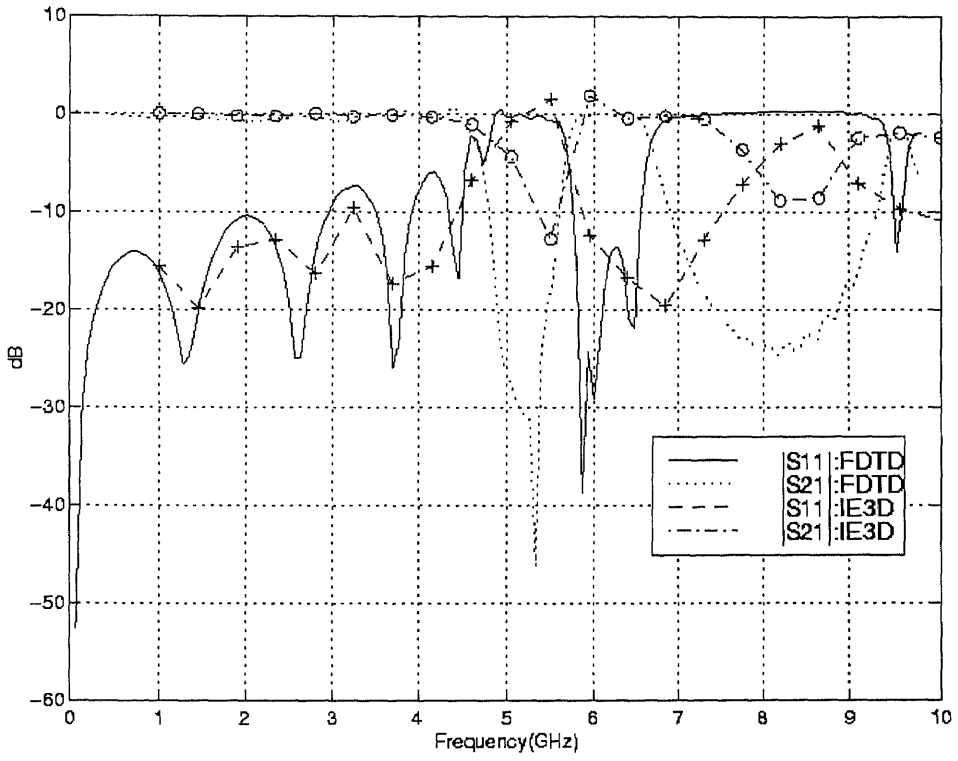

Figure 6.24 Comparison of the FDTD and IE3D simulation to Micristrip band-pass filter with 3 cylindrical holes through the substrate. 'o' and '+' points are the results from IE3D.

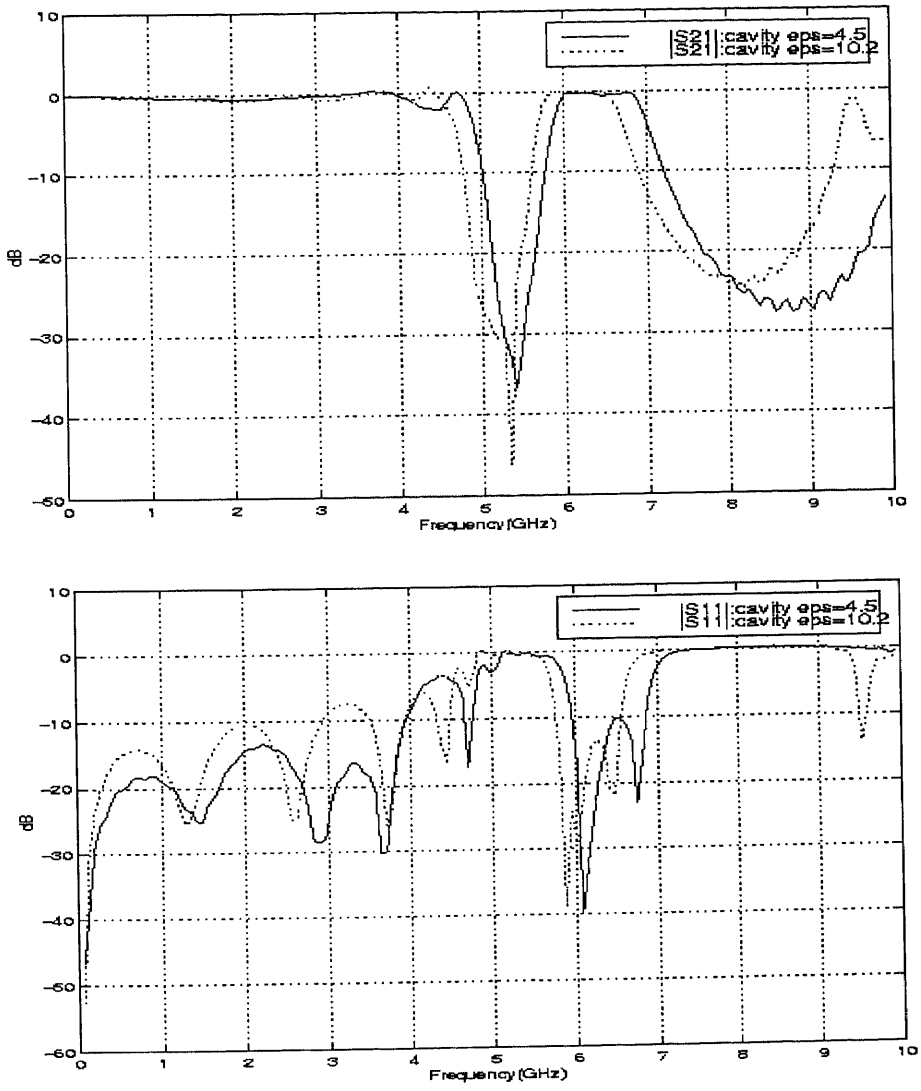

Figure 6.25 The FDTD simulation results of microstrip band-pass filter with three cylindrical holes through the substrate. It shows that the different dielectric media in the cylinder has the tuning function

2. Three holes with varactors

In this case, there is a varactor connected between the bottom of the metal wall of each cylindrical hole and the metal ground. In the small signal equivalent circuit shown in Figure 6.23 (b), Cj=7pF, Rs=0.3Ω, R=10kΩ. Figure 6.26 shows that the varactors embedded in the filter has much stronger tuning functions than that caused by the different dielectric media in the holes. Thus by adjusting the bias voltage of the varactors, it is very flexible to change the passband of the filter.

3. Seven holes without varactors

Figures 6.27 shows the co-simulation results of the filters with seven holes and three holes respectively. It shows that the number of the holes has slight influence on the pass band of the filter.

The design and analysis of the filter is still going on.

6.6. Conclusion

In this chapter, several simulations are utilized to show the field-circuit co-simulation model in full wave three-dimensional simulation. Especially in the spiral impedance matching circuit analysis, the very small physical size makes a big challenge to the simulation in terms of the grid configuration, PML construction and comparison between the measurement and simulation results. From the presented simulation examples, we can conclude that our co-simulation model has potential to simulate EM systems with more complicated lumped elements and distributed structures. Also, some important aspects about the lumped characteristic extraction from the co-simulation are presented. Although these points do not belong to the simulation itself, they make the simulation

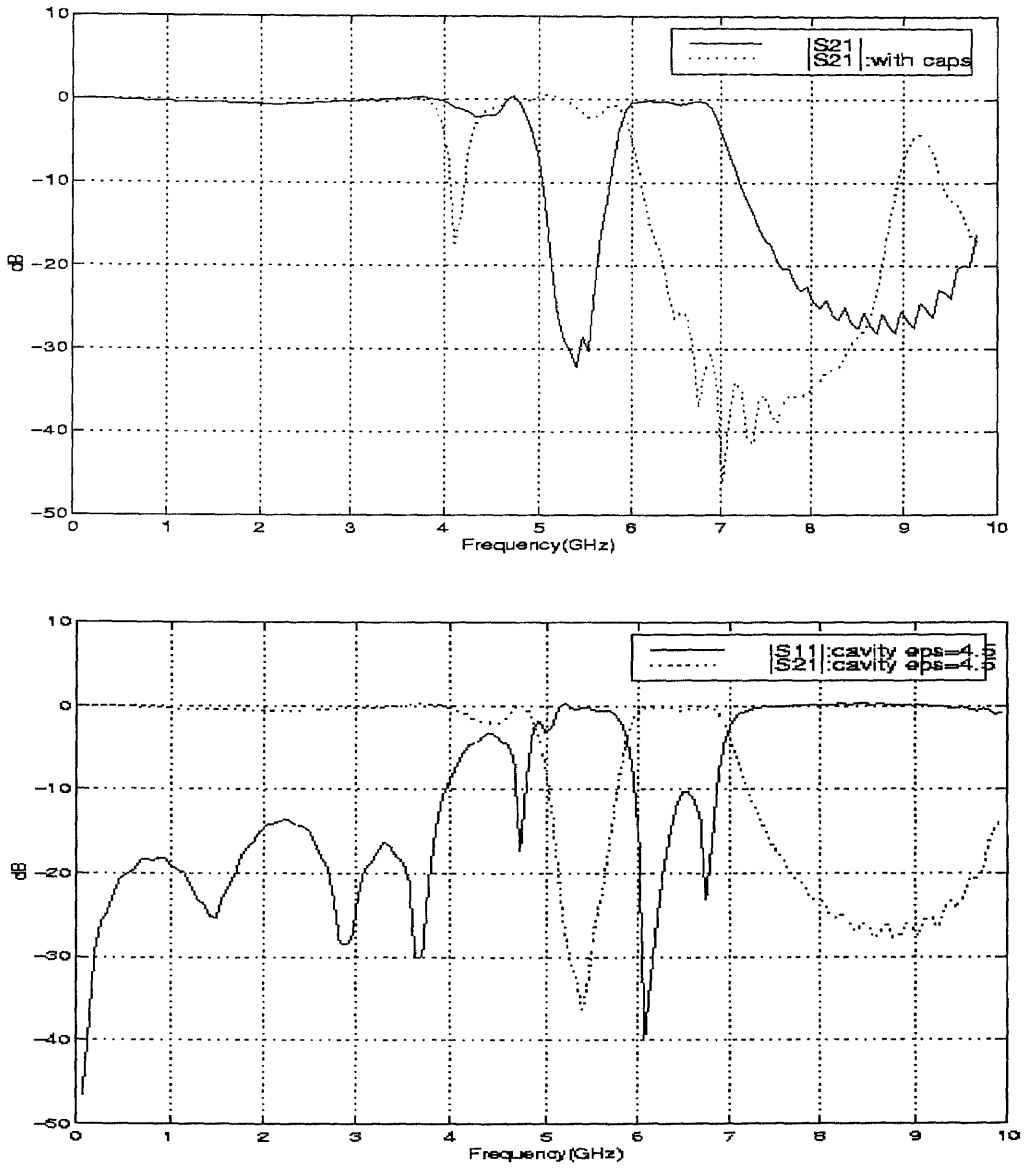

Figure 6.26 The co-simulation results of microstrip band-pass filter with three cylindrical holes through the substrate. It shows that the varactors in the filter has the tuning function

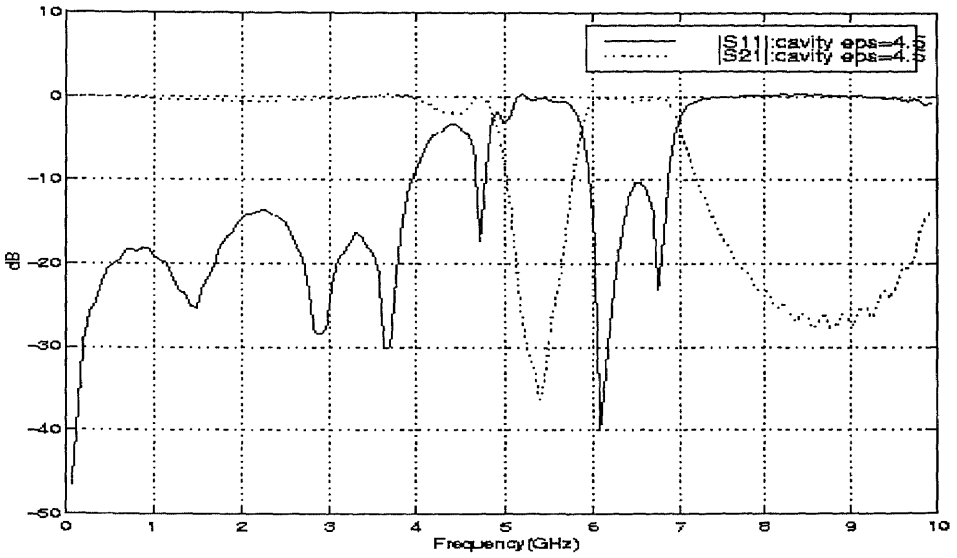

(a)

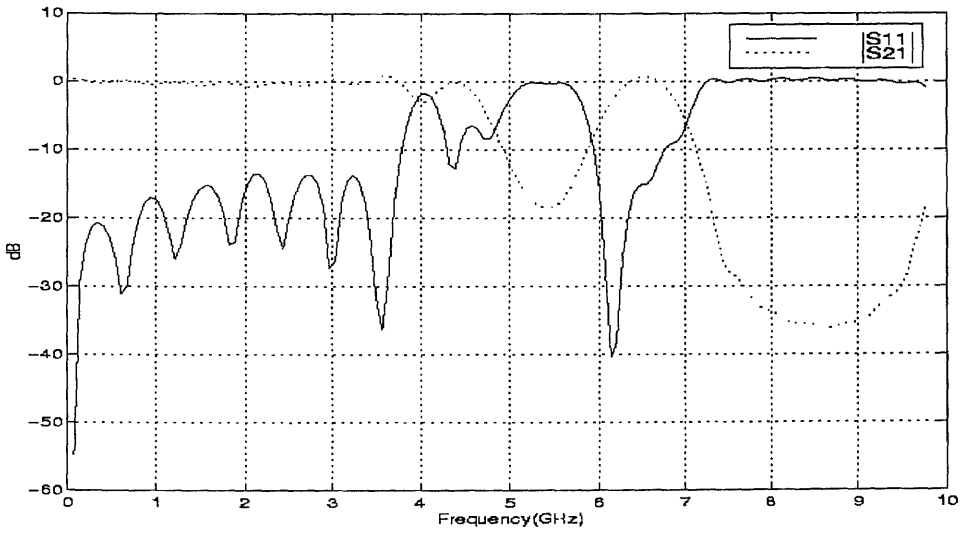

(b)

Figure 6.27 The FDTD simulation results of microstrip band-pass filter with three (a) and seven (b) cylindrical holes through the substrate.

useful in system modeling, analysis, and design. These examples build up a confidence to further improve co-simulation model to simulate industrial products.

CHAPTER 7

CONCLUSION

7.1. Contributions of the Dissertation

This dissertation is dedicated to the finite-difference time-domain (FDTD) simulation for hybrid EM systems consisting of distributed structures and embedded lumped elements.

A fundamental simulation model, called field-circuit co-simulation model, is proposed to provide an interface between FDTD and circuit simulation. By this method, the simulation of a hybrid system can be processed in a systematic manner regardless of the number and type of lumped elements in the system. This feature is promising for building an FDTD-based general full-wave simulation package for hybrid EM systems.

The proposed field-circuit model separates FDTD and circuit simulation into two independent processes with information exchanging between them and it contributes to the flexibility of the co-simulation model. In FDTD, the influence of a lumped element on its surrounding EM field is represented by a lumped current that is an additional current component in the Maxwell's equations. No component of the lumped element appears in the FDTD equations other than the lumped-current term mentioned above. In the circuit simulation, the effects of EM field on the lumped element are represented by two equivalent circuit components contributed by the EM field. Therefore, the interaction between the lumped element and its surrounding EM field is represented by a kind of leapfrog processes. FDTD calculates the field distribution with the lumped elements present, generates information to the circuit simulation, and then waits for the circuit simulator's response. The circuit simulator receives the necessary data from FDTD,

solves the circuit, and sends the results to FDTD. Thus both FDTD and circuit simulation can solve their problems independently with information exchange and benefit from their mature techniques.

A simulation package is developed to implement the field-circuit co-simulation model in three dimensions. For circuit simulation, a small circuit simulator is developed to handle some commonly used lumped elements and their combinations. In FDTD, the package utilizes the non-uniform rectangular FDTD grid with PML boundary conditions to simulate the EM field. An object-oriented programming language, C++ in this dissertation, is used to design such a program with two relatively independent simulations.

Because the 3D co-simulation of a practical EM system, which may have complicated structure, demands high-performance FDTD simulation, some important aspects about FDTD are discussed in this dissertation.

The FDTD numerical errors have critical influence on the accuracy of the co-simulation results, especially for the structure with inhomogeneous media. The FDTD numerical reflection coefficient and numerical transmitting angle on the interface of two media, which have not been presented in a non-uniform FDTD grid, are derived to provide a fundamental estimation of numerical errors. Based on the estimation of FDTD numerical reflection coefficient, the non-uniform FDTD cell size can be adjusted to avoid serious numerical errors especially in the 3D FDTD simulation. Although results are obtained for relatively simple cases, they provide important information to improve the accuracy of the FDTD simulation for some complicated structures.

Berenger's PML boundary conditions are extended and implemented into the inhomogeneous boundaries and non-uniform FDTD grid. A geometric loss profile is utilized in the PML layer. In the proposed PML, each of the six boundaries of the three-dimensional computational domain has its own PML parameters. Therefore, this approach provides the flexibility to manipulate the PML layers to achieve higher accuracy and lower computational cost.

As test cases to verify the proposed approach, a number of hybrid systems are simulated using the field-circuit co-simulation model in the two or three-dimensional domain. The excellent agreements between the two-dimensional simulation and SPICE results validate the field-circuit co-simulation model. The comparison of the results between three-dimensional co-simulations and the measurement results demonstrates that this model can be used into the design of practical hybrid systems.

Some issues about the extraction of lumped characteristics, such as S parameters, from the FDTD simulation are addressed. Some modifications to the original circuit are necessary for many circuits if one expects to extract S parameters from FDTD simulation results. Post process of the simulation result has to be performed to match the simulation and measurement results. In case that the original circuit is modified by adding a very long feeding line, it is efficient to use a non-uniform FDTD grid.

7.2. Limitations and Future Work

Our co-simulation package focuses on the modeling of the interaction between the EM field and lumped elements. Although in this dissertation some relatively small hybrid systems are solved to demonstrate its validation and implementation, the field-circuit co-

simulation model can be utilized to general cases. General co-simulation needs to include more extensions in both FDTD and circuit simulation due to the complexity of the practical systems and the inherent high computational cost of FDTD.

The future work to improve the co-simulation package can be divided into three categories, co-simulation related topics, FDTD related topics, and post process of the simulation results.

The co-simulation related topics include handling the simulation process and modeling lumped elements. In order to implement the FDTD based hybrid co-simulation model for practical systems, the intensive computational burden of FDTD has to be overcome. One of the effective approaches is to distribute the computational burden to multi-microprocessors by a parallel-computing scheme. The co-simulation package developed is in series-computing manner. Based on the proposed co-simulation model, it can be updated to a parallel-computing simulation package, specifically, the circuit simulation can be a parallel process to the FDTD process, and the FDTD process can be divided into several concurrent sub-processes.

Instead of our simple lumped circuit solver that can only solve some simple lumped systems, a general circuit solver like SPICE has to be introduced into the co-simulation code to solve circuits that are more complicated. An interface has to be built up to transfer information between SPICE and FDTD process. The SPICE package connected with the FDTD code will release our burden to model and solve some complicated circuits.

The lumped elements modeled in this dissertation are the one-port lumped elements. Multiple-port lumped elements have to be modeled. Although there are publications

about these elements [Thomas and Ling et al 1994, Thomas and Jones et al 1994], the model is not well posed. Especially the treatment of the area between the ports is essentially empirical or based on numerical experiments. A general model for the multiple-port lumped elements would be the most challenging aspect of the hybrid system modeling.

The second category of future work is the investigation of the FDTD method.

In order to generate a more general FDTD-based co-simulation package, many FDTD topics have to be further studied. The inhomogeneous PML boundary conditions have to be investigated to provide a general approach to build an optimized PML layer for very-long-time simulations. The PML boundary conditions for lossy media have to be included in a package for some applications. Some important material models, such as very thin dielectric layer, SIBC, nonlinear and anisotropic media, have to be studied. The generalized FDTD grid can be utilized to extend our model to general situations. There are many topics about the FDTD method and each of them has been studied by many researchers. To utilize our co-simulation in practical systems, all forthcoming improvements of FDTD can be included into our package because of the flexibility and robustness provided by the field-circuit model.

The third category is the post processing of the simulation data. In the present package, the post processes, including discrete Fourier transform (DFT) process and result display, are done by Matlab separately and it should be expanded and included into the package. The auto-regressive (AR) or neural network (NN) model can be a part of the post process to predict the simulation results for reducing execution time. More DFT

techniques can be used to generate the spectrum responses accurately. 2D and 3D displays are also very important to this simulation to get visualization of an EM process.

This dissertation and its future work are to develop a full wave package to simulate hybrid EM systems. The proposed field-circuit co-simulation model is essential to achieve this purpose. It is flexible enough to benefit from any improvements in both circuit simulation and FDTD. We believe that a fully developed co-simulation package will play an important role in the design and analysis of high-performance RF and microwave systems.

REFERENCE

1. Bahr, A., Lauer, A., and Wolff, I. "Application of the PML absorbing boundary condition to the FDTD analysis of microwave structures," *IEEE MTT-S Digest*, pp. 27-30, 1995.

2. Bayliss, A. and Turkel, E., "Radiation boundary conditions for wave-like equations," *Comm Pure Appl. Math.*, vol. 23, pp. 707-725, 1980.

3. Berenger, J. P. "Numerical reflection of evanescent waves from perfectly matched layers," *IEEE Antennas and Propagat. Soc. Int. Symp.* vol. 3, pp. 1888—1891, July, 1997.

4. Berenger, J. P. "Perfectly matched layer for the FDTD solution of wave-structure interaction problems," *IEEE Trans. on Antennas Propagat.,* vol. 44, no. 1, Jan. 1996.

5. Berenger, J. P. "A perfectly matched layer for the absorption of electromagnetic waves," *Journal of Computational Physics* 114, pp. 185-200, 1993.

6. Bing, W. "Impendance characteristics of a Ka-band MMIC active microstrip antenna suing FDTD method," *IEEE Antennas and Propagat. Soc. Int. Symp.*,vol. 3, pp. 1574-1577, Jul. 1997

7. Chang, K. *Microwave Solid-State Circuit and Applications,* New York: Wiley, 1994.

8. Chen, J., Elshebeni, A. Z., Smith, C. E. and Ahmat-Samii, Y. R. "FDTD analysis of printed square soiral antennas for wireless communications," *IEEE Antennas and Propagat. Soc. Int. Symp.,* vol. 3, 1550-1553, Jul. 1997.

9. Chen, J., Wu, C., Lo, T. K. Y., Wu, K. L. and Livta, J. "Using linear and nonlinear predictors to improve the computational efficiency of the FDTD algorithm," *IEEE Trans. Microwave Theory Tech.* vol. 42, no. 10, pp. 1992-1997, Oct. 1994.

10. Chen, M. Deal, W. R., Houshmand, B. and Itoh, T. "Global time-domain full-wave analysis of microwave FET oscillators and self-oscillating mixers", *IEEE MTT-S Digest*, pp. 1135-1138, 1998.

11. Chen, M., Chew, S. T. and Itoh, T. "Nonlinear analysis of a microwave diode mixer using the extended FDTD", *IEEE MTT-S Digest*, pp. 67-70, 1997.

12. Chen, Z. and Xu, J. "The generalized TLM-based FDTD modeling of frequency-dependent and anisotropic media," *IEEE Trans. Microwave Theory Tech.* vol. 46, no. 5, pp. 561-565, May 1998.

13. Chew, W. C. and Jin, J. M. "Perfectly matched layers in the discretized space: An analysis and optimization," *Electromagnetics,* vol. 5, no. 4, pp. 325-340, Jul. 1996.

14. Choi, D. H. "A comparison of the dispersion characteristics associated with the TLM and FDTD methods," *International Journal of Numerical Modelling*, 2, pp. 203-214, 1989.

15. Ciampolini, P., Mezzanotte, P., Roselli, L. and Sorrentino, R. "Actuate and efficient circuit simulation with lumped-element FDTD technique," *IEEE Trans. Microwave Theory Tech.* vol. 44, no. 12, pp. 2207-2215, Dec. 1996.

16. De Moerloose, J. and Stuchly, M. A. "Behavior of Berenger's ABC for evanescent waves," *IEEE Microwave and Guided Wave Lett.,* vol. 5, no. 10 pp. 344-346, Oct. 1995.

17. Durney, C. H., Sui, W., Christensen, D. A. and Zhu, J. " A general formulation for connecting sources and passive lumped-circuit elements across multiple 3_D FDTD cells," *IEEE Microwave and Guided Wave Lett.*, vol. 6, no. 2, pp. 85-87, Feb. 1996.

18. Engquist, B. and Majda, A. "Absorbing boundary conditions for the numerical solution of waves," *Mathematics of Computational,* vol. 31, pp. 629-651, 1977.

19. Fang, J. "Absorbing boundary conditions applied to model wave propagation in microwave integrated-circuits," *IEEE Trans Microwave Theory Tech.* vol. 42, no. 8, Aug. 1994.

20. Fang, J. and Wu, Z. "Closed-form expression of numerical reflection coefficient at PML interfaces and optimization of PML performance," *IEEE Microwave and Guided Wave Lett.,* vol. 6, no. 9, pp. 332-335, Sept. 1996.

21. Fang, J. "Time domain finite difference computation for Maxwell's equations," *Ph. D Thesis,* University of California at Berkeley, 1989.

22. Farias, R. G. and Giarola, A. J. The use of FDTD for the analysis of magnetoplasma channel waveguides," *IEEE Trans Microwave Theory Tech.* vol. 46, no. 4, pp. 387-394, Apr. 1997.

23. Gedney, S. D., Lansing, F. S. and Rascoe, D. L. "Full wave analysis of microwave monolithic circuit devices using a generalized Yee-algorithm based on an unstructured grid," *IEEE Trans Microwave Theory Tech.* vol. 44, no. 8, Aug. 1996.

24. Gwarek, W. K. and Celuch-Marcysiak, M. "A differential method of reflection coefficient extraction from FDTD simulations," *IEEE Microwave and Guided Wave Lett.,* vol. 6, no. 5, pp. 215-217, May 1996.

25. Higdon, R. L. "Numerical absorbing boundary conditions for the wave equation," *Mathematics of Computation*, vol. 49, pp65-90, 1987.

26. Holland, R. "Finite difference solution of Maxwell's equations in generalized nonorthogonal coordinates," *IEEE Trans. On Nuclear Science,* vol. 30, no. 6, pp. 4589-4591, Dec. 1983.

27. Holland, R. "THREDS: a finite defference time domain EMP code in 3D spherical coordinates," *IEEE Trans. on Nuclear Science*, vol. 30, no. 6, pp. 4592-4594, Dec. 1983.

28. Holland, R. "Total-field versus scattered field finite difference codes: a comparative assessment," *IEEE Trans. on Nuclear Science,* vol. 30, no. 6, pp. 4583-4588, Dec. 1983.

29. Houshmand, B., Itoh, T. and Piket-May, M. *Advances in Computational Electrodynamics: The Finite-Difference Time-Domain Method*, Boston: Artech House, 1998.

30. Jandhyala, A., Michielssen, E. and Mittra, R. "FDTD signal extrapolation using the forward-backward autoregressive (AR) model," *IEEE Microwave and Guided Wave Lett.* Vol. 4, no. 6, pp. 163-165, Jun. 1994.

31. Itoh, T. and Houshmand, B. *Time-Domain Methods for Microwave Structures: Analysis and Design,* Piscataway, NJ: IEEE Press, 1998.

32. Jou, C. F. et al "Millimeter wave diode grid frequency doubler," *IEEE Trans. Microwave Theory Tech.* vol. 36, no. 11, pp. 1507-1514, 1988.

33. Katsibas, K. D., Balanis, C. A., Tirkas, P. A. and Birtcher, C. R. "Folded loop antenna for mobil hand-held units, " *IEEE Antennas and Propagat.*, vol. 46, no. 2, pp. 260-266, Feb. 1998.

34. Katz, D. S., Thiele, E. T. and Taflove, A. "Validation and extension to three dimensions of the Berenger PML absorbing boundary condition for FD-TD meshes," *IEEE Microwave and Guided Wave Lett.* vol. 4, no. 3, pp. 268-270, Aug. 1994.

35. Kim, I. S. and Hoefer, W. J. R. "Numerical dispersion characteristics and stability factor for the TDFD method," *Electronics Letters*, 26, 7, pp. 485-487, 1990.

36. Kollberg, E. L. *Microwave and Millimeter-Wave Mixers*, Piscataway, NJ: IEEE Press, 1984.

37. Kunz, K. S. and Luebbers R. J., *The finite difference time domain method for electromagnetics,* Boca Raton, FL: CRC Press, 1993

38. Kuo, C., Houshmand, B. and Itoh, T. "Full-wave analysis of packaged microwave circuits with active and nonlinear devices: An FDTD approach," *IEEE Trans Microwave Theory Tech.* vol. 45, no. 5, pp. 819-826, May 1997.

39. Kuo, C. N., Wu R. B., Housmand. B. and Itoh, T. "Modeling of microwave active devices using the FDTD analysis based on the voltage-source approach," *IEEE Microwave and Guided Wave Lett.*, vol. 6, no. 5, pp. 199-201, May. 1996.

40. Kuo, C., Thomas, V. A., Chew, S. T., Houshmand, B. and Itoh, T. "Small signal analysis of active circuits using FDTD algorithm," *IEEE Microwave and Guided Wave Lett.* vol. 3, no. 7, pp. 216-218, Jul. 1995.

41. Lau, Y. C., Leong, M. S. and Kooi, P. S. "Extension of Berenger's PML boundary condition in matching lossey medium and evanescent waves," *Electronic Letters,* vol. 32, No. 11, pp. 974-976, 1996.

42. Li, T., Sui, W. and Zhou, M. "A novel field-circuit model for hybrid system co-simulation," submitted to *IEEE Transaction on MTT.*

43. Liao, Z. P., Wong, H. L., Yang, B. P. and Yuan, Y. F. "A transmitting boundary for transcient wave anlyses, " *Scienta Sinica (series A),* vol. XXVII, pp. 1063-1076, 1984.

44. Lo, T. K. and Hwang, Y. M. "A method of implementing a probe for microstrip antennas with subcell spatial adjustment in FDTD," *IEEE Antennas and Propagat. Soc. Int. Symp.,* vol. 3, pp. 1554-1557, Jul. 1997.

45. Madsen, N. K. and Ziolkowski, R.W. "A three-dimensional modified finite volume technique for Maxwell's equations," *Electromagnetics* 10:147-161, 1990

46. Marple, L. "A new autoregressive spectrum analysis algorithm," *IEEE Trans. Acoustics, Speech and Signal Processing,* vol. ASSP-20, No. 4, Aug. 1980.

47. Mass, S. A. *Nonlinear Microwave Circuits*, Piscataway, NJ: IEEE Press, 1997.

48. Mei, K. K. and Fang, J. "Superabsorption - a method to improve absorbing boundary conditions," *IEEE Trans. on Antennas Propagat.,* vol. 40, pp. 1001-1010, 1992.

49. Meskanen, H. and Pekonen, O. "FDTD analysis of field distribution in an elevator car by using various antenna positions and orientations," *Electron. Lett.,* vol. 34, no. 6, pp. 534-535, Mar. 1998.

50. Misra, I. S. and Chowdhury, S. K. "Study of impedance and rediation properties of a concentric microstrip triangular-ring antenna and its modeling techniques using FDTD method," *IEEE Trans. on Antennas Propagat.,* vol. 46, no. 4, pp. 531-537, Apr. 1998.

51. Mittra, R. and Pekel, U. "A new look at the perfectly matched later (PML) concept for the reflectionless absorption of electromagnetic waves," *IEEE Microwave and Guided Wave Lett.,* vol. 5, no. 3, Mar. 1995.

52. Monk, P. and Suli, E. "Error estimates for Yee's method on non-uniform grids," *IEEE Trans. on Magnetics*, vol. 30, no. 5, Sept. 1994.

53. Mur, G. "Absorbing boundary conditions for the finite-difference approximation of the time-domain electromagnetic field equations," *IEEE Trans, Electromagnetic compatibility*, vol. EMC-23, pp. 377-382, Nov. 1981.

54. Oguz, U. and Gurel, L. "Subsurface-scattering calculations via the 3D FDTD method employing PML ABC for layered media," *IEEE Antennas and Propagat. Soc. Int. Symp.*, vol. 3, pp. 1920-1923, Jul. 1997.

55. Petropoulos, P. G. "Phase error control for FDTD methods of second and fourth order accuracy," *IEEE Trans. Antennas Propagat.*, vol. 42, no. 6, pp. 859-862, Jun. 1994.

56. Pereda, J. A., Garcia, O., Vages, A. and Prieto, A. "Numerical dispersion and stability analysis of the FDTD technique in lossy dielectrics," *IEEE Microwave and Guided Wave Lett.*, vol. 8, no. 7, Jul. 1998.

57. Piket-May, M., Taflove, A. and Baron, J. "FDTD modeling of digital signal propagation in 3-D circuits with passive and active loads," *IEEE Trans. Microwave Theory Tech.* vol. 42, no. 8, pp. 1514-1523, Aug. 1994.

58. Pillai, E. R. "Coax via--a technique to reduce crosstalk and enhance impedance match at vias in high-frequency multilayer packages verified by FDTD and MoM modeling," *IEEE Trans Microwave Theory Tech.* vol. 45, no. 10, pp. 1981-1985, Oct. 1997.

59. Polycarpou, A. C., Tirkas, P. A. and Balanis, C. A. "The finite-element method for modeling circuits and interconnections for electronic packaging," *IEEE Trans Microwave Theory Tech.* vol. 45, no. 10, pp. 1868-1874, Oct. 1997.

60. Reuter, C. E., Joseph, R. M., Thiele, E. T., Katz, D. S. and Taflove, A. "Ultrawideband absorbing boundary condition for termination of waveguiding structures in FD-TD simulations," *IEEE Microwave and Guided Wave Lett.*, vol. 4, no. 10, Oct. 1994.

61. Reuter, C. E., Joseph, R. M., Thiele, E. T., Katz, D. S. and Taflove, A. "Ultrawideband termination of waveguiding and multilayer structures for FD-TD simulations in 2D and 3D," *11th Annual Review of Progress in Applied Computational Electromagnetics*, vol. 1, pp. 476-481, 1995.

62. Roselli, L., Tentzeris, E. M. and Katehi, L. P. B. "Nonlinear circuit characterization using a multiresolution time domain technique (MRTD)," *IEEE MTT-S Digest*, pp. 1397-1400, 1998.

63. Sheen, D. M. S., Ali, M., Abouzahra, M. D. and Kong, J. A. "Application of the threed-dimensional finite-difference time-domain method to the analysis of planar microstrip circuits," *IEEE Trans. Microwave Theory Tech.* vol. 38, no. 7, pp. 849-857, Jul. 1990

64. Shlager, K. L. and Schneider, J. B. "A selective survey of the finite-difference time-domain literature," *IEEE Trans. Antennas Propagat.*, vol. 37, no. 4, pp. 39-57, Aug. 1995.

65. Shlager, K. L., Maloney, J. G., Ray, S. L. and Peterson, A. F. "Relative accuracy of several finite-difference time-domain methods in two and three dimensions," *IEEE Trans. Antennas Propagat.*, vol. 41, no. 12, pp. 1732-1737, Dec. 1993.

66. Spillard, C., Pennock, S. R. and Shepherd, P. R. "Absorbing boundary conditions for the modeling of scattering in parallel-plate transmission media," *IEEE Microwave and Guided Wave Lett.*, vol. 5, no. 8, Aug. 1995.

67. Sui, W. "Finite-difference time-domain solutions to Maxwell's equations including interactions with lumped elements, charged-particle fluids and gain media", *Ph.D. dissertation*, University of Utah, Salt Lake City, 1996.

68. Sui, W., Christensen, D. A. and Durney, C. H. " Extending the two-dimensional FDTD method to hybrid electromagnetic systems with active and passive lumped elements," *IEEE Trans. Microwave Theory Tech.* vol. 40, pp. 724-730, Apr. 1992.

69. Sullivan, D. A. "three dimensional optical fiber simulation," *IEEE Antennas and Propagat. Soc. Int. Symp.*, vol. 1, pp. 368-371, Jul. 1997.

70. Sullivan, D. M. "A simplified PML for use with the FDTD method," *IEEE Microwave and Guided Wave Lett.*, vol. 6, no. 2, pp. 97-99, Feb. 1996.

71. Taflove, A. *Advances in Computational Electrodynamics, The Finite-Difference Time-Domain Method,* Boston: Artech House, 1998

72. Taflove, A. and Brodwin, M. E. "Numerical solution of stead state electromegnetic scattering problems using the time dependent Maxwell's equations," *IEEE Trans. Microwave Theory Tech.* vol. 23, no. 8, pp. 623-630, Aug. 1975.

73. Taflove, A. "Review of the formulation and application of the finite difference time domain method for numerical modeling of electromagnetic wave interactions with arbitrary structures," *Wave Motion,* 10, 6, pp. 547-582, 1988.

74. Teixeira, F. L. and Chew, W. C. "A general approach to extend Berenger's absorbing boundary condition to anisotropic and dispersive media," *IEEE Trans. Antennas Propagat.*, vol. 46, no. 9, pp. 1386-1387, Sept. 1998.

75. Thomas, V. A., Jones, M. E., Piket-May, M., Taflove, M. A. and Harrigan, E. "The use of SPICE lumped circuits as sub-grid models for FDTD analysis," *IEEE Microwave and Guided Wave Lett.* Vol. 4, no. 5, pp. 141-143, May 1994.

76. Thomas, V. A., Ling, K. M., Jones, M. E., Toland, B., Lin, J. and Itoh, T. "FDTD analysis of an active antenna," *IEEE Microwave and Guided Wave Lett.* Vol. 4, no. 9, pp. 296-298, Sept. 1994.

77. Toland, B., Houshmond, B. and Itoh, T. "Modeling of nonlinear active regions with the FDTD method," *IEEE Microwave and Guided Wave Lett.* Vol. 3, no. 9, pp. 333-335, Sept. 1993.

78. Trefethen, L. N. and Halpern, L. "Well-Posedness of one-way wave equations and absorbing boundary conditions," *Mathematics of Computation*, vol. 47, pp421-435, 1986.

79. Tsai, H.S., Lin, J., Frye, R. C., Tai, K. L., Lau, M. Y., Kossives, D., Hrycenko, F. and Chen, Y. K. "Investigating of current crowding effect on spiral inductors," *1997 IEEE MTT-Symp. on Technologies for Wireless Applications*, pp. 139—142, Feb. 1997.

80. Veihl, J. C. and Mittra, R. "An efficient implementation of Berenger's Perfectly Matched Layer (PML) for finite-difference time-domain mesh truncation," *IEEE Microwave and Guided Wave Lett.*, vol. 6, no. 2, pp. 94-96, Feb. 1996.

81. Verdu, J. B., Gillard, R., Moustadir, K. and Citerne, J. "An extension of the PML technique to the FDTD analysis of multilayer planer circuits and antennas," *Microwave and Optical Technology Letters*, vol. 10, no. 6, Dec. 1995.

82. Wadell, B. C. *Transmission Line Design Handbook,* Boston: Artech House, 1991

83. Xu, J., Zhao, A. P. and Raisanen, A. V. "A stable algorithm for modeling lumped circuit source across multiple FDTD cells," *IEEE Microwave and Guided Wave Lett.* vol. 7, no. 9, pp. 308-311, Sept. 1997.

84. Yee, K. S. "Numerical solution of initial boundary value problems involving Maxwell' equations in isotropic media," *IEEE Trans. Antennas Propagat.*, vol. AP-20, pp. 302-307, May 1966.

85. Zhao, L. and Cangellaris, A. C. "A general approach for the development of unsplit-field time-domain implementations of perfectly matched layers for FDTD grid truncation," *IEEE Microwave and Guided Wave Lett.*, vol. 6, no. 5 pp. 209-211, May 1996.

86. Ziolkowski, R. W. "The incorporation of microscopic material models into the FDTD approach for ultra optical pulse simulations," *IEEE Trans. Antennas Propagat.*, vol. 45, no. 3, pp. 375-391, Mar. 1997.